FAST SPATIALLY-RESOLVED ELECTRICAL MODELLING AND QUANTITATIVE CHARACTERISATION OF PHOTOVOLTAIC DEVICES

Xiaofeng Wu（吴笑风）

April 2015

Thesis submitted in partial fulfilment of the requirements for the award of

Doctor of Philosophy of Loughborough University

Centre for Renewable Energy Systems Technology (CREST)

School of Electronic, Electrical and Systems Engineering

Loughborough University

Loughborough, Leicestershire, LE11 3TU, UK

Abstract

An efficient and flexible modelling and simulation toolset for solving spatially-resolved models of photovoltaic (PV) devices is developed, and its application towards a quantitative description of localised electrical behaviour is given. A method for the extraction of local electrical device parameters is developed as a complementary approach to the conventional characterisation techniques based on lumped models to meet the emerging demands of quantitative spatially-resolved characterisation in the PV community. It allows better understanding of the effects of inhomogeneities on performance of PV devices.

The simulation tool is named PV-Oriented Nodal Analysis (PVONA). This is achieved by integrating a specifically designed sparse data structure and a graphics processing unit (GPU)-based parallel conjugate gradient algorithm into a PV-oriented numerical solver. It allows more efficient high-resolution spatially-resolved modelling and simulations of PV devices than conventional approaches based on SPICE (Simulation Program with Integrated Circuit Emphasis) tools in terms of computation time and memory usage. In tests, mega-sub-cell level test cases failed in the latest LTSpice version (v4.22) and a PSpice version (v16.6) on desktop PCs with mainstream hardware due to a memory shortage. PVONA efficiently managed to solve the models. Moreover, it required up to only 5% of the time comparing the two SPICE counterparts. This allows the investigation of inhomogeneities and fault mechanisms in PV devices with high resolution on common computing platforms.

The PVONA-based spatially-resolved modelling and simulation is used in various purposes. As an example, it is utilised to evaluate the impacts of nonuniform illumination profiles in a concentrator PV unit. A joint optical and electrical modelling framework is presented. Simulation results suggest that uncertainties introduced during the manufacturing and assembly of the optical components can significantly affect the performance of the system in terms of local voltage and current

distribution and global current-voltage characteristics. Significant series resistance and shunt resistance effects are found to be caused by non-uniformity irradiance profiles and design parameters of PV cells. The potential of utilising PVONA as a quality assessment tool for system design is discussed.

To achieve quantitative characterisation, the PVONA toolset is then used for developing a 2-D iterative method for the extraction of local electrical parameters of spatially-resolved models of thin-film devices. The method employs PVONA to implement 2-D fitting to reproduce the lateral variations in electroluminescence (EL) images, and to match the dark current-voltage characteristic simultaneously to compensate the calibration factor in EL characterisations. It managed to separate the lateral resistance from the overall series resistance effects. The method is verified by simulations. Experimental results show that pixellation of EL images can be achieved. Effects of local shunts are accurately reproduced by a fitting algorithm.

The outcomes of this thesis provide valuable tools that can be used as a complementary means of performance evaluation of PV devices. After proper optimisation, these tools can be used to assist various analysis tasks during the whole lifecycle of PV products.

Acknowledgements

I acknowledge Research Councils UK for the financial support through a joint UK-India research project entitled “Stability and Performance of Photovoltaics (STAPP)”.

Very special thanks go to my supervisors, Professor Ralph Gottschalg and Dr. Thomas R. Betts, as well as Dr. Martin Bliss, as the personal mentor, for their invaluable support, advice and patience throughout the course of this PhD.

All at CREST, past and present, deserve thanks for their contributions making it a fantastic place to work in, and will never be forgotten.

I would like to thank the STAPP family, for the outstanding management, great collaborations and fruitful discussions throughout the whole project.

I would also like to thank Jean and John Burnard. This nice couple always surprises me by demonstrating how simple scientific tricks can solve problems in their daily lives, which keeps alerting me not to be an armchair strategist.

I would also wish to express my sincere appreciation to all my family members and my girlfriend Dan Hou, for their continuous emotional support from the other side of the earth, making this 4-year time meaningful.

The list of deserved thanks in my mind is numerous, though the reasons are simple - I kept receiving “positive energy” for my study and my life. I hope everyone can feel my deep gratitude.

Finally, this moment reminds me of the wishes from my grandparents. May their souls rest in peace.

Contents

Chapter 1

Introduction

Photovoltaic (PV) technology has experienced remarkable growth over the past decade and is on its way to becoming a mature source of electricity. The world's cumulative PV capacity has grown to over 100 GW by the end of 2012 [1]. With at least 38.4 GW of newly-installed capacity in 2013, the cumulative installed capacity has reached 150 GW in early 2014, and is still booming [2, 3]. The PV systems installed globally by the end of 2013 are generating 160 TWh of clean electricity and thus avoiding about 140 million tonnes of CO_2 emission per year [3]. It is expected that the global PV market will continuously expand in the future.

The PV industry has been established for over 25 years. It consists of a long value chain from raw materials to system installation and maintenance. Currently, wafer-based silicon PV products, including monocrystalline and polycrystalline, dominate the market with over 90% share as the main technology, with the average module efficiency increased from about 12% to 16% in the last 10 years [4]. The market share of thin-film (TF) technologies, mainly refer to amorphous silicon (a-Si), cadmium telluride (CdTe) and copper indium gallium selenide (CIGS), has experienced fluctuations in recent years and reached slightly lower than 10% in 2013 [4]. Nevertheless, the module efficiencies have been increased to 10.9%, 16.1% and 15.7%, respectively [4, 5]. The other emerging technologies are also experiencing progress in recent years, however the higher cost makes them not able to challenge the predominance of c-Si and TF in the short term.

PV devices are designed to have a long lifecycle lasting 20-25 years. The performance assessments take place from the production line to the field operations. A good characterisation method can provide an effective means of evaluating the performance of the PV devices by linking the output characteristics with simple electrical parameters and performance indicators, producing an insight into the basic physics of their operations and better understanding of the effects of parameter variations and defects causing the loss of efficiency or power yield.

A PV cell is commonly considered as a diode-like device. Conventionally, at the finished-product stage, the electrical behavior of a PV device is described by a lumped equivalent diode circuit model and its current-voltage (*I*-*V*) curve, which has been standardised [6]. The performance of the device can be evaluated by the shape

of an *I-V* curve by a set of indicators. Defects in a device can change the shape of an *I-V* curve and thus these indicators. By using a solar simulator, a PV device can be tested in very short time (e.g. less than one second) and the *I-V* curve can be effectively fitted by a lumped diode model.

However, PV cells are devices with large active areas. Internal (e.g. defects) and external (e.g. non-uniform illumination) inhomogeneities can be potential sources that reduce the power output and efficiency [7]. Without the consideration of spatial variations, the lumped model imperfectly models device behavior, especially in the case of devices with very high currents (e.g. concentrator devices) or TF devices with high lateral resistances. As a consequence, advanced optoelectronic characterisation techniques, mainly scanning- and imaging- based, were then developed for detailed spatially-resolved investigation of the devices.

Scanning techniques, e.g. laser beam induced current (LBIC) [8], rely on point-by-point measurements to scan across the surface of a sample. Quantitative electronic signals can be measured to reveal the defects or other imperfections. The main drawback is the long time required to cover an entire or even a segment of a sample with a realistic spatial resolution, which makes it unsuitable for in-line characterisation. Imaging techniques such as electroluminescence (EL) [9], photoluminescence (PL) [10], and lock-in thermography (LIT) [11] overcome this drawback by using imaging sensors. Large arrays of data points can be taken in relatively short periods of time e.g. only a few seconds. EL and PL techniques are already deployed in industrial environments for the inspection of the final products or the wafers. Due to the emergence of low cost image sensors, the roles of imaging characterisation in the PV industry are expected to become more important.

To date, industrial imaging characterisation methods are often qualitative but have not yet utilised the potential of those measurements. The consideration of the spatial nature of the devices requires spatially-resolved models (SRMs) for the development of advanced quantitative analysis of the measurements. The SRM of a PV cell e.g. in [7] is a nonlinear circuit network to be solved by circuit simulation tools e.g. SPICE (Simulation Program with Integrated Circuit Emphasis) derivatives such as PSpice (commercial) [12-15] and LTSpice (free) [16, 17]. However, the complicated

preparation, significant memory consumption and long execution time rule them out for high-resolution simulations in industrial environments.

A number of existing EL- and PL-based quantitative characterisation techniques rely on over-simplified SRMs, i.e. using a lumped resistance value to represent the localised series resistance effects from both the internal (vertical) and the external (lateral) series resistances, as investigated in [18]. By combining other simplifications e.g. ignoring shunt resistances, approximate analytical relationships between the measurements and the model parameters can be established, producing full-resolution maps of derived parameters, e.g. series resistance maps [19, 20]. However, the validity of using these simplified models and various assumptions have not been fully proven.

The aim of this project is to achieve quantitative analysis of the localised electrical properties in PV devices with high resolution (e.g. equivalent to a mega-pixel EL image) and within acceptable computing time (e.g. a few minutes). This can be achieved by means of two objectives, i.e. to develop an efficient numerical algorithm to solve SRMs and a parameter determination method that can produce localised parameters for the SRM without being over-simplified. The outcomes of the project are supposed to help improving modelling and characterisation of PV devices by utilising an efficient spatially-resolved framework as a complement to conventional lumped or over-simplified approaches. The tools developed may be further adjusted for real-world PV device characterisation for various purposes from in-line quality control to in-field performance assessments.

Considering the issues addressed above, a fast simulation toolset for the SRM is developed in this project and applied to quantifying EL measurement results for extracting localised electrical parameters. More specifically, Chapter 2 will provide a review of PV devices, as well as modelling and characterisation techniques. The fundamentals of PV devices, especially from the electronics point of view, will be given as the background. Commonly used lumped diode models and important performance indicators of the electrical behaviour will be introduced thereafter, followed by a review of spatially-resolved modelling and existing quantitative imaging-based characterisation techniques.

Chapter 3 will focus on the development of the PV-Oriented Nodal Analysis (PVONA) tools for effectively solving the SRMs. The core of the PVONA toolset is a specifically designed and optimised numerical solver that utilises sparse matrix techniques and GPU-based parallelised conjugate gradient algorithm for acceleration. It is verified and evaluated in this chapter, showing its advantages against LTSpice (v2.44) [21] and PSpice (v16.6) [22], as two popular SPICE derivatives used for reference, in terms of computation time and memory usage.

Chapter 4 will demonstrate the applicability of the PVONA-based SRM for describing spatial variations or inhomogeneities in PV devices. Two case studies are presented in this chapter to illustrate how the PVONA-based SRM can be implemented as a valuable complementary tool for analysing the performance of PV devices or developing new characterisation techniques. The chapter will also illustrate how the PVONA is integrated into a hierarchical architecture for modelling PV modules and more complex electrical topologies in real PV systems.

Chapter 5 will cover the development of a quantitative characterisation method that combines EL and fast 2-D fitting with PVONA-based SRMs. This method is especially useful in TF devices for separating the lateral resistance effects (e.g. of the transparent conductive oxide layer) from the overall series resistance. The proposed approach is verified by PVONA-based simulations and verified by experiment results of an a-Si module. The application of the method towards quantitative analysis of the local shunts is elaborated as a case study, showing its potential feasibility in industrial environments.

Finally, the conclusions drawn from this project will be found in chapter 6. This chapter will also provide recommendations for the further development and optimisation of the PVONA tools and quantitative characterisation techniques.

Chapter 2

PV devices,
electrical modelling and
characterisation techniques

2.1 Overview

This chapter provides fundamental concepts for linking electrical properties to the performance of PV cells as used in this thesis. In general, modelling and characterisation can be considered as a pair of reciprocal operations. Modelling takes local electrical parameters as inputs to calculate the operating points under specified operating conditions, while characterisation seeks determination of local electrical parameters from experimentally obtained operating points. Therefore, it is important to establish the analytical relationship between the measuring techniques and the specific electrical properties involved.

The chapter firstly provides a selective review of the fundamentals, including the generation, separation and recombination of electron-hole pairs, of semiconductor PV materials. These help establish a macroscopic means to describe the behaviour of PV devices via circuit equivalent models. The different types of equivalent models are discussed with respect to the features of different materials. The conventional current-voltage characterisation based on the lumped modelling is then introduced, with the investigation of how the global behaviour of PV devices can be influenced by parametric and environmental factors, as well as the mismatch effects.

However, PV cells and modules are large area devices that are sensitive to spatial inhomogeneities such as defects or nonuniform environmental conditions. This requires spatially-resolved modelling and characterisation techniques to describe localised electrical properties in the devices. The evolution of distributed modelling and spatially-resolved characterisation techniques of PV devices will be reviewed and compared. A brief run back over the attempts towards quantitative analyses in recent years will be given, indicating the necessity for developing an efficient spatially-resolved simulation tool and a parameter extraction algorithm.

2.2 Fundamental of PV devices

2.2.1 Charge carrier generation

“Photons in, electrons out” describes the photovoltaic effect [23] – the principle of the operation of PV cells. A PV cell is an electrical device that converts the energy of

light directly into electricity by the photovoltaic effect, first reported by Edmund Bequerel in 1839. At present, the majority of commercialised PV devices in the global market are manufactured from silicon-based materials since the relevant technologies are mature and reliable [1].

Semiconductor materials act as insulators at low temperatures, but as conductors when extra energy, e.g. light, is available. Light, made up of photons, falls onto semiconductor material with a certain amount of energy. The photons with energy (E_{photon}) less than the bandgap energy (E_g) have only weak interactions with the semiconductor material and pass through it as if it were transparent [24]. Photons with $E_{photon} \geq E_g$, on the other hand, have sufficient energy to excite electrons up to higher energy levels, breaking covalent bonds, and creating electron-hole (e^--h^+) pairs that are then free to move. This process is illustrated in Figure 2.1 by both the bond model and the band model.

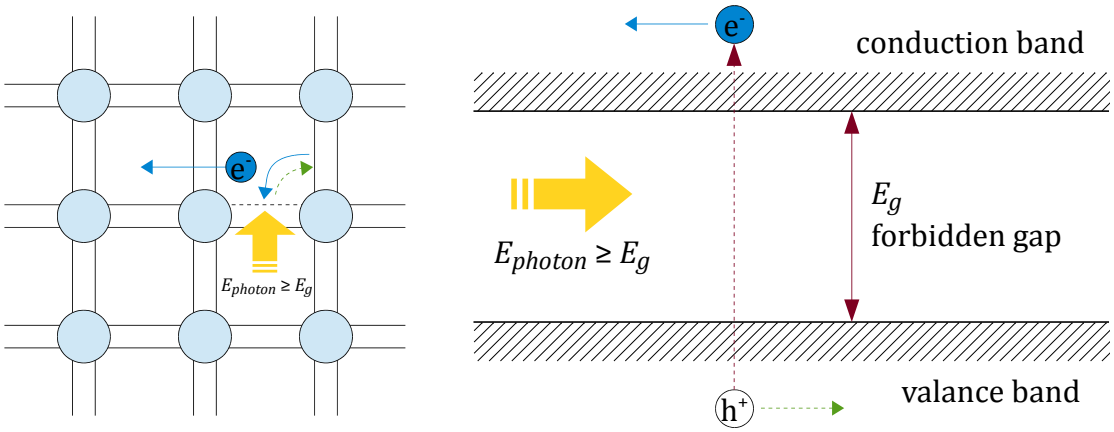

(a) (b)

Figure 2.1. 2-D schematics of conduction in semiconductors in (a) the bond model and (b) the band model. An electron-hole pair can be generated if there is sufficient energy input, i.e. $E_{photon} \geq E_g$. The released electrons and holes then become free charge carriers for the semiconductor to conduct current.

After an e^--h^+ pair is generated, the energy in excess of E_g is quickly dissipated as heat, as shown in Figure 2.2. A photon can generate only one e^--h^+ pair. Consequently, it is the incident photon flux, i.e. the number of photons striking the surface in a given period of time, rather than the photon energy density, that determines the charge carrier density and thus photocurrent generation [23, 24]. Photons with

higher energy (e.g. blue light) are absorbed closer to the surface of the semiconductor than those with lower energy (e.g. red light), i.e. lower energy photons have relatively higher penetration depths [25].

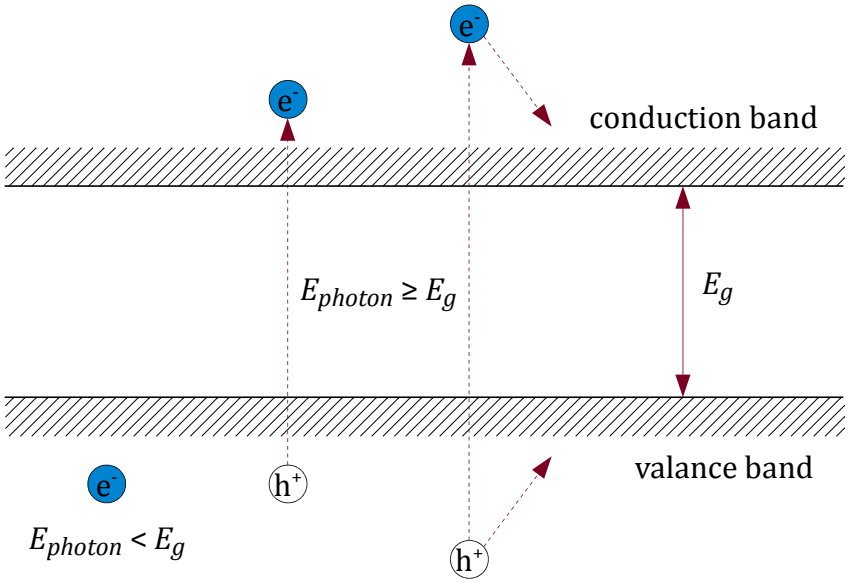

Figure 2.2. 2-D schematic of the interaction with photons with different energy in semiconductors. Photons with $E_{photon} < E_g$ cannot generate e^--h^+ pairs; photons with $E_{photon} \geq E_g$ can excite released electrons to the conduction band but the energy in excess of E_g is lost as heat.

2.2.2 Recombination

Recombination is the reverse process of free charge carrier generation. It is an electronic relaxation event that results in losing mobile charge carriers in pairs, accompanied by releasing energy. For example, in the photovoltaic effect, when the light source is removed, the semiconductor system must return to an equilibrium state from the excited state, during which the electrons and holes generated by the light move around until they meet up and recombine in pairs, and then eventually stabilise.

The energy losses in recombination can be in the form of the photons, phonons or the kinetic energy of another carrier, corresponding to radiative, Shockley-Read-Hall (SRH) and Auger [26] recombination mechanisms, respectively, as demonstrated in Figure 2.3.

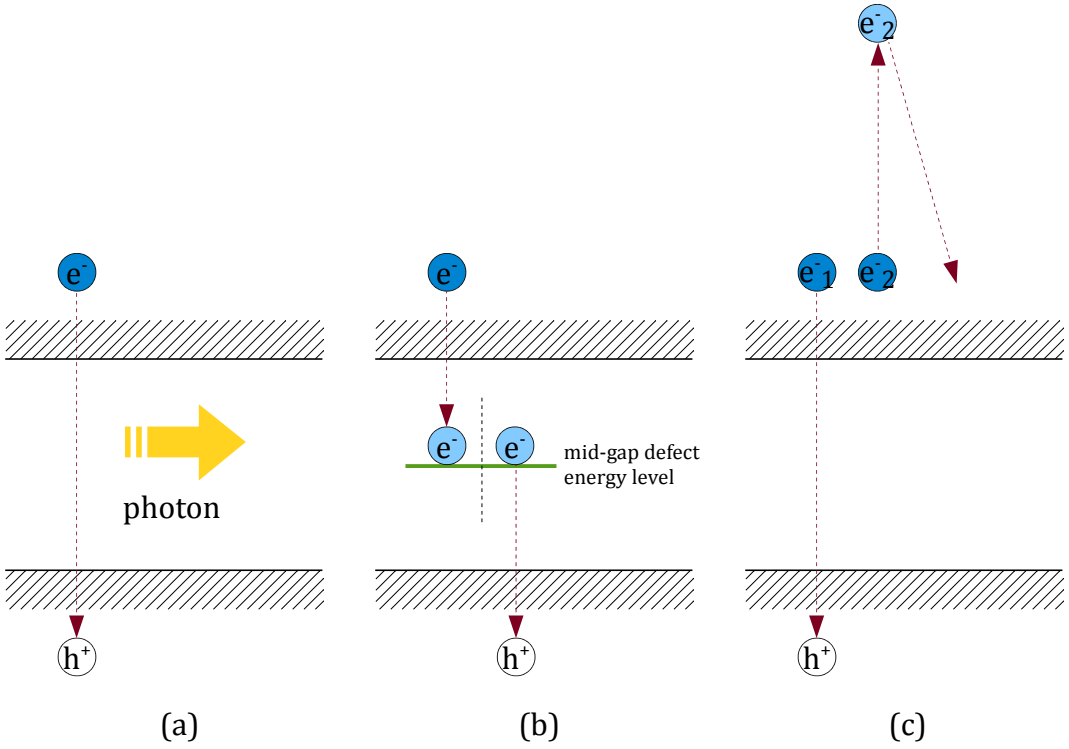

Figure 2.3. Schematics of (a) band-to-band, (b) SRH and (c) Auger recombination mechanisms. Recombination losses are import resources that can reduce the efficiency of PV cells. Auger and SRH recombination dominate in silicon-based PV cells. Radiative recombination makes luminescence-based characterisation techniques effective.

Radiative band-to-band recombination is the reverse of photon absorption. An electron from the conduction band directly combines with a hole in the valence band. This is accompanied by releasing a photon, as illustrated in Figure 2.2. The energy of the emitted photon is similar to that of the bandgap. This results in only weak re-absorption, enabling the photon to exit the semiconductor. For example at a temperature of 300 K, the bandgap of silicon (Si) is 1.11 eV, which equivalents to a wavelength of 1117 nm, in the near infrared (NIR) range. For gallium arsenide (GaAs) the value is 1.43 eV, or 867 nm, which is in the NIR range as well. In direct bandgap semiconductor materials (e.g. GaAs), radiative recombination is the dominant mechanism of recombination. In most terrestrial applications, where Si-based indirect bandgap semiconductor dominates, radiative recombination is relatively low [25]. However, it is the most significant recombination mechanism that makes luminescence-based characterisation techniques effective, which will be introduced in Section 2.5.

SRH recombination mainly denotes recombination via localised trap states caused by defects. Two steps are involved in SRH recombination. Firstly, a free electron is trapped to a trap state in the forbidden gap which is introduced by defects or impurities in the semiconductor, releasing energy as either a photon or multiple phonons. Secondly, the electron relaxes to the valence band, if it is not thermally re-emitted into the conduction band, and recombines, releasing energy as a further photon or phonons. Theoretically, SRH recombination does not occur in pure intrinsic materials.

An Auger recombination process involves three charge carriers. A first electron recombines with a hole. However, rather than emitting a photon or phonons, the excess energy is given to a second electron which is to be excited to a higher energy level in the conduction band and then thermalises back down to the edge of the conduction band, releasing its energy to phonons. Auger recombination is particularly effective in relatively highly-doped materials in which it becomes the dominant recombination mechanism.

Recombination losses reduce the conversion efficiency of PV cells. One of the major tasks of cell designers is to overcome these losses to improve the performance of the product. The effect of each recombination mechanism can be described by the carrier lifetime ($\tau_{\text{radiative}}$, τ_{SHR} and τ_{Auger}), i.e. the average time it takes for a charge carrier to recombine after generation due to the specific loss mechanism[24]. The lifetime of carriers in the material bulk (τ_{bulk}) can be formulated by

$$\frac{1}{\tau_{\text{bulk}}} = \frac{1}{\tau_{\text{radiative}}} + \frac{1}{\tau_{\text{SHR}}} + \frac{1}{\tau_{\text{Auger}}} \tag{2.1}$$

Recombination at the surfaces (τ_{surface}) also plays an important role. The combination of effects of bulk and surface recombination forms the effective lifetime τ_{eff} [Equation (2.2)], as an indicator of the overall recombination effects in a device.

$$\frac{1}{\tau_{\text{eff}}} = \frac{1}{\tau_{\text{bulk}}} + \frac{1}{\tau_{\text{surface}}} \tag{2.2}$$

Diffusion length (L) is another parameter to describe recombination effects. It is defined as the average distance a carrier can move from where the generation occurs until it recombines. It is related to the lifetime by

$$L = \sqrt{D\tau} \tag{2.3}$$

where D is the diffusivity (in m^2/s) [23]. Higher diffusion length is indicative of longer lifetime.

2.2.3 *p*-*n* junctions

In a piece of PV material, energy conversion starts from charge carrier generation, and then should be followed by separation and transport to establish a steady electrical potential and current in a closed circuit system. A junction acts as a selective barrier to the carrier flow, through which an asymmetric resistance and thus a driven force are established, enabling the control of the carriers in photovoltaic action.

p-*n* junction is a classic type of junctions used in PV cells. Such a junction is formed by joining *p*-type and *n*-type semiconductor materials. Both *p*-type and *n*-type materials are produced by doping, i.e. intentionally introducing impurities into an intrinsic semiconductor for the purpose of modulating its electrical properties by controlling the concentration of free charge carriers. The details of producing doped materials can be found in [27]. Briefly, the balance of electrons and holes in a doped semiconductor is shifted. The more abundant charge carriers are called majority carriers while the less abundant charge carriers are called minority carriers. In *p*-type materials, holes are majority carriers and electrons are minority carriers; in *n*-type materials, on the contrary, electrons are majority carriers and holes are minority carriers.

When two pieces of different materials are joined, due to the gradients of carrier concentrations across the junction, excess holes in the *p*-type material diffuse to the *n*-type side and meanwhile the electrons in the *n*-type material diffuse to the *p*-type side. This diffusion process results in the fixed positive and negative ion cores being exposed in the *n*-type side and *p*-type side respectively, setting up a built-in electric field ($\boldsymbol{E}$) that tends to be against it by keeping the holes in the *p*-type side and to keep the electrons in the *n*-type side. This electric field quickly sweeps free carriers out and therefore forms a depletion region (also known as space charge region) in which

there is few free charge carriers, and consequently a built-in voltage is established. The formation of a *p*-*n* junction is sketched in Figure 2.4a.

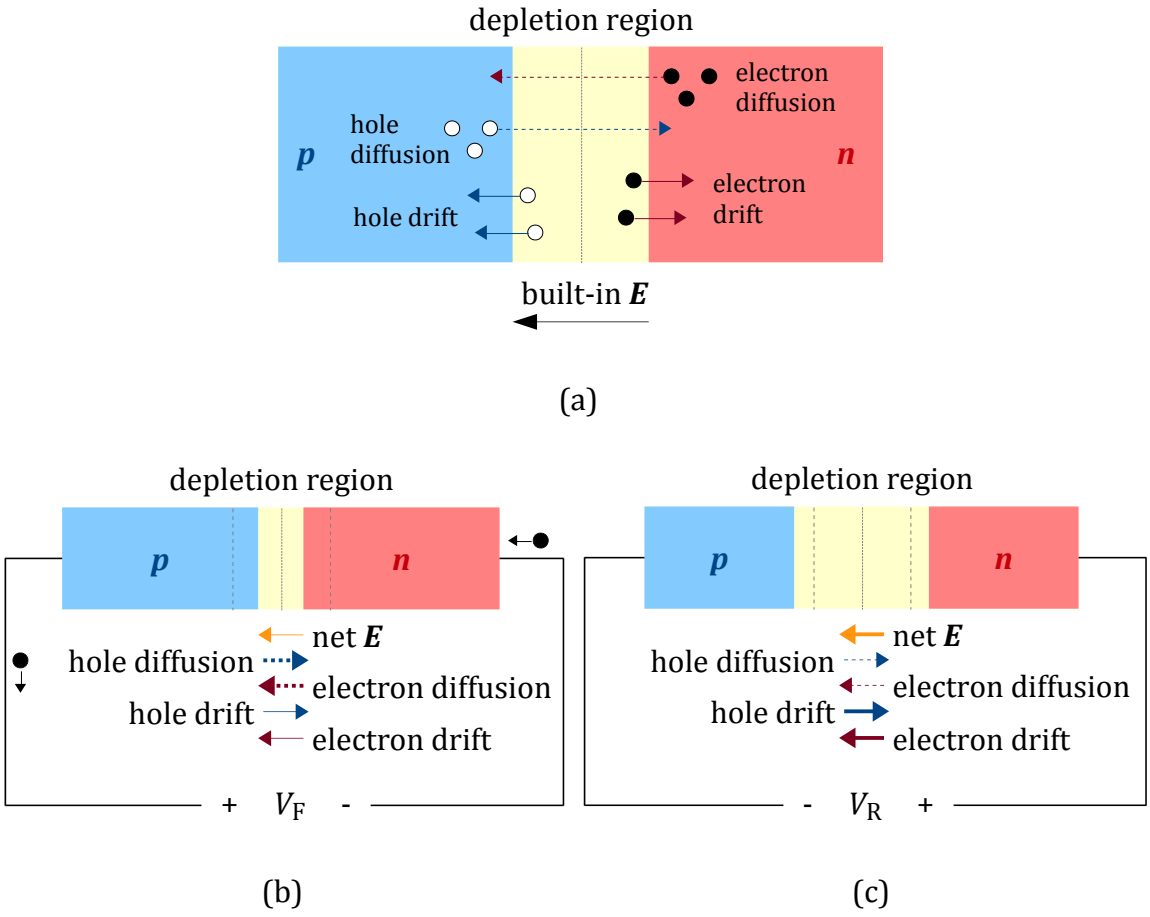

Figure 2.4. Schematics of a *p*-*n* junction that is (a) in equilibrium, (b) forward-biased and (c) reverse-biased. The electrical bias changes the intensity of the electric field across the junction and the width of the depletion region, and therefore the distribution of charge carriers. A current flow can be established in forward bias.

A *p*-*n* junction can operate under either a forward or a reverse bias. When a forward bias (V_F) is applied, as shown in Figure 2.4b, the electric field set up across the junction is decreased by the external electric field introduced by the biasing, which reduces the drifts and encourages diffusions. The increased diffusions cause minority carrier injection at the edges of the depletion region. The minority carriers will eventually recombine with majority carriers provided by the external circuit and therefore a current is established, flowing from the *p*-type side to the *n*-type side (in the opposite direction of the electron flow). When reverse-biased (V_R), as shown in Figure 2.4c, the resultant electric field across the junction is increased, resulting in

decreasing of the diffusion current. A PV device is normally forward-biased during operation. Reverse bias can be useful in some specific characterisation techniques for revealing some defects that can be identifiable only when reverse-biased, which will be studied in Section 2.5.

The electrical behaviour of *p*-*n* junction can be described by the Shockley ideal diode equation

$$I = I_{sat}\left[\exp\left(\frac{qV_j}{kT}\right) - 1\right] \tag{2.4}$$

where I is the operating current, I_{sat} is the dark saturation current, V_j is the applied voltage, q is the charge of an electron, k is Boltzmann's constant and T is the absolute temperature of *p*-*n* junction. I_{sat} is an important parameter that reflects the quality of the semiconductor material by acting as a measure of the recombination [25].

A variation of the *p*-*n* junction, the *p*-*i*-*n* junction, is also used in PV products. The main difference is that there is a layer of intrinsic semiconductor (*i*-layer) sandwiched between the *p*-type and the *n*-type materials. The electric field built between the *p*-type and *n*-type materials extends over the entire *i*-layer. This structure can have advantages if the minority carrier diffusion lengths of the material are short [23]. However, since the conductivity of the *i*-layer is relatively lower than that of the doped layers, extra series resistances may be introduced.

2.2.4 Structure and operation of PV cells

Two types PV cells are involved in this work, namely the wafer-based crystalline silicon (c-Si) cells and the thin-film amorphous silicon (a-Si) cells. At this stage, only non-bifacial single-junction cells are considered, although the outcomes of this work can potentially be extended to more complicated cases. This will be discussed in Chapter 6.

A PV cell is a flat diode-like electrical device, built with the *p*-*n* structure for c-Si devices and the *p*-*i*-*n* structure for a-Si ones. Apart from the types of junctions, there are distinct differences on the structures of c-Si and a-Si cells, among which the front contact is the most significant one, as sketched in Figure 2.5. Metal contact grids are used in c-Si PV cells, in which busbars are directly connected to the external leads

while fingers collect local currents and delivery them to the busbars. In thin-film cells, a transparent conducting oxide (TCO) layer is used as the front contact to collect and conduct current flows. Due to the relatively high resistivity of the TCO, a-Si PV cells are more likely to suffer from high series resistance.

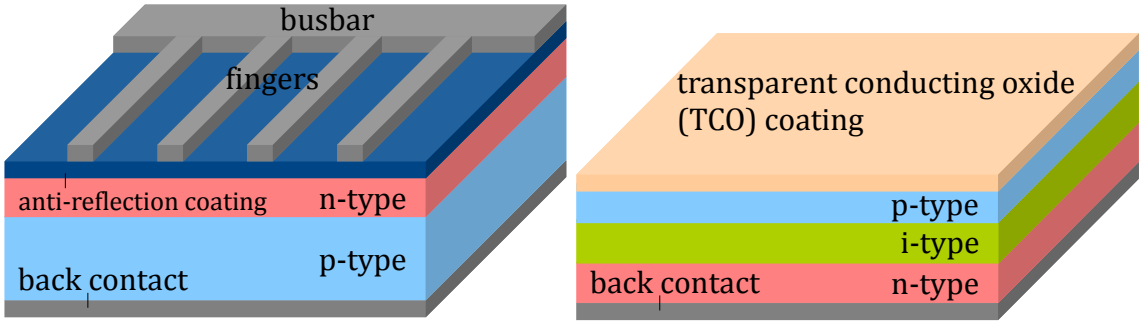

(a) (b)

Figure 2.5. Schematics of segments of (a) a *p*-type c-Si and (b) an a-Si PV cells. In a contact grid of a c-Si cell, fingers collect local currents and delivery them to the busbars which are directly connected to the external leads. In a-Si cells, a TCO layer is used as the front contact.

The power output of a PV cell is determined by a sophisticated balance between light absorption, charge carrier generation, separation, recombination, and transport, as sketched in Figure 2.6, using a *p*-*n*-junction-based c-Si cell as an example. The cell absorbs usable photons and generates e^--h^+ pairs at different sites. Ideally, e^--h^+ pairs generated near the junction area are effectively separated and swept towards the contacts, establishing a current flow that interacts with the external circuit. Some e^--h^+ pairs are lost before collection due to recombination.

The composition of incident light can influence the recombination in the cell. For example, as discussed in Section 2.2.1, since photons with higher energies (e.g. blue) have a lower penetration depth than those with lower energies (e.g. red), the blue portion of the incident light is absorbed close to the surface and thus is more likely to suffer from front surface recombination, while the red portion can go deeper in the cell and is more likely to recombine in the bulk or at the back contact. Defects in the cell can act as extra recombination centres that produce SRH recombination, as illustrated in Section 2.2.2.

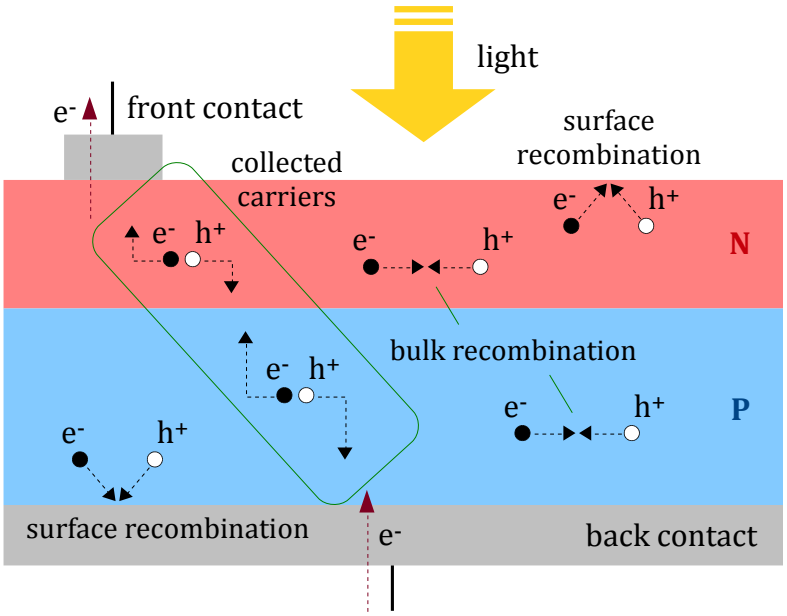

Figure 2.6. 2-D schematic of the operation of a *p*-*n*-junction-based PV cell. The cell absorbs usable photons and generates e^--h^+ pairs at different sites. Some e^--h^+ pairs are lost before collection due to recombination. The remaining carriers are separated by the electrical field across the *p*-*n* junction and establish a current flow in the circuit.

2.3 Lumped electrical modelling for PV cells

2.3.1 Single-diode model

Since a PV cell has a junction-based structure and thus a diode-like behaviour, it can be equivalent to a diode-based circuit model. One of the most commonly used type of diode models for c-Si PV cells, i.e. the single-diode model [28-33], is shown in Figure 2.7. With the marked reference direction, an equation can be formulated according to the Kirchhoff's current law (KCL)

$$I = -I_{ph} + I_{sat}\left\{\exp\left[\frac{q(V - IR_s)}{nkT}\right] - 1\right\} + \frac{V - IR_s}{R_{sh}} \tag{2.5}$$

where I is the overall current, V is the terminal voltage. I_{ph} is the photocurrent, n is the ideality factor of the diode, R_s is the series resistance and R_{sh} is the shunt resistance.

More specifically, I_{ph} is a current source that represents photocurrent. In common simplifications, the intensity of I_{ph} is considered to be proportional to the irradiance

when the cell is illuminated and is 0 if the cell is in dark. However, it shows a nonlinear behaviour in e.g. a-Si devices and needs to be described by a specific model, as introduced in Section 2.3.3. The second factor on the right hand side of Equation (2.5) is a variant of the ideal diode Equation (2.4), representing the behaviour of the *p*-*n* junction, in which the ideality factor *n* ranges from 1 to 2, where $n = 1$ suggests a pure diffusion at the junction and $n = 2$ indicates the junction is complete drift-driven [25]. R_s and R_{sh} are parasitic resistances, namely series resistance and shunt resistance respectively. The main sources of R_s include bulk resistance of the material, contact resistances, sheet resistance, etc. R_{sh} can be relevant to impurities in the material or unexpected current paths introduced during the manufacturing procedures. The existence of R_s results in a voltage drop between the terminal and the junction, i.e. $V_j = V - IR_s$. R_{sh} provides a potential current path with the loss represented by the third factor on the right hand side of Equation (2.5).

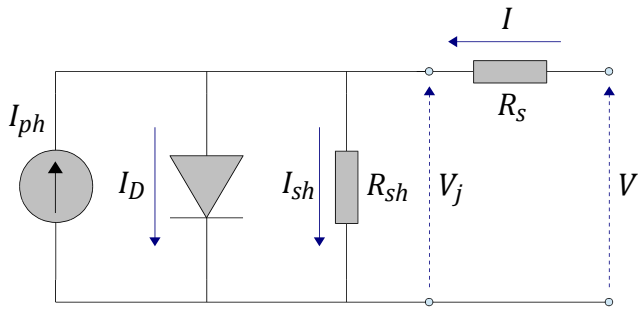

Figure 2.7. Single-diode model for PV cells. When operating under illumination, the output current of the cell is the remaining part of I_{ph}, by subtracting the losses at the *p*-*n* junction and the shunting path.

Equation (2.5) is a nonlinear equation which cannot be solved analytically. Instead, iterative algorithms are commonly used, among which Newton-Raphson (NR) is an effective one. For a given terminal voltage V_x, the operating current I_x can be obtained by iteratively solving Equation (2.5) by NR method

$$I_{k+1} = I_k - \frac{f(I_k)}{f'(I_k)}|_{V_x} \tag{2.6}$$

$$f(I) = I + I_{ph} - I_{sat}\left\{\exp\left[\frac{q(V - IR_s)}{nkT}\right] - 1\right\} - \frac{V - IR_s}{R_{sh}} \tag{2.7}$$

$$f'(I) = 1 + \frac{qI_{sat}R_s}{nkT}\exp\left[\frac{q(V - IR_s)}{nkT}\right] + \frac{R_s}{R_{sh}} \tag{2.8}$$

where I_{k+1} and I_k are the estimations of the current from the active NR loop and the previous loop respectively.

2.3.2 Double-diode model

The single-diode model given by Equation (2.5) assumes a constant value for the ideality factor n and neglects the recombination in the depletion region. In fact, n is a function of the voltage across the cell which is determined by the balance between diffusion, drift and recombination effects [25]. To compensate the omitted factors in the single-diode model, a second diode is added in parallel with the first one [34-38], as shown in Figure 2.8. The equation of the model then becomes

$$\begin{aligned} I = -I_{ph} + I_{sat1}\left\{\exp\left[\frac{q(V - IR_s)}{n_1 kT}\right] - 1\right\} + \\ I_{sat2}\left\{\exp\left[\frac{q(V - IR_s)}{n_2 kT}\right] - 1\right\} + \frac{V - IR_s}{R_{sh}} \end{aligned} \tag{2.9}$$

where I_{sat1} and I_{sat2} are the dark saturation currents, n_1 and n_2 are the ideality factors of the two diodes respectively.

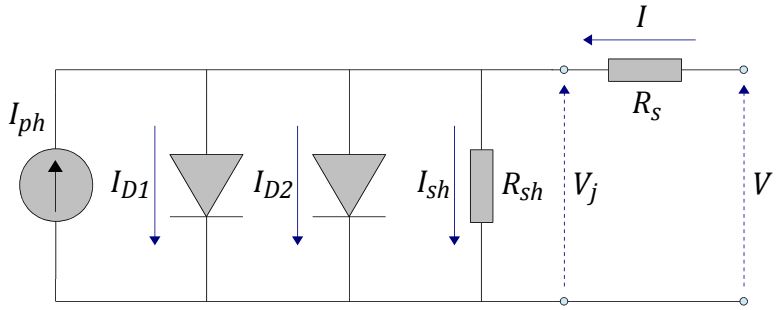

Figure 2.8. Double-diode model for PV cells. The first diode with n_1 = 1 is used to represent the diffusion in the junction. A second diode with n_2 = 2 is added in parallel with the first one to describe the recombination in the depletion region that is omitted in the single-diode model.

In the double-diode model, the first diode describes the diffusion current with the ideality factor n_1 = 1, and the second diode is used to describe the recombination in

the depletion region in the junction, with n_2 = 2 [25], although in some cases this value is reported to be greater than 2 [39-43].

Similarly, Equation (2.9) can be solved by using NR algorithm as formulated by Equation (2.6), in which there are

$$f(I) = I + I_{ph} - I_{sat1}\left\{\exp\left[\frac{q(V - IR_s)}{n_1 kT}\right] - 1\right\} - I_{sat2}\left\{\exp\left[\frac{q(V - IR_s)}{n_2 kT}\right] - 1\right\} - \frac{V - IR_s}{R_{sh}} \tag{2.10}$$

$$f'(I) = 1 + \frac{qI_{sat1}R_s}{n_1 kT} exp\left[\frac{q(V - IR_s)}{n_1 kT}\right] + \frac{qI_{sat2}R_s}{n_2 kT} exp\left[\frac{q(V - IR_s)}{n_2 kT}\right] + \frac{R_s}{R_{sh}} \tag{2.11}$$

2.3.3 Merten's diode model

A-Si PV cells are based on the *p-i-n* structure, as illustrated in Section 2.2.3, they exhibit some specific characteristics that differ from c-Si devices. Particularly, the photocurrent generation becomes voltage-dependent due to the fact that drift dominants the charge carrier separation in the *i*-layer. The electric field that stretches over the *i*-layer is influenced by the voltage applied across the device. For example, an increasing forward bias can cause a decrease in the intensity of the electric field and thus a decreasing photocurrent, as the result of the increasing recombination rate. This voltage-dependent recombination loss was modelled by Merten *et al*. [44] as

$$I_{rec}(I_{ph}, V) = \frac{I_{ph} {d_i}^2}{(\mu\tau)_{eff}[V_{bi} - (V - IR_s)]} \tag{2.12}$$

where d_i, $(\mu\tau)_{eff}$ and V_{bi} represent the thickness of the intrinsic layer, effective mobility lifetime product and built-in voltage, respectively. This is equivalent to a voltage-dependent current sink in the circuit. Therefore the equation for the modified diode model as shown in Figure 2.9 becomes

$$I = -I_{ph}\left\{1 - \frac{{d_i}^2}{(\mu\tau)_{eff}[V_{bi} - (V - IR_s)]}\right\} + I_{sat}\left\{\exp\left[\frac{q(V - IR_s)}{nkT}\right] - 1\right\} + \frac{V - IR_s}{R_{sh}} \tag{2.13}$$

This modified *I-V* characteristic has been verified by Gottschalg *et al.* [45]. To solve Equation (2.13) by the NR method, Equation (2.14) and (2.15) are used.

$$f(I) = I + I_{ph}\left\{1 - \frac{{d_i}^2}{(\mu\tau)_{eff}[V_{bi} - (V - IR_s)]}\right\} - I_{sat}\left\{\exp\left[\frac{q(V - IR_s)}{nkT}\right] - 1\right\} - \frac{V - IR_s}{R_{sh}} \tag{2.14}$$

$$f'(I) = 1 + \frac{I_{ph}{d_i}^2 R_s}{(\mu\tau)_{eff}[V_{bi} - (V - IR_s)]^2} + \frac{qI_{sat}R_s}{nkT}\exp\left[\frac{q(V - IR_s)}{nkT}\right] + \frac{R_s}{R_{sh}} \tag{2.15}$$

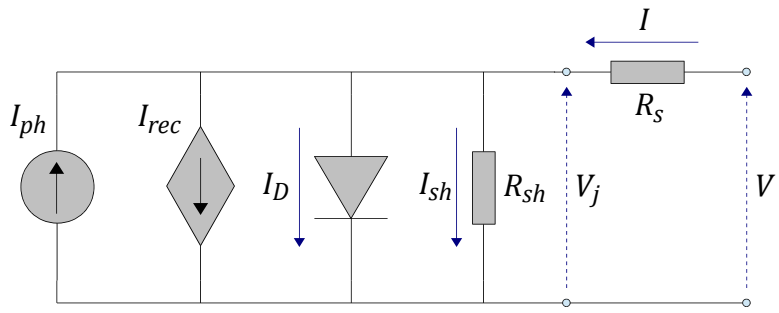

Figure 2.9. Merten's improved single-diode model for a-Si PV cells. A voltage-dependent current sink is introduced to represent the losses of photocurrent due to the recombination in the intrinsic layer.

2.4 Global current-voltage characteristics and behaviour of PV cells

2.4.1 Current-voltage characteristics and performance indicators

The measurement of the current-voltage (*I-V*) characteristic is a standard tool for the PV industry. Most commercial solar simulators are equipped with analysis tools to instantly extract critical performance indicators from measured *I-V* curves. Figure 2.10 illustrates the appearance of an *I-V* curve. In most cases, the main part of an *I-V*

curve is plotted in the first quadrant, in which the positive current and positive voltage suggests generating power. To remove the dependence of the area of solar cells, the current density (J, in A/m^2) is commonly used instead of I. J is obtained by dividing the global current I by the area of the cell. This allows the comparison between PV cells with different areas and materials.

The performance of the device under test (DUT) is commonly described by the short-circuit current (I_{SC}) [or sometimes the short-circuit current density (J_{SC}) on a J-V curve], the open circuit voltage (V_{OC}) and the maximum power point (MPP). I_{SC} is the maximum current at zero voltage and V_{OC} is the maximum voltage at zero current. The product of the current and voltage for each point on the I-V curve gives the power output for the particular operating condition. The MPP is the one with the maximum power output given by

$$P_{MPP} = I_{MPP}V_{MPP} \tag{2.16}$$

These parameters are graphically shown in Figure 2.10.

The fill factor (FF) is an important indicator of the cell quality. It is a measure of the "squareness" of the I-V curve defined by

$$FF = \frac{P_{MPP}}{I_{SC}V_{OC}} = \frac{I_{MPP}V_{MPP}}{I_{SC}V_{OC}} \tag{2.17}$$

It is the ratio of the areas of the two rectangles shown in Figure 2.10. A PV cell with a high FF tends to have a low series resistance and a high shunt resistance, and therefore less of the current produced by the cell is dissipated on parasitic resistances.

The MPP can be used to derive another important performance indicator of PV cells, namely the conversion efficiency (η), i.e. the ratio of power (or energy) output from the cell to the input power (or energy) of the irradiance

$$\eta = \frac{P_{MPP}}{P_{in}} = \frac{I_{MPP}V_{MPP}}{P_{in}} \tag{2.18}$$

where P_{in} is the power of the incident irradiance. The efficiency is one of the most commonly used parameters to compare the performance of one PV device to another.

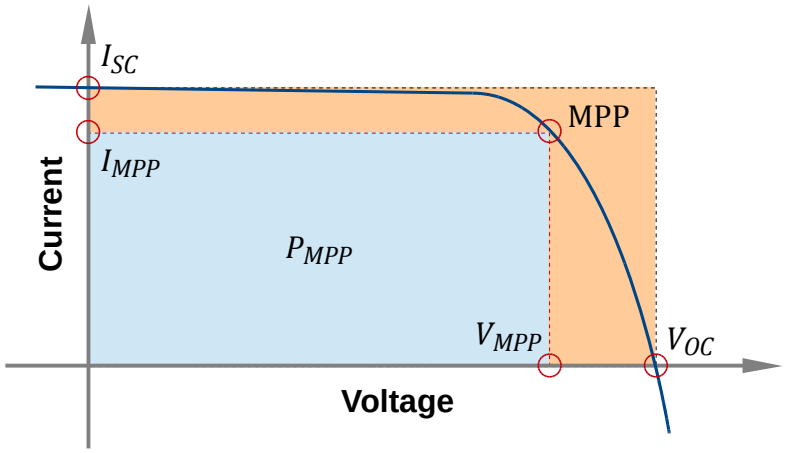

Figure 2.10. An *I-V* curve and commonly used performance indicators. I_{SC} and V_{OC} can be directly read from the curve. MPP is determined by the corresponding current (I_{MPP}) and voltage (V_{MPP}) at produces the maximum power (P_{MPP}).

Apart from the performance indicators, electrical parameters can be derived from an *I-V* curve by an iterative fitting process [38, 46, 47]. The measured *I-V* curve is used to estimate the initial values of electrical parameters for a specified model type (single-diode, double-diode or Merten's model), which are subsequently adjusted and fed to the model in each iterative sequence, to calculate a corresponding new set of operating points, i.e. an estimated *I-V* curve. The procedure repeats until there is sufficient agreement between the measurement and the estimation, as shown in Figure 2.11.

Normal *I-V* characterisations are carried out under the Standard Test Conditions (STC), i.e. 1000 W/m^2 irradiance, 25 °C temperature and AM 1.5 spectrum [6]. However, measurements under non-standard conditions are sometimes manipulated. For example, dark *I-V* measurements are used to examine the material properties of the PV devices [25, 48-51]. In dark *I-V* measurements, a PV cell is in essential a large flat diode that is intentionally biased by injected carriers rather than the light to achieve different excitation levels. Dark *I-V* measurements can be implemented without a solar simulator and can extract parameters e.g. R_s, R_{sh}, n, I_{sat}, which is sometimes more effective than illuminated measurements [25].

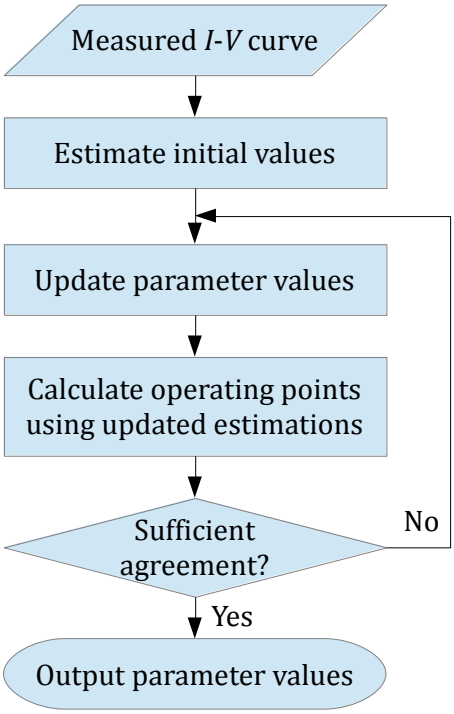

Figure 2.11. Flowchart of the iterative fitting process to extract electrical parameters from a measured *I-V* curve. In each iterative sequence, a new set of parameters is estimated and evaluated. The fitting succeeds when an estimated *I-V* curve and the measured *I-V* are in close agreement with each other.

2.4.2 Effects of parasitic resistances

Resistive effects in PV cells can reduce the efficiency of the device by dissipating power in the resistances. Series resistance (R_s) and shunt resistance (R_{sh}) are the two types of parasitic resistances in PV devices. High R_s or low R_{sh} can lead to reduction of the *FF*. Figure 2.12 and Figure 2.13 show the effects of R_s and R_{sh} on the *I-V* curves respectively.

Increasing R_s results in the *I-V* curve pivoting around V_{OC} and thus a reduction of the *FF*. An excessively high R_s can also reduce the I_{SC}. R_s does not affect the V_{OC} of the cell since there is no current flowing through it and is therefore no voltage drop, although the slope of the curve is strongly affected near the V_{OC} due to the significant voltage drop ΔV on R_s. A straight-forward method for estimating the R_s from the *I-V* curve is to find the slope at the V_{OC}.

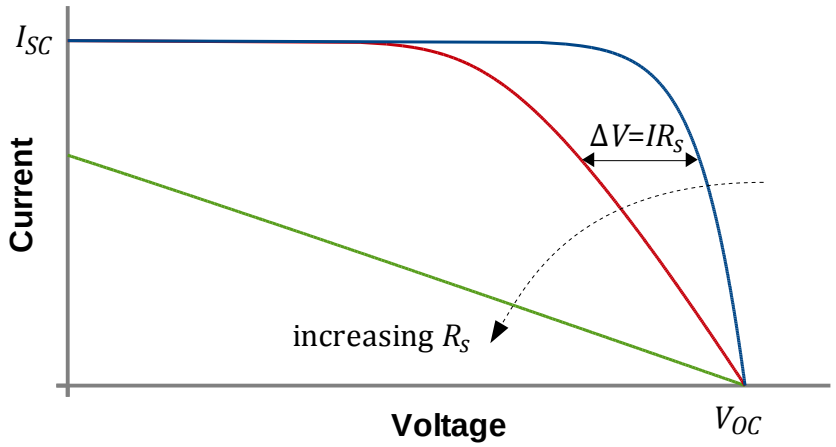

Figure 2.12. The effect of R_s on the *I-V* characteristic of a PV cell. The increasing R_s results in a shrink of the *I-V* curve and thus the decreasing *FF*. An excessively high R_s can further reduce the I_{SC}. The V_{OC} is not changed, but the slope is altered significantly and can therefore be used to estimate the R_s.

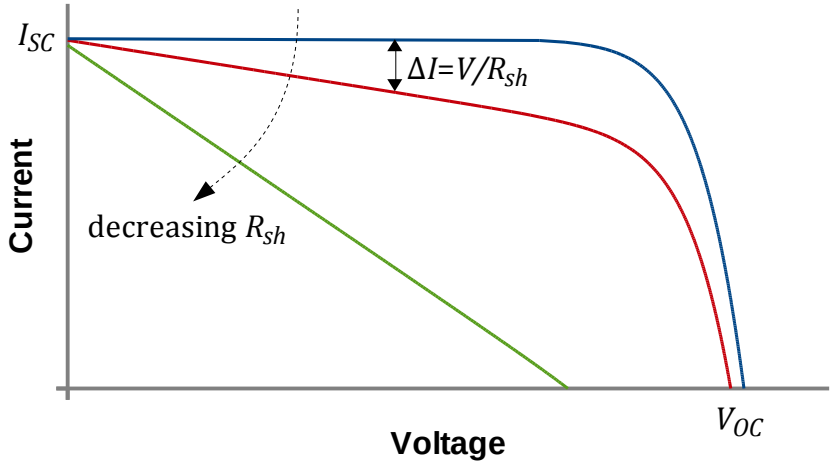

Figure 2.13. The effect of R_{sh} on the *I-V* characteristic of a PV cell. The decreasing R_{sh} results in a reduction of MPP of the *I-V* curve and thus the decreasing *FF*. The decreasing R_{sh} can reduce the V_{OC}. The slope of the curve at the I_{SC} and can be used for estimating the value of R_{sh}.

A low R_{sh} causes power loss in a PV cell by diverting the light-generated current towards an alternate current path, reducing the amount of current flowing through the junction and thus the terminal voltage. Consequently, the *FF* of the *I-V* curve is reduced. The effect of R_{sh} is more apparent at low irradiance levels [25]. The decreasing R_{sh} can gradually reduce the V_{OC} but in most realistic cases the effect will not be too noticeable. In addition, the slope of the *I-V* curve is affected near I_{SC} and can be therefore used for estimating the value of R_{sh}.

2.4.3 Effects of environmental factors

Operating PV devices experience variable environmental conditions. Environmental conditions mainly referred to are irradiance, temperature and spectrum, among which the former two factors are more important to this work. These environmental factors can have significant impacts on the *I-V* curves. Figure 2.14 and Figure 2.15 show the effects of irradiance and temperature on the *I-V* curves respectively.

Changing the light intensity on a PV cell alters the performance indicators of the resultant *I-V* curve. An increase in the irradiance can produce a proportional increase of the photocurrent generation and thus the I_{SC}. Besides, it also elevates the V_{OC} but to a lesser extent due to the logarithmic relationship between the V_{OC} and the I_{ph}. At low irradiance levels, more specifically, the effects of R_{sh} become increasingly important because the relative amount of the current that flows through the cell decreases and thus the fraction of the total current flowing through the R_{sh} increases. This feature can be helpful in identifying shunts from characterisation measurement results e.g. electroluminescence (EL) images taken under different levels of electrical excitations in the dark (Chapter 5).

Like most semiconductor devices, PV cells are sensitive to the temperature. This is due to, according to the bond and the band models of the semiconductor materials shown in Figure 2.1, the increasing temperature can be viewed as increasing the energy of the electrons in the material, and therefore lower external energy is needed to break a bond, reducing the bandgap. As a consequence it can affect most of the material parameters.

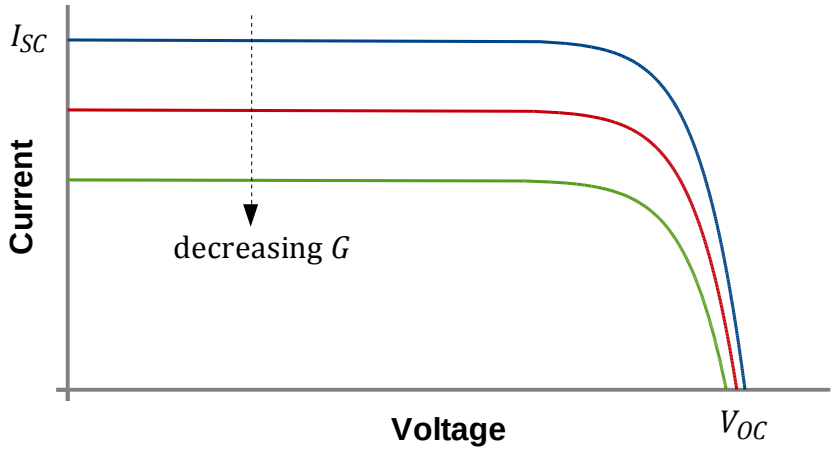

Figure 2.14. The effect of irradiance (G) on the I-V characteristic of a PV cell. Increasing irradiance causes a proportional increase of I_{ph} and thus I_{SC}. It also elevates V_{OC} but to a lesser extent due to the logarithmic relationship between the V_{OC} and the I_{ph}.

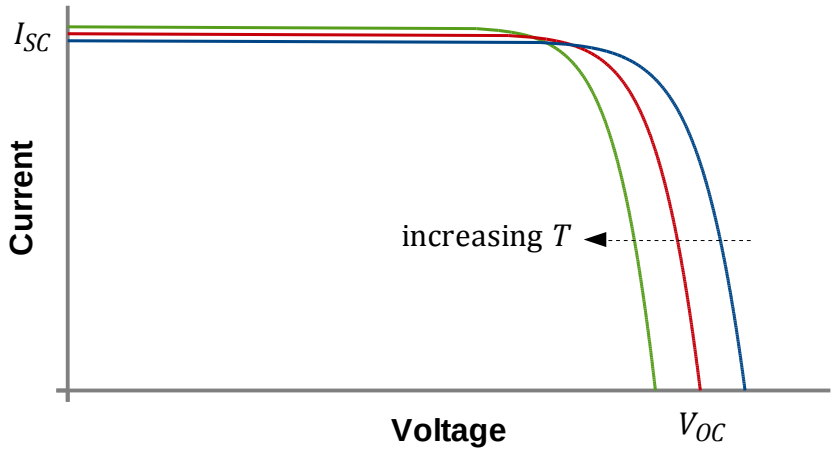

Figure 2.15. The effect of temperature (T) on the I-V characteristic of a PV cell. With increasing temperature, the main effects include the reduction of the V_{OC}, the FF and hence the overall power output, with the slight increase of I_{SC}.

In electrical modelling, a change of temperature (T) can be reflected by modifying the dark saturation current, i.e. I_{sat}, of a PV cell by

$$I_{sat} = BT^{\gamma} \exp\left(-\frac{E_{g0}}{kT}\right) \tag{2.19}$$

where B is a temperature-independent constant, E_{g0} is the linearly extrapolated bandgap at zero temperature (0 K) of the material, and γ is a correction factor that includes the effects from remaining temperature-dependent properties [24]. On an *I-V* curve, the main effects from the increasing temperature are the reduction of the V_{OC}, the *FF* and hence the overall power output, and in addition to a slight increase of I_{SC} which is not covered by the saturation current. A realistic impression is shown in Figure 2.15.

2.4.4 Effects of electrical mismatch

PV cells are always connected in series or in parallel in PV modules to provide higher current and voltage output respectively. Ideally, all the cells in a module should be identical. However, due to nonuniformity of the local electrical properties or the environmental conditions, the output from the cells in a module can be distinctively different. For example, individual cells in a module are normally connected in series, which means there is a strong effect on all other devices in a string if one cell underperforms. In this case, the overall output of the module is limited by the poorest cell. This is referred to as the mismatch effect. It is also important in distributed modelling because mismatch effects between sub-cells can provide valuable clues and evidences for analysing the local electrical properties.

The mismatch effects can be explained by Kirchhoff's current and voltage laws (KCL and KVL). If two PV elements are connected in series, as shown in Figure 2.16, the current flowing through each one should be the same, and the overall voltage equals to the sum of the voltage across each component. Although a higher voltage is established across the string of the two elements, the current is limited by the one with the worst performance, i.e. cell2. The stronger cells push the poorer cell into reverse-biased, i.e. consuming power, which results in heat generation and potentially in irreversible damage to the device [24]. Similarly, if two elements are connected in parallel, the voltages across both elements should be identical and will

be limited by the worst component, while the overall current is obtained by the sum of the current flowing through both branches.

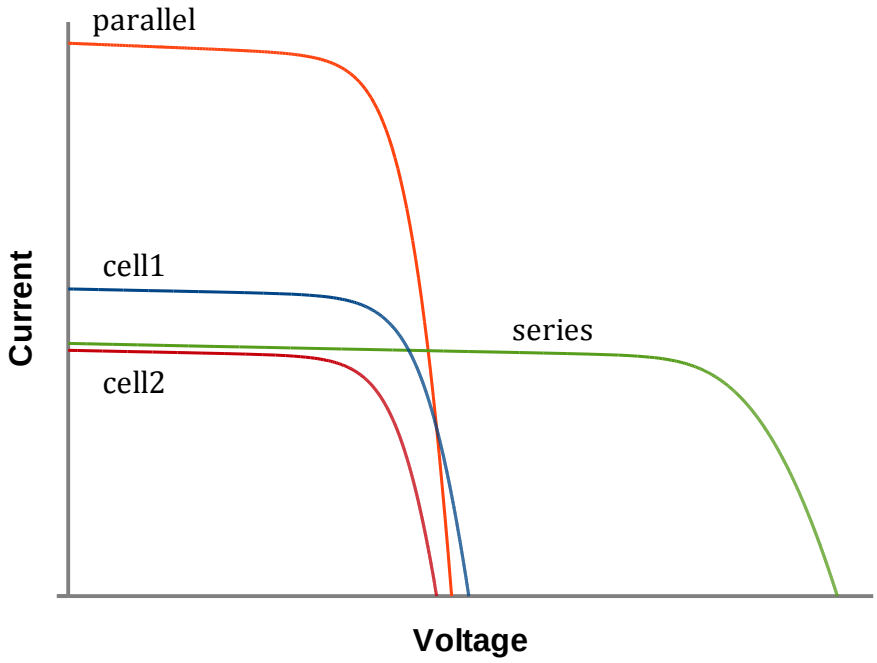

Figure 2.16. The effects of electrical mismatch on the *I-V* characteristic of two PV components connected in series and in parallel. When the two cells are connected in series, a higher voltage is established across the string, but the overall current is limited. When the connection is in parallel, the overall current is enhanced, but the voltage across the group is limited.

2.5 Spatially-resolved modelling and characterisation of PV devices

2.5.1 Spatially-resolved modelling

Global *I-V* modelling and characterisation provides a quick means of evaluation of the overall performance of PV devices, but is far from sufficient for the detailed investigation of the localised electrical properties or fault mechanisms. Different types of defects, e.g. high series resistance and low shunt resistance, can be detected by their impacts on the global *I-V* characteristics. However, it does not include information about the location and localised effects of the defects. Spatially-resolved characterisation takes localised electrical parameters into account, establishing one-

to-one links between the measurement results and local electrical parameters. To describe a device in a spatially-resolved point of view, a spatially-resolved model (SRM) is required to replace the lumped model.

In an SRM, a PV cell is represented by an array of virtual sub-cells. The size of the sub-cell array is determined by the required resolution. Each sub-cell is an analogue of a finite area of the PV material and thus can be represented by a local diode model corresponding to the material properties, as described in Section 2.3. Lateral resistances are introduced to depict the contact schemes. This is done by introducing two resistor networks to model the front contact layer (the metal grid or the TCO layer) and the back contact layer (metal), respectively. Therefore the model of a PV cell becomes a discrete nonlinear network of diode models and resistors.

There has been seen an evolution in SRMs during the past decades. The model structure is extended from the lumped model to distributed one-dimensional (1-D) [14, 52-57] and to two-dimensional (2-D) [12, 13, 16, 17, 58-69] for single-junction PV cells and further to three-dimensional (3-D) [69-71] for multi-junction cells, as shown in Figure 2.17.

To clarify, the concepts of 1-D, 2-D and 3-D structures are unified in this thesis to avoid ambiguities that have been encountered in some publications, in which the concepts of 2-D and 3-D are sometimes mixed. In this work, 1-D refers to a number-line-like structure in which the sub-cells are connected horizontally (Figure 2.17a). A 2-D model uses an array of sub-cells to represent a cell in which each sub-cell can be located by a Cartesian coordinate pair (x, y) (Figure 2.17b). In a 3-D model, the z axis is introduced to suit the multiple junctions while each is represented by a 2-D model (Figure 2.17c).

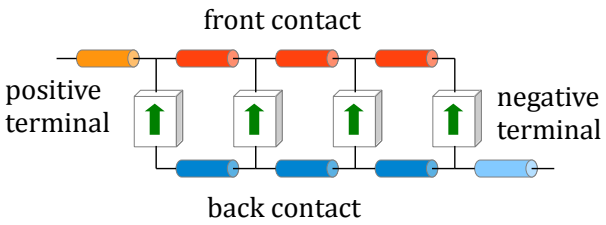

(a)

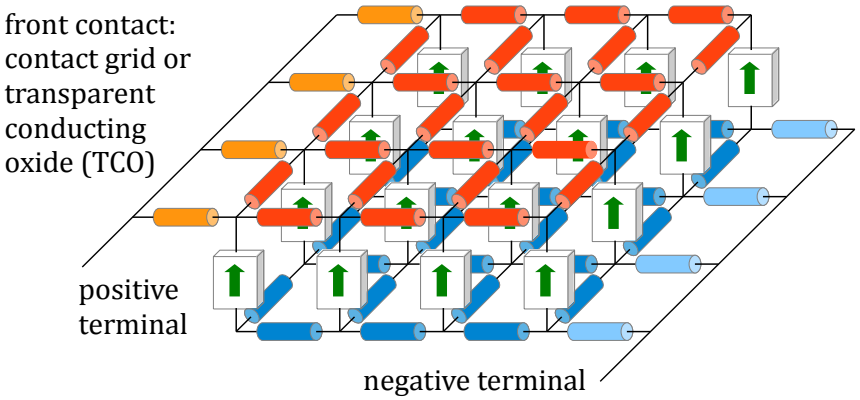

(b)

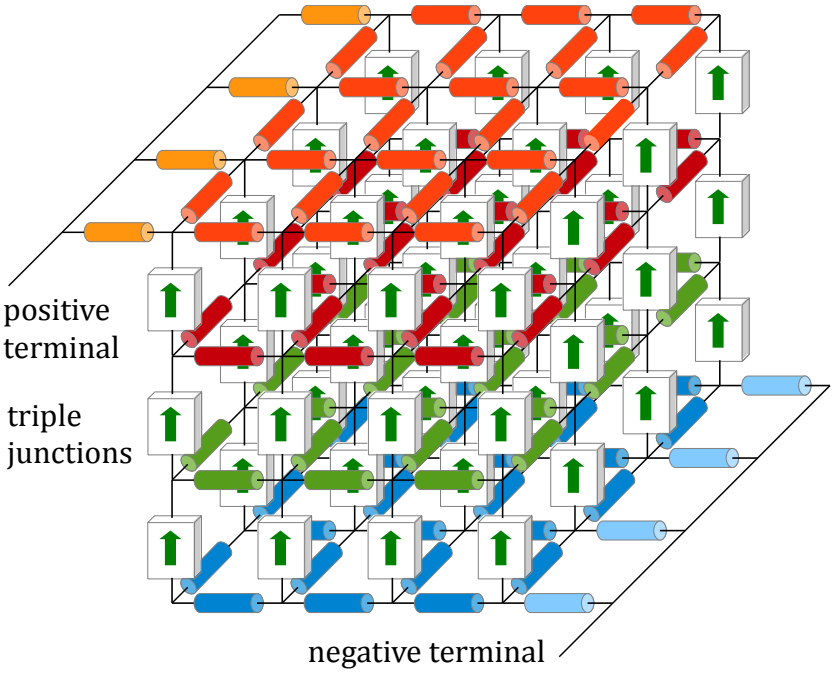

(c)

Figure 2.17. Schematics of (a) 1-D model, (b) 2-D model and (c) 3-D triple-junction model. A PV cell is divided into an array of virtual sub-cells. Each local sub-cell is an analogue of a finite area of the PV material. The cell is therefore a nonlinear circuit network.

1-D modelling was reported in some early attempts to analyse the effects of series resistances. The sub-cells are organised in a single row to represent a finite number of segments along the width of the cell. The resistors between every two parallel diode models enable the spatial variations of local operating points due to the lateral resistances observable along the width of the cell. Representatively, Boone and Van Doren in 1978 [52] used a 1-D distributed model to support PV cell design in analysing resistive losses. It was further used for assisting the design of the grid structure geometries of c-Si cells. In 1982, Nielsen [53] applied a similar 1-D model structure to study the distributed series resistance effects in solar cells. Zekry and Al-Mazroo [14] reported a model in SPICE (Simulation Program with Integrated Circuit Emphasis) with special attention paid to the non-uniform current distribution and effective series resistances, as well as the dynamic characteristics of a cell. Most of the later studies of 1-D modelling focused on the variations of electrical properties due to the effects of the width [57] or thickness of PV cells.

2-D models were developed to extend the 1-D model to the planar level, enabling real spatially-resolved modelling for single-junction PV cells with literally arbitrary spatial resolution. 2-D models are sometimes also referred to as “quasi-3-D” models because a corresponding discrete circuit network has a 3-D structure in which current can flow horizontally in the front and back contacts and vertically in the local diode models. However, since there is only one physical junction, it is reasonable to fit the array of sub-cells in a Cartesian coordinate system. Kasemann *et al*. in 2008 [59] introduced a 2-D model that allows the simulation of lateral voltage distributions for analysing non-uniform operating points detected in luminescence measurement results. Vorasayan *et al*. in 2011 [62] proposed a quasi 3-D model to investigate inhomogeneities in a-Si PV modules. Moreover, the model was used to study the electrical mismatch effects in the dark- and illuminated-LBIC (laser beam induced current) measurements, and to verify the improved limited-LBIC measurement technique. Pieters [12] published a model for thin-film PV cells with an adaptive mesh, which was validated by EL measurement results and corresponding simulations of a CIGS PV module with a local shunt. Brecl *et al.* reported detailed studies of electrical losses in thin-film modules due to monolithic contacts [72] and different configurations and front contacts [15] by using 1-D and

2-D simulations. An EL analysis method for small area circular CdTe cells using a 2-D SPICE model was reported in [73]. Several researchers published similar modelling approaches for thin-film PV devices to study the electrical behaviour of local defects in various characterisation measurements. Some other researchers attempted to apply the 2-D model structure to c-Si devices by introducing a contact grid, which can be found in the work of Eidelloth *et al*. [16], Gupta *et al*. [13] and Guo *et al*. [17, 65].

Most of these models use existing circuit simulation software packages, e.g. derivatives of SPICE, as the simulation engine. These SPICE derivatives include both commercialised and free version. For example, PSpice [22], as a typical commercial derivative, was used in [12-15, 73]; and LTSpice [21], as a free derivative, was used in [16, 17]. In addition, works utilising WinSpice [62] and HSpice [74] were also reported. As an alternative approach, Fecher *et al*. [68] used a finite element modelling (FEM) tool to model the 2-D electrical behaviour of the influence of a local shunt in a thin film PV device. But FEM-based methods have not been widely used.

With the development of multi-junction PV technology, 3-D modelling techniques have been applied to study internal electrical properties of MJ PV devices. The triple-junction SPICE model developed by Nishioka *et al*. [70] was used in the analysis of the electrical performance of concentrated PV (CPV) cells, during which the chromatic aberration and the intensity distribution were taken into account.

In this project, a 2-D model is used for describing PV devices. In the 2-D point of view, localised electrical properties in a cell are normally obtained through spatially-resolved characterisation techniques. There are mainly two types of such techniques, i.e. scanning (or mapping) and imaging. Local spectroscopic techniques are emerging in recent years [75-77] but are out of the scope of this work. Scanning techniques are able to provide absolute measurement of current or voltage but are naturally time-consuming (up to many hours for a full-area scan) and are thus not suitable for industrial applications. Imaging techniques can take the measurements within only a few seconds but require after-treatments to be quantified.

2.5.2 Scanning-based characterisation techniques

Scanning techniques rely on point-by-point scanning across the specified area of a device. The measured signal acquired at each point is recorded in a 2-D data array with a Cartesian coordinate pair in accordance with the real position. Laser beam induced current (LBIC) is a scanning characterisation techniques that has been given much attention since its development [7, 8, 78-107].

The first development of LBIC system dates back to 1981, Miller *et al*. [78] used a He-Ne laser with a mirror to achieve the scanning over a 30 cm × 120 cm area for detecting cracks and shunts in c-Si PV modules. For about 20 years, blue and red lasers were commonly used in LBIC systems [80, 83, 84] until Carstensen *et al*. reported in 2000 [86] that a near-infrared (NIR) laser in their CELLO (Solar Cell Local Characterisation) system to measure charge carrier life times. CELLO enables identification of local shunts and estimation of series resistances. Kress *et al*. in 2000 [87] reported an LBIC setup with two NIR lasers, which was designed for investigating emitter wrap-through in PV cells. A multi-laser setup was seen in the work of Michel *et al*. [92] in which blue, red and NIR lasers were mounted for more detailed failure analysis of PV devices. This system was then further utilised by Vorosayan *et al*. [7] for the characterisation of thin film modules. There are also commercial LBIC systems that provide means of inspection in the PV industry [105, 106]. However, due to the long processing time for high-resolution measurements, LBIC can hardly be a competitive candidate for in-line applications.

A typical LBIC system is operated in CREST and the schematic is demonstrated in Figure 2.18. An LBIC system normally consists of a lock-in control unit, light sources, an optical system, light and electrical biases, a movement system and a data acquisition system. A chopped scanning light (laser) beam is used to generate free e^--h^+ pairs and the current flowing out of the DUT is measured by the lock-in technique to eliminate the influences of the background light and to enhance the signal-to-noise ratio. Multiple light sources can be used to provide beams of different wavelengths to measure at varying abortion depths in the DUT and ultimately to measure the localised external quantum efficiency (EQE). The power of the laser beams needs to be limited in LBIC systems to prevent excessive heat generation and

damaging the DUT. The diameter of the laser beam can be adjusted by an optical system, e.g. an aperture or a focusing system. Scanning of the light beam over the DUT is realised by either controlling a mirror (for large modules) to guide the laser beam or an X-Y table (for small samples) to carry the DUT or light source. External light and electrical bias are sometimes needed to set up some specified test conditions by shifting the operating points. The local photocurrent is collected and recorded in a 2-D current map. The spatial variation of the local current is used to locate the defects in the DUT and can help identify the type of defects. It is especially effective to reveal defects that cannot be visually detected, e.g. cracks and local shunts, and can be further extended to extract the maps of local carrier lifetime and diffusion length [8, 105, 106].

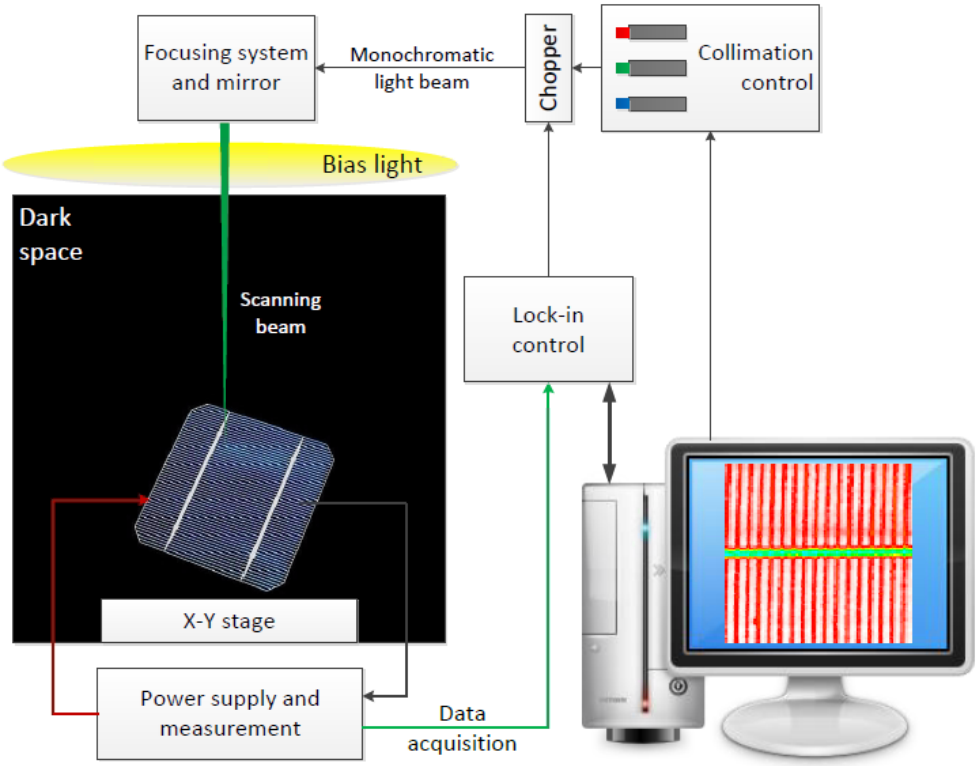

Figure 2.18. Schematic of the LBIC system in CREST [7]. An LBIC system normally consists of a control unit, light sources, an optical system, light and electrical biases, a movement system and a data acquisition system.

Another concern about LBIC is the electrical mismatch effects in PV modules may lead misinterpretation of the measurement results. Conventional LBIC measurements are carried out in the dark or under a background light, referred to here as dark-LBIC (d-LBIC) and illuminated-LBIC (i-LBIC) respectively. However, as

detailed earlier, the overall current output of a module is limited by the cell with the worst performance due to mismatch effects among cells. Both the dark environment and the non-uniform illumination can bring mismatch in terms of the non-uniform local irradiance, and therefore the current output of the light source does not reflect the behaviour of the cell being scanned. To improve the LBIC measurement technique, a limited-illuminated-LBIC (li-LBIC) method was developed [100]. In li-LBIC, variations in the bias light are introduced to the cell being scanned, making it the limited component in the module. Consequently, the overall current output becomes sensitive to the photocurrent generated from the limited cell and prevents misinterpreting of the results caused by the mismatch effects. However, it requires moving the shaded area and to accomplish the full-area scanning.

To summarise, characterisation by scanning techniques has been proven feasible for testing PV cells, although the time issue makes it not an effective option for in-line applications. It is useful for laboratory cell testing where testing time is less critical. To compromise, local area inspection or line scan can be set to gain a relatively faster measurement speed. But after all, scanning techniques like LBIC do not show sufficient competitiveness to handle full electrical characterisation tasks in-line. Nevertheless, scanning techniques can be used for verifying newly-developed characterisation methods [108].

2.5.3 Imaging-based characterisation techniques

In imaging characterisation techniques, image sensors e.g. CCDs (charge-coupled devices) are used to capture the emission profiles. CCDs are sensitive to the emission from radiative recombination or the heat generation. The local emission intensities of the whole testing area are recorded simultaneously, allowing the measurements to be done in a short period of time. The emission profiles of the areas with defects show distinguishing features comparing with those of the intact areas.

Popular imaging characterisation techniques include electroluminescence (EL), photoluminescence (PL) and lock-in thermography (LIT) [77, 109-113]. These techniques do not have long history serving the PV world as spatially-resolved characterisation tools, but have drawn increasing attentions in recent years. LIT was introduced for testing PV cells in 1994 and then has been further developed by

Breitenstein *et al*. as a powerful characterisation method [114]. EL and PL are even younger than LIT, being published for the first time in 2005 by Fuyuki *et al*. [9] and in 2006 by Trupke *et al*. [10], respectively.

LIT detects and shows the heat generated from a PV cell under a periodic electrical bias under dark (dark LIT or DLIT) or a light bias (illuminated LIT or ILIT) [115] by lock-in techniques. It therefore requires a special camera with a thermal sensor. EL is also carried out in the dark but is with a constant electrical bias to record band-to-band radiative recombination. Unlike DLIT, EL does not require lock-in techniques when obtaining the emission profile [9]. PL uses monochromatic lights as excitation and therefore allows contactless tests for PV cells or even wafers [10, 116-120]. Band-pass filters are needed to eliminate the excitation light before the emission is recorded by the imaging sensor. A typical EL system setup is shown in Figure 2.19. It shows the basic experimental setup of an imaging characterisation system. For example, for DLIT measurements the constant current bias can be replaced by a periodic current source with lock-in setup; for PL, a light source can be used as the source of excitation.

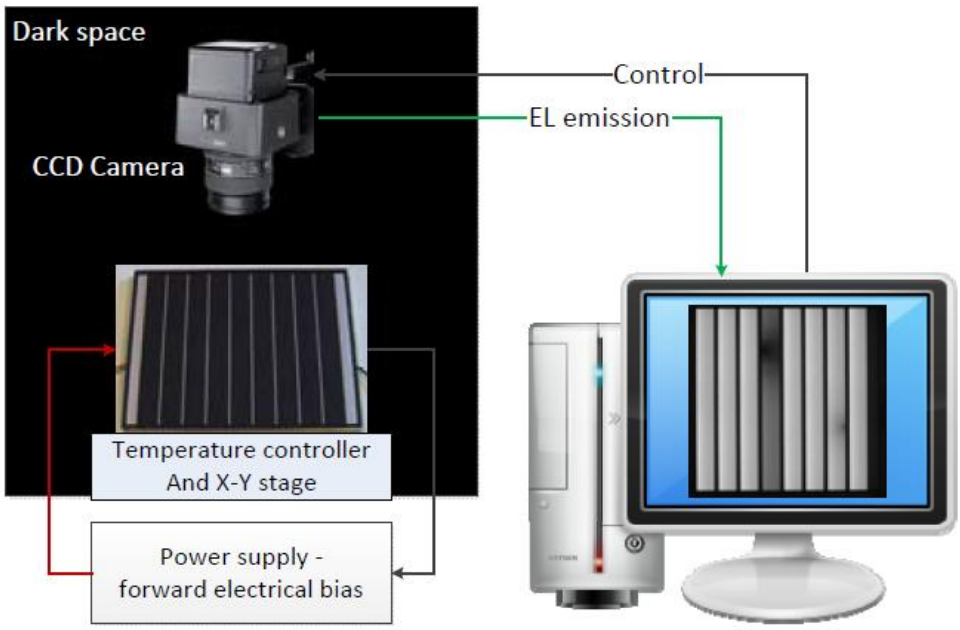

Figure 2.19. Schematic of an EL system. The EL measurements are carried out in the dark. NIR Light emission from the radiative recombination is excited by the external electrical bias applied at the terminals of a PV cell. This schematic shows the basic experimental setup of imaging characterisation systems.

Unlike scanning techniques in which absolute current or voltage values are measured, imaging techniques are naturally qualitative. The relative signal strength corresponds to the brightness of each pixel. An image shows the relative spatial variations in the DUT. It produces a mixed effect of inhomogeneities, which can contain various fault mechanisms from series resistances, shunts, etc. To access the localised electrical properties, i.e. to learn how the local parameters are influenced, a quantitative characterisation is required. A quantitative characterisation technique aims to describe the DUT in a spatially-resolved fashion so that the measured features can be reconstructed by using an SRM. For this reason, an image normally needs to be calibrated before a parametric characterisation can be achieved [121]. Efforts have been made to analytically identify and separate the influences of possible defects such as low diffusion length [122], high series resistances [123], and shunts [59]. But there is no method that can uniquely quantify every loss mechanism. Furthermore, quantitative characterisation methods (will be detailed in Section 2.5.4) often require complicated algorithms that involve large matrix computations or iterations [124] and thus can be time-consuming. Consequently, for applications with certain time restrictions e.g. in-line quality control, qualitative characterisations are more appropriate to meet the critical time requirements [125].

Since LIT can be costly due to the expensive image sensors and the relatively longer image acquisition time, attention has been paid to replacing LIT by cheaper and faster EL or PL systems for certain characterisation tasks. Kasemann *et al*. and Trupke *et al*. reviewed LIT and EL/PL as general spatially-resolved characterisation tools [118, 126] and concluded that ILIT suits better for the localisation of shunts, since the shunted regions may appear to be blurred in luminescence images as an inherent disadvantage. In 2011, Breitenstein *et al*. further investigated these imaging techniques with the topic “Can luminescence imaging replace lock-in thermography on solar cells?” and published a more detailed review [127], indicating that LIT and EL/PL measurements are complementary to each other and should be used in combination. A summary of the utilisation of LIT and EL/PL was given by means of a rating table (Table 2.1).

Table 2.1
Rating of imaging techniques (LIT, EL and PL) as general spatially-resolved parametric characterisation tools [127]

Item	LIT	EL/PL
Lifetime in wafers	+	++
Trapping centres	++	--
Defect luminescence	--	++
Metal-boron pairs	+	++
Bulk defects in cells	+	++
Weak ohmic shunts	++	-
Strong ohmic shunts	++	+
Cracks	+	++
Series resistance	-	++
Local *I-V* characteristics	++	-
Breakdown sites	+	+
Breakdown analysis	++	+
Note:	"++" = "very appropriate"; "+" = "appropriate"; "-" = "less appropriate"; "--" = "not appropriate".	

2.5.4 Quantification of imaging characterisation techniques

Series resistance and shunt imaging are useful for assessing the material qualities of PV cells. In many cases, the local series resistance in a PV cell is defined as the local voltage drop between the terminals and the local equivalent diode, divided by the local current [127]. This is an "effective" series resistance that contains the effects of both the internal R_s and the lateral resistances from the contact schemes. The basic thinking behind these methods is that every pixel corresponds to a sub-cell that is connected to the cell terminal via a single series resistance i.e. the effective series resistance. Comparative measurements e.g. EL with DLIT [19], or differential operations, i.e. EL/PL under different excitation levels [20, 108, 128, 129] were carried out to compensate the calibration processes. An analysis of the applicability will be given in Chapter 5.

Detecting shunts is another popular utilisation of imaging techniques [59, 119, 123, 130, 131]. A shunt can be a hot spot in LIT images due to the relatively high local power dissipation and can be a dark spot in luminescence images because of the change from local radiative recombination to a direct current path. Nonlinear shunts were also reported. The diode-like shunts are active only when the cell is reverse-

biased, therefore reversed current biases were introduced during the imaging processes [123, 132, 133]. Since a strong shunt can be directly identified from an image, the imaging techniques are efficient for qualitative inspection of shunts in PV devices [109, 130, 134-136]. Several authors managed to move a step forward to quantify shunt values by establishing the theoretical relationship between the local electrical characteristics and the measured local signal strength in the images [109, 112, 137]. Rau's reciprocity theorem [138-140] links the EL and EQE measurements, by which attempts for extracting *I*-*V* characteristics were made [110].

As a step forward ahead the resistive imaging, the full characterisation of a PV sample is supposed to provide sufficient parameters to reconstruct its behaviour by a 2-D SRM. However, there are certain major challenges hiding behind this straightforward expectation and need special attention. Firstly, high-resolution experiments produce huge unknown variable sets. Take a distributed model with the single-diode mode for example, there are normally four parameters, i.e. I_{sat}, n, R_s and R_{sh} [see Equation (2.5)], to determine for each local sub-cell. These parameters have nonlinear relationships with the local operating points. Secondly, the measurement results, e.g. luminescence images, demonstrate mixed effects of local electrical properties. Therefore the separation of these composited factors needs to be considered in characterisation. Thirdly, the validity of the extracted parameter sets should be examined properly to prevent false convergence due to e.g. local minima, especially in iterative methods. In addition, time effectiveness may be of interest in specific applications e.g. in-line quality control.

There have been quantitative characterisation methods, with different emphases in terms of the above-mentioned challenges [11, 19, 20, 108, 116, 124, 128, 129, 141-146]. A list of influential research papers is chronologically reviewed in Table 2.2. It can be seen from the list that attempts have been made on all the electrical parameters relate to the single- or double-diode models. However, none of these methods can achieve a full set of local parameters.

Two recent (2013) pieces of work [108, 116] provide results that are close to the "full characterisation" based on the double-diode model using PL, with the assumption that the light generated current density is uniform across the sample.

But both methods failed to manage R_s and R_{sh} at the same time. The reason for this was illustrated by Breitenstein *et al*. [124] in his quantitative analysis of EL images, stating that the influences of R_s and R_{sh} cannot be uniquely separated, which also explains the reason why in most R_s extraction methods [19, 20, 108, 128, 129] the influences of local R_{sh} are neglected. The effective R_s discussed earlier attracted a number of research works. It provides an effective way for the model to link the local operating points, even though the sources of the local R_s remain undefined, although its validity has not been fully proven yet. Moreover, the uniform light-generated current density and n = 1 for single-diode models are also common assumptions [124, 128, 129] and potential over-simplifications.

In the point of view of measurement techniques, luminescence imaging predominates. For extracting R_s, most PL measurements were carried out with external electrical biases or irradiance biases [20, 108, 116, 129], enabling differential operations. This is necessary for PL because the original experimental setup operates under V_{OC}, and does not supply injection current to intensify the variations caused by the series resistances, especially the lateral resistances in large-area thin-film cell. Homogeneous local light generation is a widely used assumption in PL-based characterisation methods [20, 108, 116, 145], which significantly simplified the calculation processes by reducing the number of variables. Comparatively, EL and LIT seemed to be more natural to produce measurement results consisting of the effects from lateral resistances, although it can take extra efforts to distinguish the power dissipation, i.e. the heat generation, from different types of resistances and thus additional assumptions may be used [19].

2.6 Chapter conclusions

In this chapter, the fundamentals of PV cells, modelling and characterisation are reviewed. A PV cell is an electrical device that converts the energy in light into electricity. The output of a PV cell is the result of a subtle balance among light absorption, current generation and charge recombination. e^--h^+ pairs are generated by the incident light. The electric field across the semiconductor junction separates the electrons and holes and sweeps them to the external circuit via the terminal of the cell before recombination.

The global electrical behaviour of a PV cell can thus be described by a lumped diode model and the corresponding *I*-*V* characteristics. A set of performance indicators can be used to evaluate the effects of the flaws in the devices. However, lumped characterisation cannot provide information about spatial inhomogeneities in cells. Therefore spatially-resolved characterisation techniques with distributed models should be applied to describe the behaviour of PV devices.

Imaging spatially-resolved characterisation techniques are recently popular not only in laboratories but also in production lines for their much higher speed than scanning methods. However, since imaging techniques are naturally qualitative, extra efforts need to be made for quantifying the measurement results. Moreover, to identify and to separate the source of inhomogeneities is also challenging.

The use of SRM can link the experiment results to the localised electrical properties by introducing an array of virtual sub-cells where each represents a finite area of the PV material. The SRM of a cell is a discrete circuit network to be solved numerically e.g. by simulation tools like SPICE derivatives, which may undergo complicated preparation and long processing time. The existing quantification methods of imaging techniques rely on various assumptions and simplifications which have not been fully proven yet.

To overcome these issues, the following chapters will illustrate the development of a fast solver for a 2-D SRM, which will be used for a fitting algorithm that can extract localised electrical parameters from dark *I*-*V* and EL measurement results, without e.g. using the effective R_s. The characterisation results can be further used to quantify flaws e.g. shunts.

Table 2.2

List of quantitative electrical characterisation methods based on imaging techniques

First author (Year)	Parameters	Measurement techniques	Brief description	Major assumptions	Ref.
Breitenstein (2003)	I_{sh}, J_{sat}, n	LIT	Local *I-V* characteristics are measured thermally. The current through a local shunt (I_{sh}) is measured quantitatively; the mapping of n and J_{sat} over the whole cell are provided.	Not specified	[11]
Trupke (2007)	R_s	PL	Strong lateral variations of the series resistance are determined by PL images measured under different voltage biases.	The local diode voltages are assumed to be the same as the terminal voltage; n = 1 is used; R_{sh} is not considered.	[129]
Ramspeck (2007)	I_{rec}, R_s	EL + LIT	The local recombination current (I_{rec}) and R_s maps are obtained by pixel-by-pixel processing an EL image and an LIT image measured under the identical operating condition.	Heating caused by the current flowing through R_s is neglected; R_{sh} is not considered.	[19]
Hinken (2007)	R_s	EL	The method combines the local EL emission and its derivative with respect to the applied voltage bias, and yields the effective R_s map.	The local diodes are assumed to have n = 1; local R_{sh} is not considered.	[128]
Kempwerth (2008)	R_s	PL	The method evaluates local effective R_s values by differential PL, without accessing the local calibration constants.	The light-generated current density is homogeneous across the cell and equals to the J_{sc}.	[20]
Glatthaar (2009)	I_{sat}	EL	The local I_{sat} is determined from two EL images taken at two voltage levels by deriving local voltage and current distribution with the emitter sheet resistance.	Not specified	[142]

Table 2.2 (continued)

First author (Year)	Parameters	Measurement techniques	Brief description	Major assumptions	Ref.
Breitenstein (2010)	R_s, J_{sat}	EL	An iterative procedure is developed to calculate R_s and J_{sat} images from two EL images taken at two bias conditions. However, R_s variations cannot be uniquely separated from R_{sh} variations.	The local diodes are assumed to have n = 1; a scaling factor f is assumed to be same for all positions.	[124]
Breitenstein (2011)	J_{sat1}, J_{sat2}, n_2, R_{sh}	DLIT	J_{sat1}, J_{sat2}, n_2, R_{sh} for local double-diode model can be obtained by evaluating DLIT images taken at different bias conditions: 3 forward biases and 1 reverse bias.	Not specified	[146]
Seeland (2012)	R_{int}, R_{sheet}	EL	Internal resistance (R_{int}) and sheet resistance (R_{sheet}) for a one-dimensional network model can be derived from the EL result that is averaged over the width of the sample.	The cell is described by a one-dimensional model.	[143]
Hameiri (2013)	V_{OC}, pFF, J_{sat1}, J_{sat2}, R_{sh}	PL	Distributed implied V_{oc}, pFF (pseudo fill factor), J_{sat1}, J_{sat2} and R_{sh} of silicon wafers or wafer-based solar cells can be extracted by fitting the local pseudo I-V curves via a contactless "Suns-PL" method.	The light-generated current density is uniform across the sample.	[116]
Shen (2013)	R_s, J_{sat1}, J_{sat2}, η, FF	PL	Local parameters based on a double-diode model including R_s, J_{sat1} and J_{sat2}, as well as local efficiency (η) and FF are extracted from at least 5 PL images measured under different operating conditions.	The light-generated current density is homogeneous across the cell and equals to the J_{sc}; R_{sh} is neglected.	[108]
Fertig (2014)	J_{SC}	LIT	A quantitative map of J_{SC} is extracted from the difference of two power-calibrated ILIT images and one DLIT image.	J_{SC} does not differ significantly from the illuminated current under moderate reverse bias.	[144]

Table 2.2 (continued)

First author (Year)	Parameters	Measurement techniques	Brief description	Major assumptions	Ref.
Hallam (2014)	implied V_{OC}	PL	Spatially-resolved implied V_{OC} values are determined by applying the local calibration constants from quasi-steady-state photo-conductance measurements on partially processed cells and *I-V*s on finished cells.	The photogenerated excess carrier density is constant throughout the bulk of the wafer.	[145]

Chapter 3

Accelerated spatially-resolved electrical simulation of PV devices using PV-oriented nodal analysis

3.1 Overview

The previous chapter reviewed the modelling and characterisation methods for PV devices, and identified that an efficient algorithm for solving 2-D SRMs (Spatially-resolved models) is useful for quantifying e.g. imaging characterisation techniques. This current chapter elaborates the development of such a simulation tool, namely the PV-oriented nodal analysis.

As introduced in the previous chapter, the 2-D modelling techniques take the spatial nature of devices into account. Predominantly, they are done by circuit simulation tools e.g. SPICE (Simulation Program with Integrated Circuit Emphasis) derivatives. Galiana *et al*. [71] presented a model with detailed parameterisation for concentrator PV cells and demonstrated its fidelity on depicting localised properties. Eidelloth *et al*. [16] proposed an elaborate model structure for wafer-based cells with metal contact grid. However, the case study of a 400 × 400 nodes simulation required 5 GB memory space and 8 hours calculation time for a single bias condition. Vorasayan *et al*. [62] and Ott *et al*. [64] implemented simplified model structures and achieved simulations for mismatched thin-film modules. But the immense memory usage and computation time rules them out for high-resolution (e.g. mega-node level) simulations.

More specifically, SPICE-based approaches require significant amounts of memory and are very slow in terms of execution times. Calculation times increase quadratically with the number of nodes[1]. This can make the simulation of e.g. a full-resolution EL image take many hours or even longer. Recently, simulation approaches based on the finite element method (FEM) have been proposed [147] for 2-D modelling of PV cells with high computational speeds, based on advanced meshing strategies. The meshing may reduce computational loads when carrying out simulations but does not link directly to measurements taken e.g. by a camera. It thus needs to be adjusted in a case-by-case basis as it otherwise might lose information of defects in the 'wrong' locations. Pieters [12] introduced a variable meshing system to adjust the resolution for being able to describe complicated geometric patterns of the contact grid in reasonable memory requirement and computation time [148]. But

[1] A "node" in a circuit is a point where elements or branches connect through their terminals.

similarly, adjustments are required for linking the meshes with different area to e.g. the pixels of an EL image.

Thus it is necessary to implement modelling with regular (i.e. square) meshing and SPICE-like simulation to generate understanding of inhomogeneities in PV devices. To achieve this, it is vital to develop an efficient solver. There are optimised algorithms such as KLU [149, 150], SuperLU [151], NISCLU [152] etc. developed to accelerate general circuit simulations by being integrated with the SPICE core. Optimised SPICE derivatives such as Spice OPUS [153] are also available. However, SPICE tools require complicated preparation (e.g. generating and parsing netlists[2]). Moreover, they are ineffective in terms of the interfaces with other simulation tools or functions which may be used for e.g. iterative characterisation algorithms.

A PV-oriented nodal analysis (PVONA)[3] is presented in this chapter. It contains a flexible set of tools and allows efficient 2-D simulations of PV cells and modules. This is achieved by integrating a specifically designed sparse data structure and a graphics processing unit (GPU)-based parallel conjugate gradient algorithm into a PV-oriented Newton-Raphson solver. Here, two commonly used SPICE derivatives, PSpice (v16.6) and LTSpice (v4.22) (discussed in Section 2.5.1), are used for comparison, to demonstrate the improvements of PVONA in terms of the efficiency on solving high-resolution (e.g. mega-sub-cell level) SRMs. Tests are done on a normal PC with a consumer-level graphics card. The test cases demonstrated in this chapter use only about 5% of the time required by both the LTSpice and PSpice versions used for comparable simulations. The approach could be easily deployed on various high-power parallel computing platforms and achieve further time savings. This would allow deployment in industrial applications.

[2] A "netlist" describes the connectivity of an electronic design. In circuit simulation software e.g. SPICE, a netlist is a list of all the component terminals that should be electrically connected for the circuit to work.

[3] PVONA is developed in C.

3.2 Spatially-resolved model structure

3.2.1 2-D spatially-resolved model for PV cells

2-D Spatially-resolved modelling allows the investigation of the local electrical properties in a large-area single-junction device. The local characteristic of a PV cell can be described by a Poisson problem as given by Equation (3.1),

$$\nabla^2 \boldsymbol{V} = \boldsymbol{J}(x, y, V) R_{\blacksquare}(x, y) \tag{3.1}$$

where ∇^2 is the Laplace operator; $\boldsymbol{V}$ is the local electric potential difference between the front and back contacts; $\boldsymbol{J}(x, y, V)$ is the local current density; $R_{\blacksquare}(x, y)$ is the local lateral resistance; and the boundary conditions were given in [12]. However, analytically solving the continuous Poisson equation e.g. using a Green's function is inefficient. Therefore, using circuit simulation to solve a discrete equivalent circuit model, i.e. an SRM, becomes a commonly accepted alternative.

An SRM of a PV cell is composed by an array of finite areas, i.e. sub-cells, where each one is an analogue of a segment of the PV material. As sketched by Figure 3.1a, each sub-cell (a block with an arrow) represents a rectangular-shaped segment of the bulk, while the resistor networks on the top and the bottom represents the front and back contact schemes, respectively. The front contact layer is connected to the positive terminal while the back contact is connected to the negative terminal, which is set as the reference node of the circuit with V_{REF} = 0 V.

Since the resistivity of the metal contact is low and can be assumed uniform, the back contact scheme is neglected in the development of the accelerated PVONA, as done in [58, 71] and demonstrated in Figure 3.1b. The benefit of this simplification will be seen when constructing the nodal equation system (Section 3.3.1). Nevertheless the back contact can be easily added to the network (as shown later in Figure 3.4).

The front resistor network can be configured to suit both the contact grid for wafer-based cells and the transparent conducting oxide (TCO) sheet for thin-film devices, as illustrated in Section 2.2.4. Figure 3.2a and b demonstrate voltage maps of a thin-film cell and a wafer-based c-Si cell, respectively. The variations shown in the voltage maps are due to the voltage drop on lateral resistances in the TCO in thin-film cells

and the emitter layer in c-Si cells. The description of lateral variations like this distinguishes SRMs from lumped models.

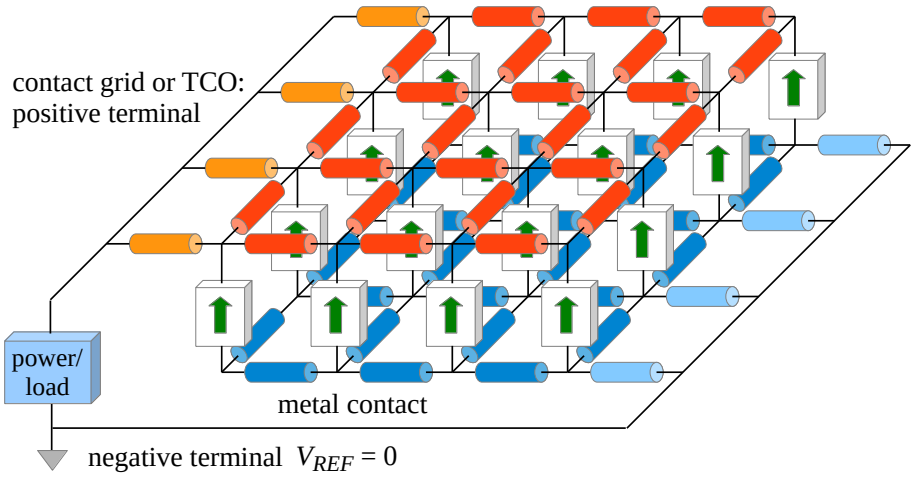

(a)

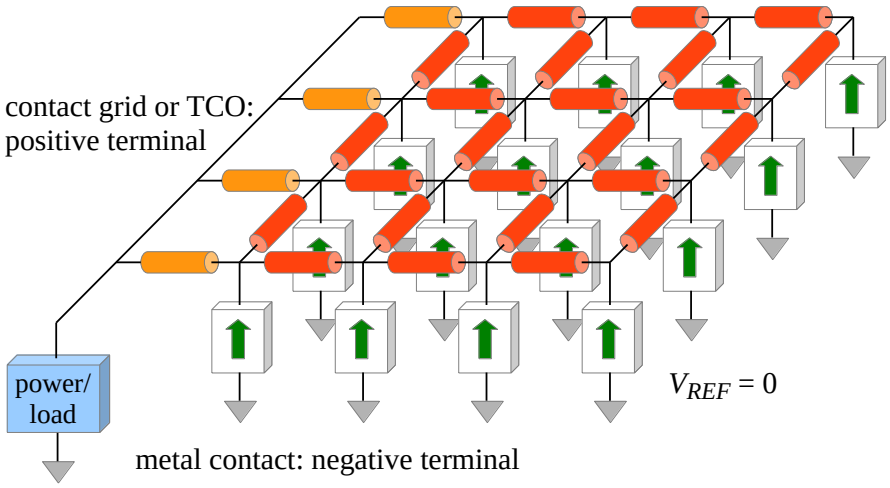

(b)

Figure 3.1. (a) Schematic diagrams of the spatially-resolved model (SRM). An SRM is a discrete nonlinear circuit network that consists of a front contact layer, a back contact layer and an array of local diode models. (b) For optimisation, the resistances in the metal back contact are neglected in PVONA.

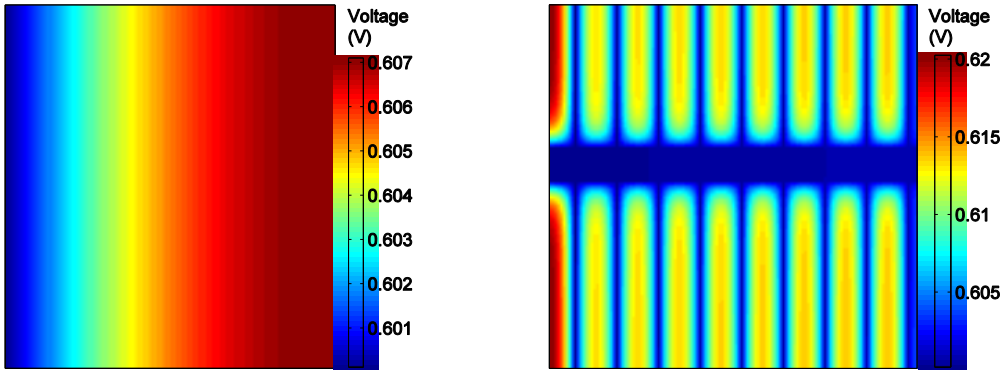

(a) (b)

Figure 3.2. Voltage maps of (a) a thin-film cell and (b) a wafer-based c-Si cell. The variations shown in the voltage maps are due to the voltage drop on lateral resistances in the TCO in thin-film cells and the emitter layer in c-Si cells, which distinguishes SRMs from lumped models.

3.2.2 Local sub-cells

To organise a network model, the concept of "sub-cell" is introduced. A sub-cell is the elementary component of the SRM, as shown in Figure 3.3a. The size of the sub-cell array is determined by the required resolution of the SRM. For a sub-cell, there are two resistors radiating to the "west" and "south" from the top node. These two resistors represent the local sheet resistance of the front contact. If the back contact is considered, as shown in Figure 3.3b, two resistors radiating to the "south" and "east" from the bottom node to represent the metal back contact. If a sub-cell is in the column at the west (and the east edge in a full model), i.e. connected to a terminal, the lateral resistance is reduced by half comparing that used in elsewhere, to match the shortened lateral current pathway (half of a node-to-node pathway).

The "PV unit" in the sub-cell model is a local diode model that represents the material behaviour. As introduced in Section 2.3, various diode models are available to match the properties of different semiconductor materials used in PV devices. The single-diode model, as shown in Figure 2.7, is used for demonstration purposes in this thesis. The *I-V* characteristic of the single-diode model was given by Equation (2.5) in Section 2.3. It can be replaced easily by other types of diode models e.g. double-diode model or Merten's model [45] for different material types.

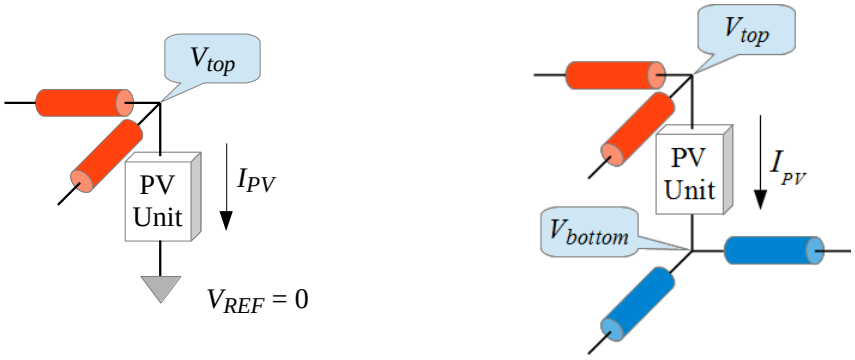

(a) (b)

Figure 3.3. Schematic diagrams of the sub-cell model (a) without and (b) with the consideration of the lateral resistances in the back contact layer. The PV unit is the core of a sub-cell and is modelled by a local diode model.

3.3 Sparse PV-oriented nodal equation system

3.3.1 Nodal equation system and sparsity

Nodal analysis (NA) is the most common way to solve the network models in circuit analysis software [154, 155] e.g. SPICE. In a circuit network, a "node" is a point where circuit components or branches connect. Nodal analysis is a method of determining the potential difference between nodes. For nodal analysis, a nodal equation system (NES) will be generated by applying Kirchhoff's current law (KCL) to each node by applying Equation (3.2)

$$\sum_{b=1}^{N} I_b = 0 \tag{3.2}$$

where N is the total number of branches connected to the node. I_b represents the current flowing in each circuit branch from or to the node. If the current is flowing into the node, I_b will be a positive value; if the current is flowing out of the node, I_b will be negative.

Rearranging the NES gives the matrix-vector form as Equation (3.3)

$$\boldsymbol{GV} = \boldsymbol{I} \tag{3.3}$$

where $\boldsymbol{V}$ is the unknown vector containing all node voltages; $\boldsymbol{G}$ is the admittance matrix and $\boldsymbol{I}$ is the current vector containing all the independent current sources. The target of NA is to solve the node voltages $\boldsymbol{V}$, through which all the local operating conditions in the circuit can be derived.

As an example, the formulation of the NES of an SRM with 3 × 3 sub-cells is demonstrated in Figure 3.4. There are 19 nodes in the NES, in which there are 9 nodes for both the front and the back contact layers, numbered as 1 to 9 and 10 to 18, respectively. The positive terminal is numbered as 19. A sub-cell, e.g. the one at the 2nd row, 2nd column in the array, can have at most 4 neighbouring sub-cells. To formulate the NES, KCL [Equation (3.2)] is applied to each node. I_{eq} and R_{eq} are the effective current source and the effective resistance respectively derived from the *I*-*V* characteristic of the local PV unit in the linearisation stage (will be discussed in Section 3.4.2). If the lateral resistances in the back contact are neglected, all the PV units will directly connect with the reference node, i.e. without formulating node No. 10-18 in this example. R_{ij} represents the resistance between the *i*-th node and the neighbouring *j*-th node. By rearranging, each KCL equation can be expressed as a linear combination of the unknown node voltages on the left hand side, with the current source on the right. Therefore all the nodal equations can be formatted into the matrix form as Equation (3.3).

Special features can be found in the NES's for the SRMs. The entries in the admittance matrix $\boldsymbol{G}$ represent the ohmic interconnections between adjacent nodes in the circuit by Equation (3.4)

$$G_{ij} = \begin{cases} \sum_{b=1}^{N} \frac{1}{R_{ib}}, & i = j \\ -\frac{1}{R_{ij}} = -\frac{1}{R_{ji}}, & i \neq j \end{cases} \tag{3.4}$$

where $1 \leq i, j \leq$ the number of nodes; N is the total number of branches connected to the *i*-th node; and R_{ij} represents the resistance between the *i*-th and *j*-th nodes. Entries on the diagonal represent self-admittance while non-diagonal entries represent additive inverse of the mutual-admittance. Therefore, $\boldsymbol{G}$ is firstly symmetric; and secondly highly sparse when the size of the SRM is large.

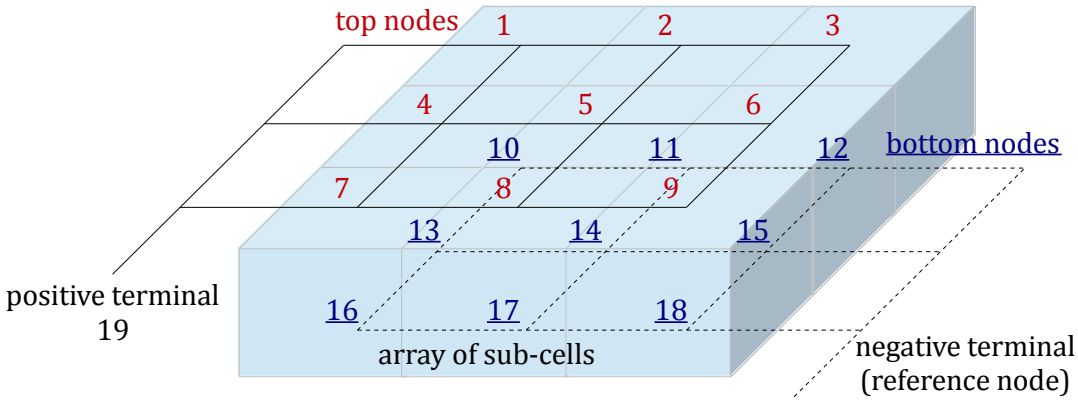

(a)

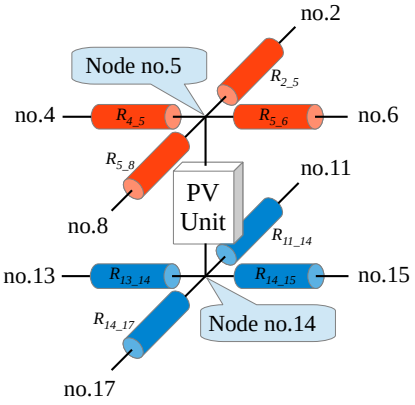

KCL form:

Node no.5: $\frac{V_4-V_5}{R_{4\_5}}+\frac{V_2-V_5}{R_{2\_5}}+\frac{V_6-V_5}{R_{5\_6}}+\frac{V_8-V_5}{R_{5\_8}}=I_{eq5\_14}+\frac{V_5-V_{14}}{R_{eq5\_14}}$

Node no.14: $\frac{V_{14}-V_{13}}{R_{13\_14}}+\frac{V_{14}-V_{11}}{R_{11\_14}}+\frac{V_{14}-V_{15}}{R_{14\_15}}+\frac{V_{14}-V_{17}}{R_{14\_17}}=I_{eq5\_14}+\frac{V_5-V_{14}}{R_{eq5\_14}}$

Re-organise:

Node no.5: $-\frac{1}{R_{2\_5}}V_2-\frac{1}{R_{4\_5}}V_4-\frac{1}{R_{5\_6}}V_6-\frac{1}{R_{5\_8}}V_8-\frac{1}{R_{eq5\_14}}V_{14}$
$+(\frac{1}{R_{2\_5}}+\frac{1}{R_{4\_5}}+\frac{1}{R_{5\_6}}+\frac{1}{R_{5\_8}}+\frac{1}{R_{eq5\_14}})V_5=-I_{eq5\_14}$

Node no.14: $-\frac{1}{R_{11\_14}}V_{11}-\frac{1}{R_{13\_14}}V_{13}-\frac{1}{R_{14\_15}}V_{15}-\frac{1}{R_{14\_17}}V_{17}-\frac{1}{R_{eq5\_14}}V_5$
$+(\frac{1}{R_{11\_14}}+\frac{1}{R_{13\_14}}+\frac{1}{R_{14\_15}}+\frac{1}{R_{14\_17}}+\frac{1}{R_{eq5\_14}})V_{14}=I_{eq5\_14}$

(b)

Figure 3.4. (a) Schematic diagram of the sub-cell at the 2nd row, 2nd column in a 3 × 3 full model. (b) KCL is applied to both nodes. The KCL equations are re-organised to be expressed as a linear combination of the unknown node voltages on the left hand side, with the current source on the right.

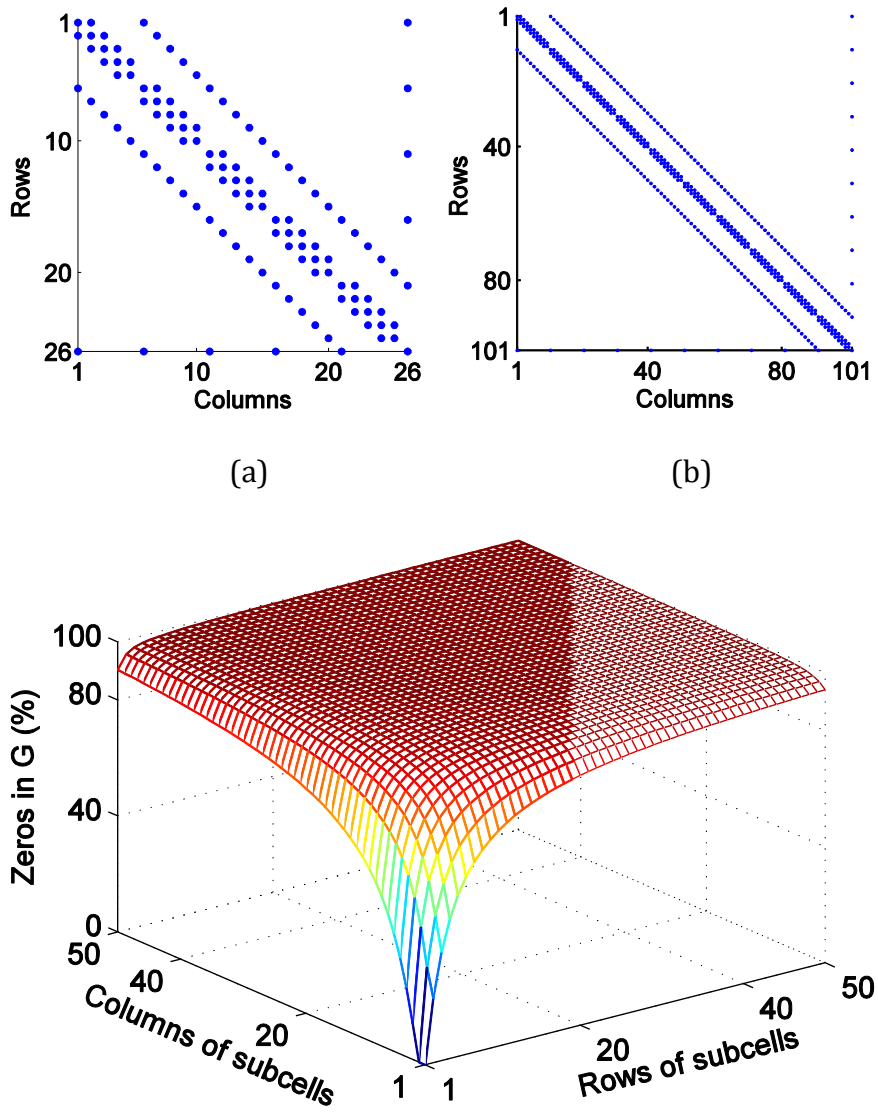

(a) (b)

(c)

Figure 3.5. Pattern of the ***G*** matrix of an NES for a standard model containing (a) 5 × 5 sub-cells and (b) 10 × 10 sub-cells. Blue dots (•) represent nonzero entries, showing highly sparse matrices. (c) The number of zero entries increases dramatically with the size of the sub-cell array.

Figure 3.5a and b show the patterns of the ***G*** matrices of the NES's for two SRMs. In the model with 5 × 5 sub-cells, 116 entries out of 676 (17.2%) are nonzero; the percentage decreases to 4.7% in the 10 × 10 case. Figure 3.5c displays the change of the percentage of zero elements in ***G*** according to the size of the sub-cell array. In a cell with a 100 × 100 sub-cell array, zeros can occupy 99.95% space of the ***G*** matrix, and the number increases with bigger sizes. These zero elements can cause

considerable waste of memory space on data storage. For example, the dense format of the $\boldsymbol{G}$ matrix for a 100 × 100 model can consume 763 megabytes (MB) if double precision floating point numbers are used. If the size of the model increases to 200 × 200, the memory consumption for the dense $\boldsymbol{G}$ can reach 11.9 gigabytes (GB). In fact, if only the nonzero elements are stored, only 0.4 MB is needed for the 100 × 100 case. Even for a 1000 × 1000 model, the nonzero entries use less than 40 MB. In addition, extra computing power for manipulating zeros will be required in algebraic operations.

The $\boldsymbol{G}$ matrix for the NES of the standard model structure is naturally strictly diagonal dominance [156] by satisfying Expression (3.5)

$$|G_{ii}| > \sum_{k=1,k\neq i}^{MN+1} |G_{ik}|, \qquad 1 \leq i \leq (MN+1) \tag{3.5}$$

Being symmetric and strictly diagonal dominance, $\boldsymbol{G}$ is guaranteed to be positive definite [157]. This special feature is not satisfied in most general circuit simulation scenarios (a SRM including the back contact scheme holds positive semi-definite). This feature enables efficient numerical algorithms to be applied for solving Equation (3.3).

3.3.2 Sparse nodal equation system

For a SRM consists of R rows and C columns, the RC + 1 nodes (one top node for each subcell plus one positive terminal node while the negative terminal is set as the reference) produces a $\boldsymbol{G}$ matrix of the size $(RC + 1)^2$ in which only a very small amount of entries are nonzero. A sparse data structure for the NES (SpNES) is developed and illustrated in Figure 3.6-top.

The SpNES is built based on the "***node***" objects and records only the existing interconnections by two vectors, namely ***Neighbour*** and ***Conductance***. For example, if the i-th node is in connection with the j-th node, then j is attached to ***Neighbour*** as the index and the mutual-admittance (MA) between the two is attached to ***Conductance*** with the same sequence number. The self-admittance (SA) of the node itself is attached as the last element of ***Conductance***. This sparse data structure is a variant of the standard "coordinate list" format of sparse matrix [158]. Each ***node*** can

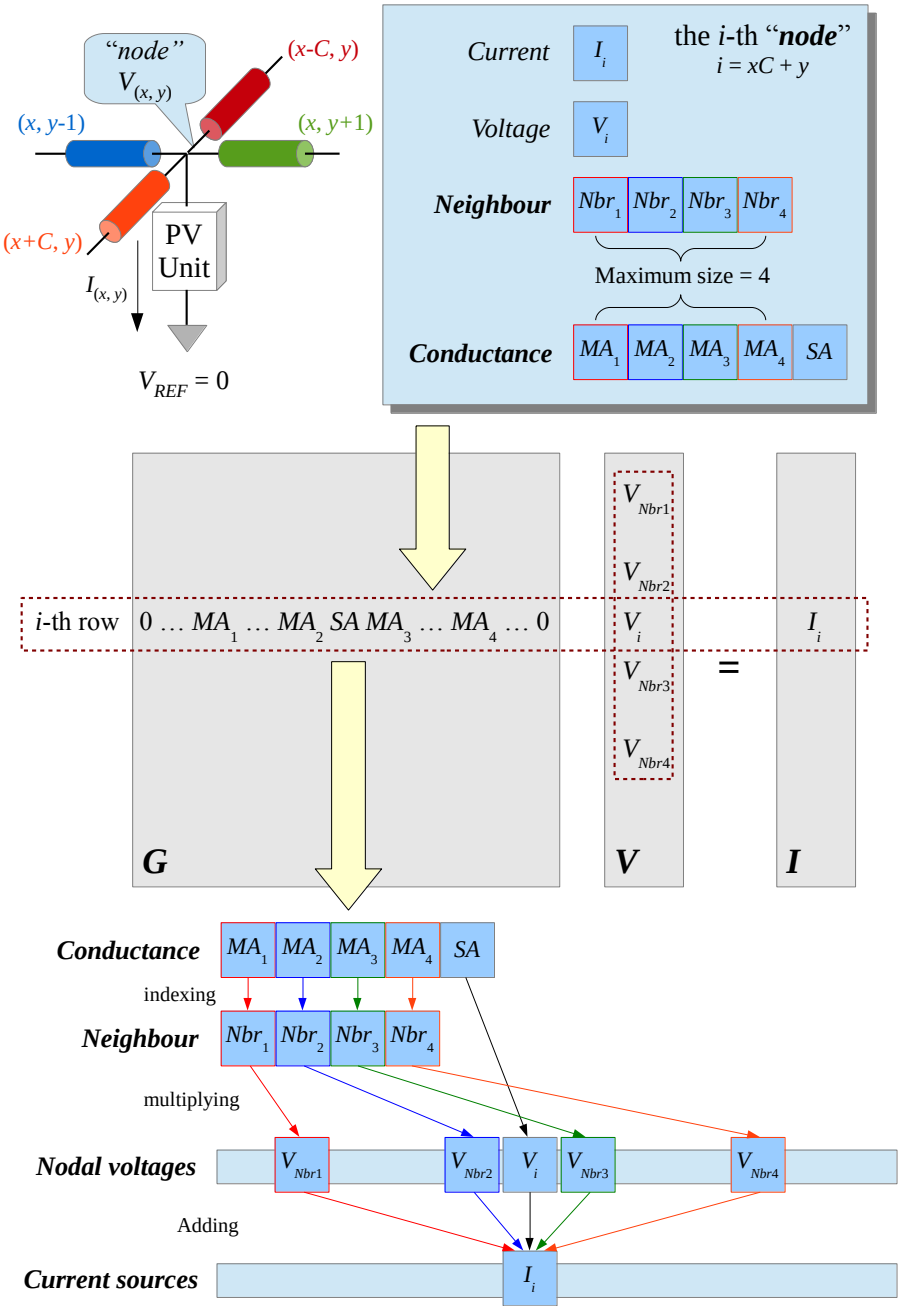

Figure 3.6. Sparse data structure for the NES (SpNES) of the standard model. Top: data organisation of a "***node***" object (*C* is the total number of columns); Middle: the *i*-th node represents the *i*-th row in the ***G*** matrix; Bottom: the indexing system of the SpNES for matrix-vector multiplication.

replace a row of the NES [Equation (3.3)], as depicted in Figure 3.6-middle, where V_i is the node voltage to be solved, and I_i is the local current. The use of SpNES not only significantly saves memory space for large matrices, but also provides a seamless interface to efficient iterative algebraic computing processes e.g. conjugate gradient (as will be shown in Section 3.4.3). The definition of the sparse data structure is attached in Appendix A.1.

3.4 PV-oriented numerical solving procedure

3.4.1 Newton-Raphson iterative loop

The NES of the SRM is a nonlinear system. The most common approach to solve such a nonlinear system is to iteratively solve a sequence of linearised equations, for which the method of linearisation is determined by the nonlinear root-finding algorithm [154]. Newton-Raphson (NR) method is a powerful and popular means for solving nonlinear equation systems [154, 159, 160]. The NR method provides the numerical approximation of the final solution by a series of linearised iterative sequences. For a nonlinear equation system in the matrix format, the iterative NR method can be expressed as Equation (3.6)

$$\boldsymbol{X}_k = \boldsymbol{X}_{k-1} - \boldsymbol{J}^{-1}(\boldsymbol{X}_{k-1})F(\boldsymbol{X}_{k-1}) \tag{3.6}$$

where $\boldsymbol{X}$ is the unknown vector; $\boldsymbol{J}(\boldsymbol{X})$ is the Jacobian matrix; and $F(\boldsymbol{X})$ is the set of nonlinear equations [160].

Figure 3.7 shows the steps of using NR to solve the SRM for one voltage-bias condition. The procedure starts with an initial “guess” for every node voltage. This first approximation will be updated after each iterative sequence. Each local diode model, as a nonlinear component, is then linearised (as the result of Jacobian operation) using the updated operating point derived from the previous approximation. The linearised NES can then be formulated and solved by linear algebra techniques. These steps are repeated until the difference between the solutions from two successive iterative sequences meets the stopping criterion described by Expression (3.7)

$$\|\boldsymbol{V}_k - \boldsymbol{V}_{k-1}\|_2 < \varepsilon\|\boldsymbol{V}_k\|_2 \tag{3.7}$$

where k represents the active iterative sequence; and $\|\cdot\|_2$ denotes the Euclidean norm [154]. A small tolerance value e.g. $\varepsilon = 10^{-6}$ is set to evaluate the convergence. If the number of iterations exceeds the maximum limit and the stopping criterion is still not satisfied, which can be caused by diverging or low converging rate (as will be discussed in Section 3.5), the solving process will abort as a failure. However, PVONA has shown good stability for the simulations using typical parameters for PV devices. *I-V* curves are built up from a pre-determined number of operating points. Specific points could be determined by applying an outer iteration for specific conditions around this.

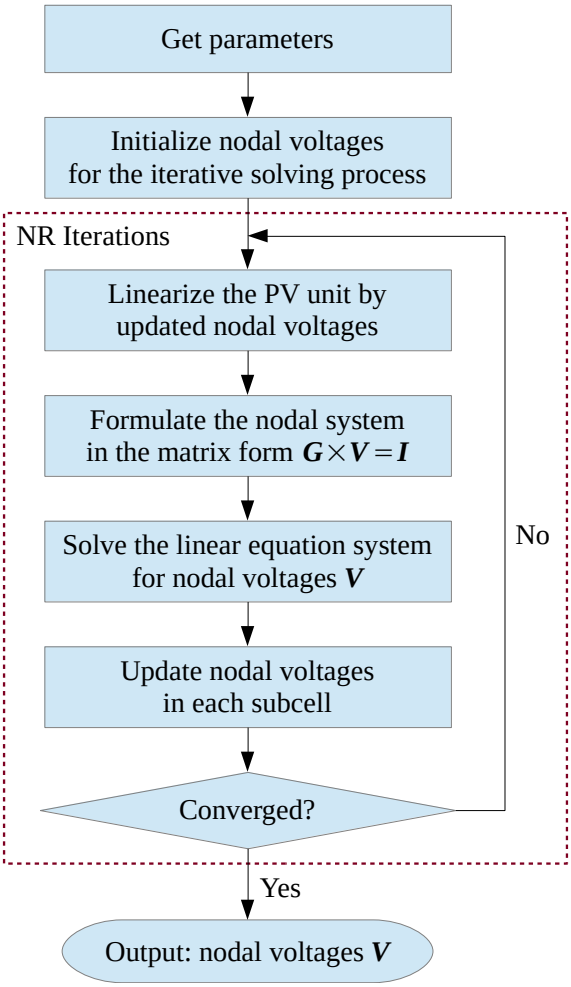

Figure 3.7. Newton-Raphson algorithm for solving one operating point from the NES of a PV cell. It approximates the solution by solving an iterative sequence of linearised equations. An *I-V* curve can be obtained by repeating this procedure within a specified current and voltage range with a certain step width.

3.4.2 PV-oriented linearisation

The linearisation in a NR loop results in calculating the Jacobian matrix of the NES. The PV-oriented linearisation distinguishes PVONA from general-purpose simulation tools. In standard linearisation, each nonlinear component e.g. a diode in the circuit is linearised individually [154]. For example, in a single-diode model, the diode is the only nonlinear component and is replaced by a parallel connection of an equivalent current source (I_{eq}) and an equivalent linear conductance (G_{eq}), in each iterative sequence of the NR solver. In PVONA, the entire diode model is treated as a single entity, as depicted in Figure 3.8. The tangent G_{eq} of the I-V curve is calculated in each NR iterative sequence by the given operating voltage V_x. Only the values for V_x, G_{eq} and I_{eq} need to be updated in each NR loop.

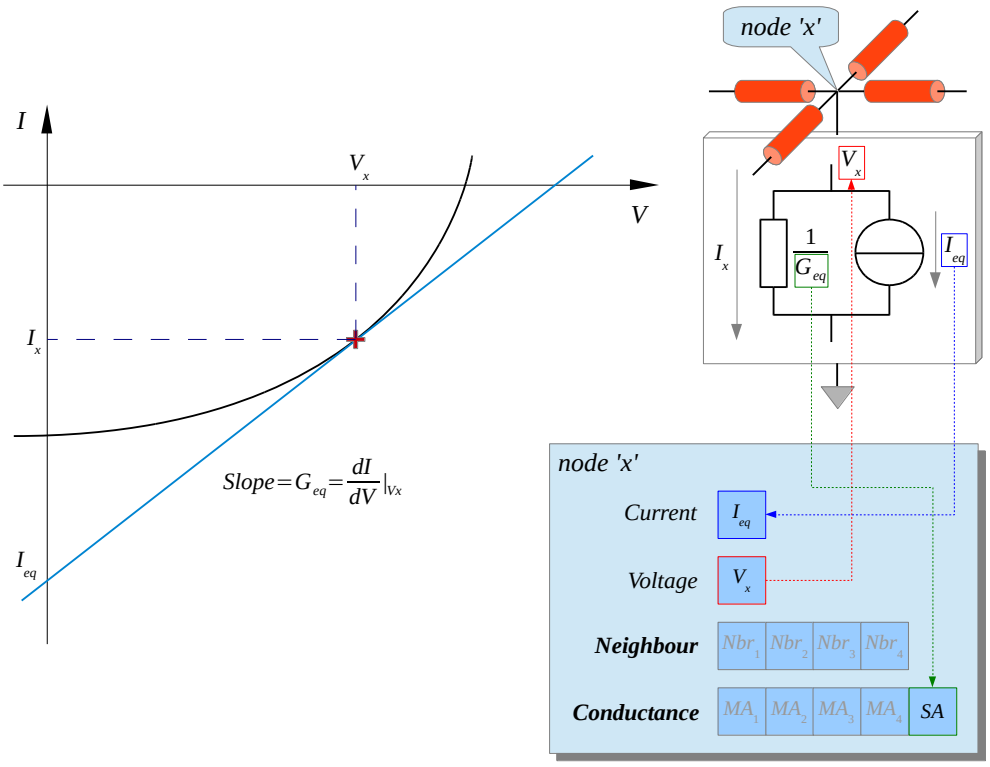

Figure 3.8. PV-oriented linearisation for a diode model. The diode model is treated as a single entity and is replaced by an equivalent resistance and a current source connected in parallel. Linearisation has to be calculated in each NR iterative sequence with the updated node voltages. In each linearisation process, variables I_i, V_i and SA are updated while others remain unchanged.

Equations (3.8)and (3.9) show the G_{eq} and I_{eq} derived from the *I-V* characteristics of the single-diode model

$$G_{eq} = \frac{dI}{dV}|_{V_x} = \frac{\frac{I_{sat}q}{nkT}\exp\left[\frac{q(V-I_xR_s)}{nkT}\right] + \frac{1}{R_{sh}}}{1 + \frac{I_{sat}qR_s}{nkT}\exp\left[\frac{q(V-I_xR_s)}{nkT}\right] + \frac{R_s}{R_{sh}}} \tag{3.8}$$

$$I_{eq} = I_x - G_{eq}V_x \tag{3.9}$$

where I_x is obtained by solving Equation (2.5) with respect to V_x using an inner NR loop. As a consequence, the number of circuit components of each single-diode model is reduced from 4 to 2, while the number of nodes is reduced from 2 to 1. These result in 50% fewer nodes and 43% fewer circuit elements in an SRM in PVONA than in standard SPICE tools, which considerably simplify the NES especially when the size of the SRM is large. The same rule can be easily applied on other types of diode models e.g. the double-diode model and the Merten's model.

3.4.3 Parallelised conjugate gradient algorithm

Solving the linearised NES's is the predominant factor that makes SRM simulation time-consuming. In SPICE packages, direct e.g. triangular (LU)-factorization-based solvers are used normally. Although such a direct analytical method has high numerical stability [161], computing times increase exponentially with the size of the SRM. This quickly becomes a bottleneck for larger NES's. Although the sparse matrix techniques can be applied for optimisation [149-151, 158, 162, 163], complicated indexing mechanism and fill-in controls are required due to the high independency between rows, and therefore extra computational efforts will be introduced [164]. Iterative methods can be less computing intensive, and thus more time efficient, than direct ones. Being row-independent [165], they are suitable to combine sparse matrix techniques. An iterative method with suitably convergent behaviour can improve the performance of the solving process. As an example, Chen [152] proposed an efficient mixed numerical solver for circuit simulation, which can switch between the iterative generalized minimal residual (GMRES) method [166] and the conventional LU decomposition if GMRES diverges.

For the symmetric positive definite SpNES's of the SRM in PVONA, the conjugate gradient (CG) is introduced as the solving algorithm. This typically results in a linear dependence on matrix size [161, 167]. It can be expected that CG can provide a reliable estimation of the exact solution after a finite number of iterations, which is not larger than the size of the coefficient matrix, i.e. the number of nodes. The iterative steps of CG are shown in Algorithm 3.1. The use of the SpNES structure provides an efficient indexing system for matrix-vector multiplication (Figure 3.6-bottom), in which each MA element in ***Conductance*** can locate its multiplier in ***V*** directly by the index stored in the corresponding position in ***Neighbour***, without extra indexing operations. Expression (3.10) is used as the stopping criterion for CG

$$\|\boldsymbol{r}_k\|_2 < \varepsilon\|\boldsymbol{r}_0\|_2 \tag{3.10}$$

where $\varepsilon = 10^{-6}$; and $\boldsymbol{r}$ represents the residual vector in the Krylov subspace [165]. The *if-else* block from Line 6 to 9 introduces a regular round-off error removal process, in which the exact residual will be recalculated regularly, determined by the checkpoint N_C, to eliminate accumulated floating point error in the recursive formula [167].

Algorithm 3.1. Conjugate gradient (CG) [167][168]

1	$r^{(0)} \leftarrow b - \boldsymbol{A}x^{(0)}$
2	$p^{(0)} \leftarrow r^{(0)}$
3	for $k \leftarrow 0$ to k_{max}
4	$\alpha^{(k)} \leftarrow \langle r^{(k-1)}, r^{(k-1)}\rangle / \langle p^{(k-1)}, \boldsymbol{A}p^{(k-1)}\rangle$
5	$x^{(k)} \leftarrow x^{(k-1)} + \alpha^{(k)}p^{(k-1)}$
6	if k is divisible by 10,000
7	$r^{(k)} \leftarrow b - \boldsymbol{A}x^{(k-1)}$
8	else
9	$r^{(k)} \leftarrow r^{(k-1)} - \alpha^{(k)}\boldsymbol{A}p^{(k-1)}$
10	$\beta^{(k)} \leftarrow \langle r^{(k)}, r^{(k)}\rangle / \langle r^{(k-1)}, r^{(k-1)}\rangle$
11	$p^{(k)} \leftarrow r^{(k)} + \beta^{(k)}p^{(k-1)}$
12	if the exit criteria is not satisfied
13	$k \leftarrow k + 1$, continue the for loop
14	Else
15	break and return $x^{(k)}$

Some computing-intensive applications for high-resolution SRMs, e.g. the *I-V* calculation or the iterative local parameter fitting, require efficient approaches to keep the computing times under control. This is especially important in time-critical

situations e.g. the quality control in a production line. The row-wise independent operations in CG enables the implementation of parallel computing techniques for acceleration.

Parallel computing is an appropriate candidate for accelerating a program with intensive matrix computations. It enables allocating independent row-wise computations to the equipment which is able to run these smaller segments simultaneously and then to synchronize and re-assemble them [169]. This can be employed cost-effectively using a graphics processing unit (GPU) which can contain thousands of cores. The Compute Unified Device Architecture (CUDA) is a GPU computing architecture proposed by Nvidia, enabling transfer of sequential code to parallel, i.e. heterogeneous programming [170], as shown in Figure 3.9.

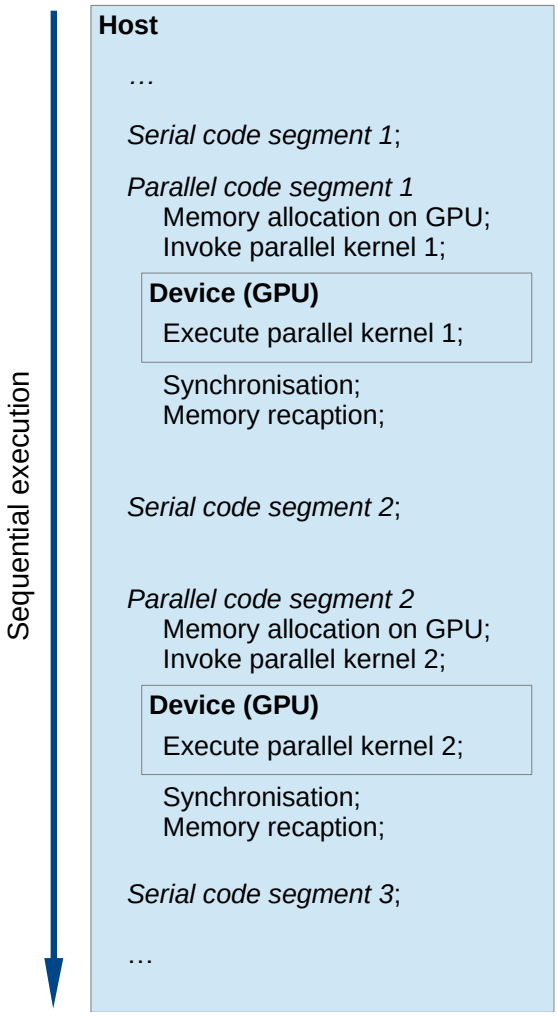

Figure 3.9. Diagram shows heterogeneous programming in CUDA [170]. Parallelism is performed by offloading computationally-intensive portions of the application to the GPU, while the remainder of the code still runs on the CPU.

The parallelism of CG is performed by offloading row-independent matrix arithmetic to a GPU, while the remainder still runs on the CPU. Each iterative sequence of CG involves a few inner products (Line 4 and 10), matrix-vector multiplications (Line 1, 4, 7 and 9) and scaled vector additions (Line 1, 5, 7, 9 and 11), as marked in Algorithm 1. These row-independent operations can be manipulated by functions *dotc*, *multiply* and *axpy*, respectively, using CUDA built-in libraries cuSPARSE [171] and cuBLAS [172]. In this study, an open source library CUSP is chosen as it provides a parallelised CG solver *cusp::cg* that utilizes those built-in functions with adaptive thread dispatching [173]. The parallel CG is integrated into the NR loop for solving the linearised SpNES's while the other operations remaining sequential.

3.5 Verification, performance evaluation and discussions

3.5.1 Verification with SPICE derivatives

To verify PVONA, a latest free circuit simulator LTSpice v4.22 [21] and a commercial PSpice v16.6 are used as the references. The LTSpice is operated on a PC with an Intel Core i5 CPU (3.20 GHz) and 4 GB memory is used as the basic test platform. For the CUDA-based parallel computing, a consumer-level Nvidia GeForce GTX760 graphic card equipped with 1.03 GHz clock rate, 2 GB device memory and 1152 computational cores is used. The PSpice is deployed on a comparable PC with an Intel Core i3 CPU (3.06 GHz) and 4 GB memory.

Identical SRM structures with randomly selected electrical parameters and external bias conditions were set up and solved by both PVONA and the two SPICE tools. The simulation of a thin-film PV cell is demonstrated here as an example. The size of the active area is 1 cm × 1 cm and the local electrical parameters are listed in Table 3.1. The standard test conditions i.e. irradiance 1000 W/m^2 and temperature 25 °C were used to set the environmental parameters. 5 test cases with 10,000 (100 × 100), 31,684 (178 × 178), 99,856 (316 × 316), 315,844 (562 × 562) and 1,000,000 (1000 × 1000) nodes, were chosen.

Table 3.1
Local electrical parameters for the thin-film PV cell

J_{ph}	1.35×10^{-2} A/cm^2
J_{sat}	1.0×10^{-10} A/cm^2
n	2.0
R_s	100.0 Ω·cm^2
R_{sh}	5.30×10^{5} Ω.cm^2
$R_{\blacksquare}$	8.0 Ω/□

Figure 3.10 overlays the *I-V* curves obtained from both PVONA and LTSpice simulated between 0-1.0 V with 100 intervals, using a 100 × 100 SRM. Visually they show perfect alignment. The maximum difference, approximately 1 mV, was found at the V_{OC} (0.963 V) area, giving only a 0.1% variation. This deviation is considered marginal in the context of the overall modelling accuracy and should be sufficient for all applications. The good agreement between *I-V* curves can be confirmed by calculating the root-mean-square deviation (RMSD) [174] values, using Equation (3.11)

$$\mathrm{RMSD} = \sqrt{\frac{\sum_{i=1}^{N}(I_{\mathrm{PVONA}} - I_{\mathrm{SPICE}})^2}{N}} \tag{3.11}$$

where N is number of *I-V* data pairs. The inset in Figure 3.10 demonstrates the RMSDs between the *I-V* curve pairs of different node numbers. It clearly shows that the RMSDs remain in a low range, with the order of magnitude of 10^{-5}. LTSpice crashed for the 562 × 562 and 1000 × 1000 cases due to the memory allocation failure. PSpice managed to operate simulations for the 562 × 562 case but failed in the 1000 × 1000 case. PVONA was able to handle these and produced results consistent with the lower resolution cases.

The good consistency implies that the accuracy and convergence are appropriately controlled in the three iterative loops (outer NR loop for solving the nonlinear network, inner NR loop for solving operating current in linearisation, and CG algorithm for solving linearised SpNES) in PVONA. Double precision floating point numbers were used, resulting in firstly the reduction of total round-off error, and secondly the lower possibility of numerical overflow. As to convergence, for CG, the symmetric positive definite $\boldsymbol{G}$ matrix guarantees the convergence [156]. However,

the speed of convergence can depend on the features e.g. the condition number [165] of the $\boldsymbol{G}$ matrix. For this reason, the application of pre-conditioned CG may provide further improvement to the solver. The performance of a NR solver may be affected by more complicated and subtle issues e.g. oscillations, ill-suited initial values and ill-conditioned NES's [154]. Nevertheless, PVONA has shown good stability for the simulations using typical parameters for PV devices and defects.

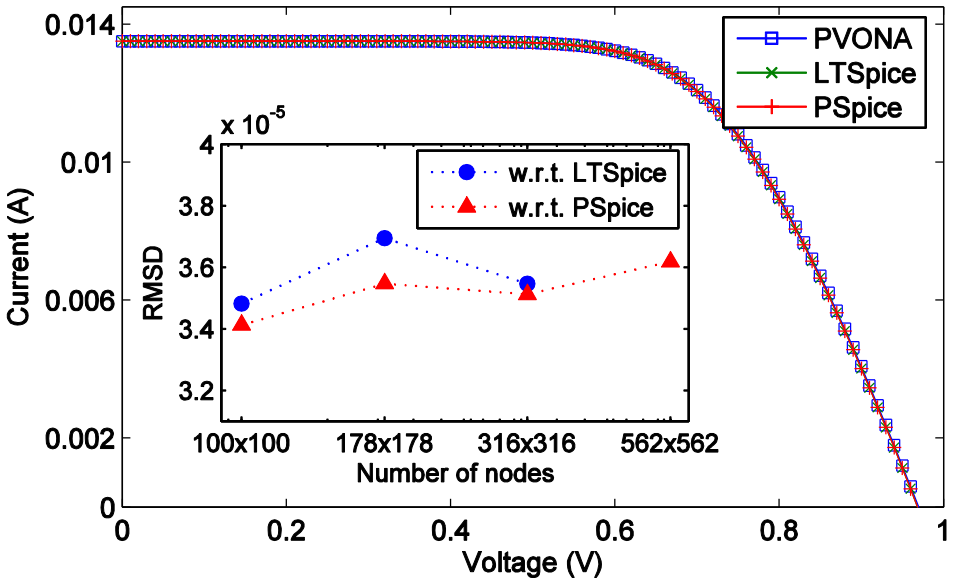

Figure 3.10. *I-V* curves of the 100 × 100 SRM generated by PVONA, LTSpice, and PSpice. Visually they show perfect alignment. (Inset) The RMSD values of the *I-V* data pairs for 100 × 100, 178 × 178, 318 × 318, and 562 × 562 models. The RMSD values remain in a low range, with the order of magnitude of 10^{-5}.

3.5.2 Performance evaluation

For each of the 5 listed test cases, the time for solving 6 voltage biases (0 V, 0.2 V, 0.4 V, 0.6 V 0.8 V and 1.0 V) were recorded and averaged. In terms of the computing speed, PVONA does not necessarily have advantages over LTSpice and PSpice when the size of the model is relatively small, especially lower than 50 × 50 nodes. For smaller sizes, the iterative CG algorithm may require more time than a direct method e.g. LU factorization to solve linearised NES's [175], and the time for parsing a short netlist in SPICE is negligible. However, it is evident that PVONA is significantly faster as the size of the problem increases, as illustrated in Figure 3.11. The sequential PVONA used 8.4% of the time required by LTSpice for the 316 × 316 model. The

improvement due to the parallelised CG is also noticeable, enabling another 54% faster than the sequential counterpart in this case, i.e. only 4.6% compared to LTSpice. The time for these simulations required by PSpice is within the same order of magnitude comparing LTSpice. For the 562 × 562 case, PVONA required only 4.1% of the time.

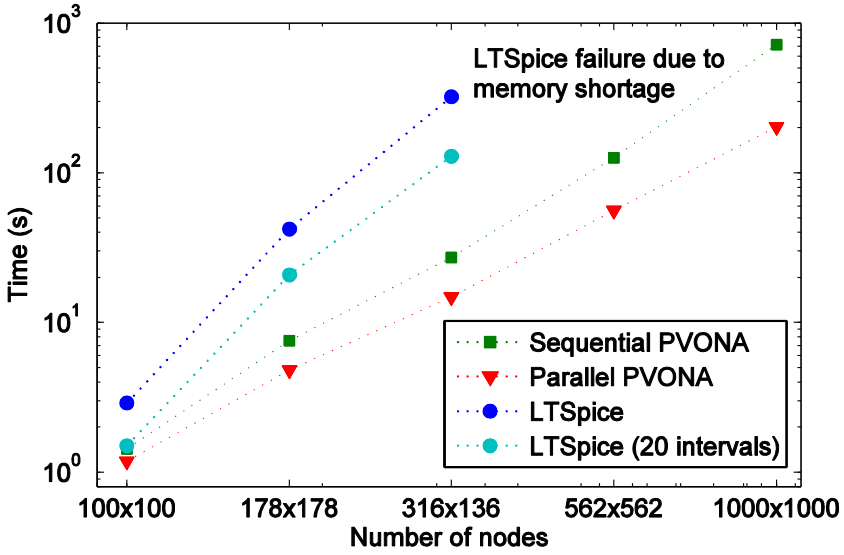

(a)

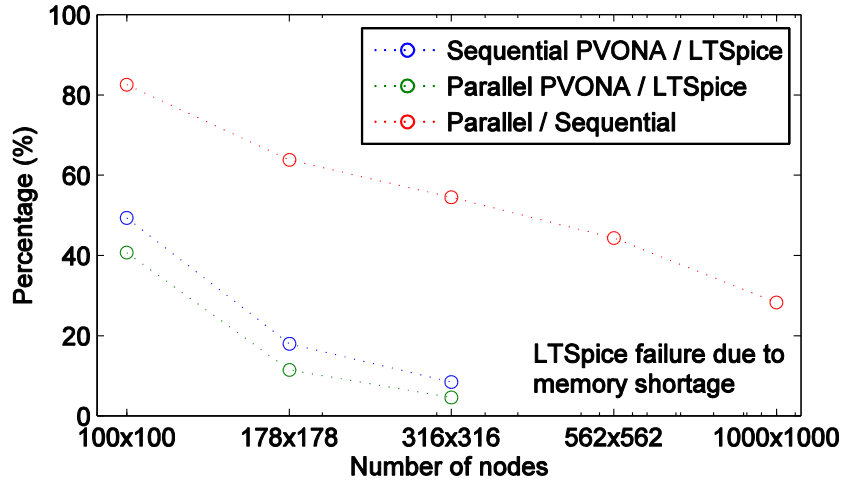

(b)

Figure 3.11. (a) Averaged time for solving one voltage-bias condition by PVONA and LTSpice for varying number of nodes. (b) The percentage of time consumption between PVONA and LTSpice for different number of nodes. The benefit of using PVONA is overwhelming.

It is noticeable that in SPICE tools, a large amount of time is consumed on the initialisation e.g. netlist parsing and system matrix generation stages. For this reason, a high number of bias conditions in a single run may balance the cost for the initialisation. For example, the average time needed from a 20-interval *I*-*V* simulation is shorter than that in the original 5-interval cases, as demonstrated in Figure 3.11a. However, it is still highly inefficient comparing PVONA, especially for the simulation of a single bias condition e.g. an EL image.

The implementation of the SpNES allows simulations for higher number of nodes possible. The sequential and parallel PVONA managed to solve the 1000 × 1000 model (equivalent to a mega-pixel image) within 12 minutes and 3.4 minutes, respectively. Although the time consumption of a task can vary significantly depending on the features of the NES and thus the parameter values, the benefit of using PVONA is clearly demonstrated. Further parallelisation may be implemented to PVONA with the support of GPU computing. For example, the linearisation processes can also be parallelised due to the fact that the linearisation for each local diode model can be carried out independently. However, extra efforts are needed to balance the overhead and latency effects for the data transfer between the main memory and the GPU memory [170]. For the same reason, using CUDA-supported data structure e.g. matrices and vectors in the SpNES may allow another level of improvement to PVONA.

3.6 User and programming interfaces

3.6.1 Software framework and user interface

The PVONA toolset elaborated above acts as a simulation engine for spatially-resolved models for PV cells. A graphical user interface (GUI) is developed to organise the whole simulation workflow, as shown in Figure 3.12. Briefly, the configurations for the cell model are done by loading external files. The program is able to produce local operating points and *I*-*V* curves. The data can be displayed directly for quick inspections or can be exported to external text files for further processing and analysis.

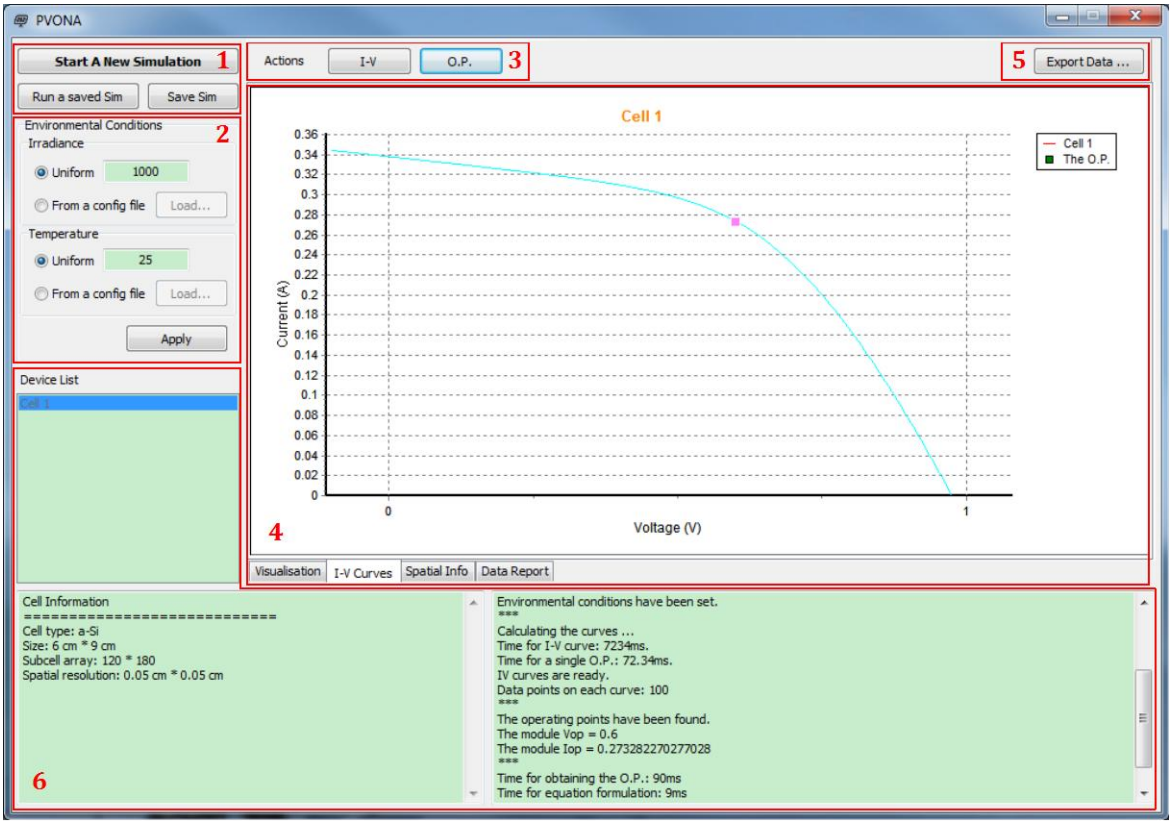

Figure 3.12. GUI of the simulation program based on PVONA. The GUI is composed by 6 functional modules, namely the (1) configuration files management, (2) environmental configuration, (3) simulation settings, (4) simulation monitors, (5) data export and (6) status monitors.

The GUI consists of 6 functional modules. The function of each module is described as follows:

(1) ***Configuration files management***

The configuration files for a cell model can be loaded from this module. For a new simulation task, the configuration file containing the basic information of the cell (e.g. the type of the diode model, the size of the sub-cell array, etc.) and all local electrical parameters should be read by the program. The users can save the active simulation task by clicking the "Save sim" button. All the parameters and changed simulation settings will be remained in a configuration file. The saved simulations can be loaded from the "Run a saved sim" function. The format of the configuration files will be illustrated in Section 3.6.2.

(2) ***Environmental configuration***

This module provides a speedy way to change environmental (i.e. irradiance and temperature) conditions to a prepared cell model. The new environmental conditions can overwrite the parameters configured with the diode models in module (1). The environmental conditions can be uniform or nonuniform. Uniform conditions can be read from the edit boxes. Nonuniform conditions are loaded from external text files in which the local irradiance or temperature values are recorded in a row-major $R \times C$ matrix, where R and C are the number of rows and columns of the sub-cell array, respectively. A case study in Section 4.3 will show how the irradiance interface is used in the analysis of the effects of nonuniform illumination.

(3) ***Simulation settings***

Two simulation modes, i.e. the *I-V* curves and the local operating points (O.P.), are available. In the O.P. mode, the type and the value of the external electrical bias should be set by the users. The bias can be either current, voltage or ohmic load. In the *I-V* mode, the number of data points for the *I-V* curve can be specified. Using the default settings will produce a curve in the first quadrant with voltage biases, although these settings can also be customised.

(4) ***Simulation monitors***

Simulation monitors inspect the simulation results. There are 4 pages, namely the Visualisation, *I-V* curves, Spatial info, and Data report. The *I-V* curves page displays the *I-V* curve generated in the *I-V* mode. The Visualisation page provides a quick glance of the current map and the voltage map graphically. The local operating points for each sub-cell are available through the Spatial info page. The Data report page is used to preview the text file generated for data export.

(5) ***Data export***

Simulation results, *I-V* data or local operation points, can be exported to external text or Matlab (.m) files for visualisation or further analysis. The data source to be exported depends on the active simulation monitor. If the "*I-V*

curves" page is active, the *I*-*V* data will be exported; if the "Spatial info" page is active, the local operation points will be exported.

(6) ***Status monitors***

3 message boxes enable the status of simulations observable. The device list displays the name of the cell, as loaded from the configuration file. The Cell information box (bottom-left) shows the basic information of the cell and the model e.g. the type, the actual size, the size of the sub-cell array, the spatial resolution, etc.. The Simulation status box (bottom-right) exhibits the real-time status of the simulation, as demonstrated in Figure 3.12.

3.6.2 Configuration files

The configuration files should ensure the minimum data set for a constructing a cell model to be passed to the PVONA program. The minimum data set includes the dimension i.e. the row and column numbers of the sub-cell array, and the parameters for all the electrical components i.e. the lateral resistances and the diode models. There are two configuration modes, namely the uniform configuration and the full configuration.

The uniform configuration can be used for thin-film cells with uniform distribution of local electrical parameters. The content of a uniform configuration file for a standard model with 100 × 100 sub-cells is shown in Figure 3.13a. A line starts with "#" denotes the comment line and will be ignored during data extraction. Line 6 specifies the size of the sub-cell array. Each resistor in the front contact layer is assigned by the value in Line 9. Line 12 provides the data set for all the local single-diode models. The SI (International System of Units) derived units are used unless specified.

All nonuniform cell models should be configured by the full mode. A full configuration file of a thin-film cell with a 3 × 3 SRM is shown in Figure 3.13b for demonstration. The size of the sub-cell array is listed in Line 6. The parameter set for each sub-cell occupies a single line, sorted by the row-major rule. All the electrical parameters for a sub-cell (Figure 3.3) should be enumerated explicitly.

```
##########################################
# Configuration File - unified parameters #
##########################################

# Size of the array (n_SubRows, n_SubCols)
100, 100

# Front contact (Rtop)
1e-4;

# Diode parameters (G, TinC, Iph, Isat, Rs, Rsh, n)
1000, 25, 1E-3, 1E-10, 0.1, 530E+3, 1.5

# end
```

(a)

```
#####################
# Full configuration #
#####################

# Size of the array (n_SubRows, n_SubCols)
3, 3

# The full (distributed) configuration
# Rtop_west, Rtop_south, Iph, Isat, Rs, Rsh, n, G, TinC
# Subcell(0, 0)
5.000000e-05, 1.000000e-04, 1.000000e-03, 1.000000e-10, 1.000000e-01, 5.300000e+05, 1.500000e+00, 1000.000000, 24.999994
# Subcell(0, 1)
1.000000e-04, 1.000000e-04, 1.000000e-03, 1.000000e-10, 1.000000e-01, 5.300000e+05, 1.500000e+00, 1000.000000, 24.999994
# Subcell(0, 2)
1.000000e-04, 1.000000e-04, 1.000000e-03, 1.000000e-10, 1.000000e-01, 5.300000e+05, 1.500000e+00, 1000.000000, 24.999994

# Rtop_west, Rtop_south, Iph, Isat, Rs, Rsh, n, G, TinC
# Subcell(1, 0)
5.000000e-05, 1.000000e-04, 1.000000e-03, 1.000000e-10, 1.000000e-01, 5.300000e+05, 1.500000e+00, 1000.000000, 24.999994
# Subcell(1, 1)
1.000000e-04, 1.000000e-04, 1.000000e-03, 1.000000e-10, 1.000000e-01, 5.300000e+05, 1.500000e+00, 1000.000000, 24.999994
# Subcell(1, 2)
1.000000e-04, 1.000000e-04, 1.000000e-03, 1.000000e-10, 1.000000e-01, 5.300000e+05, 1.500000e+00, 1000.000000, 24.999994

# Rtop_west, Rtop_south, Iph, Isat, Rs, Rsh, n, G, TinC
# Subcell(2, 0)
5.000000e-05, 1.000000e-04, 1.000000e-03, 1.000000e-10, 1.000000e-01, 5.300000e+05, 1.500000e+00, 1000.000000, 24.999994
# Subcell(2, 1)
1.000000e-04, 1.000000e-04, 1.000000e-03, 1.000000e-10, 1.000000e-01, 5.300000e+05, 1.500000e+00, 1000.000000, 24.999994
# Subcell(2, 2)
1.000000e-04, 1.000000e-04, 1.000000e-03, 1.000000e-10, 1.000000e-01, 5.300000e+05, 1.500000e+00, 1000.000000, 24.999994

# end
```

(b)

Figure 3.13. Examples of (a) a uniform configuration file and (b) a full configuration file. The uniform configuration can be used only for a-Si cells with uniform distribution of local electrical parameters. All the nonuniform cell models should be configured by the full mode.

A separate program[4] is developed to generate full configuration files. This is especially effective for c-Si cells as they have metal grids (Figure 2.5). Apart from electrical parameters, the program requires geometric data for the contact grid as inputs. Typical geometric parameters include the number of busbars and fingers, the widths and lengths of the busbars and fingers, as well as the distances between two fingers. These geometric measures are translated into the number of sub-cells according to the resolution of the SRM. The program firstly generates a uniform cell

[4] The program for configuration file generation is developed in C.

model with the electrical parameters, and secondly adjusts the lateral resistances to represent the metal grid in the front contact layer. The I_{ph} values of the local diode models under the busbars and fingers are set to nil due to the shading. To introduce defects, parameters can be changed directly in a configuration file, or by adding statements when creating a customised simulation scenario. An example of utilising this program to generate the configuration file of the SRM of the c-Si cell used in Section 4.3 is demonstrated in Appendix B.

3.6.3 Programming interfaces

PVONA provides integrated functions for parameter configuration, simulation and data export. Since object-oriented programming was used, all these functions should be based on a ***cell*** object in which all the parameters are organised. An incomplete list of the main member functions of the ***cell*** class is shown in Table 3.2 with brief descriptions. By utilising these programming interfaces, users can customise their own simulation tasks with more complicated workflows, making PVONA a versatile and generalised toolset for the modelling of PV devices. The function prototypes are listed in Appendix A.2 and an example is given in Appendix A.3 to demonstrate how these programming interfaces are used to calculate local operating points.

3.7 Chapter conclusions

A PV-oriented nodal analysis (PVONA) is presented in this chapter that enables significantly faster 2-D simulations of PV devices than two popular SPICE tools, LTSpice and PSpice. The use of the sparse CG algorithm and CUDA-based parallel computing techniques not only significantly saves the memory space but also accelerates the numerical solving procedure for high-resolution simulations. Further acceleration is possible by upgrading to a dedicated GPU and higher power CPUs. In the tests, the accelerated PVONA managed to accurately solve a 1000 × 1000 model, equivalent to the pixel number of a mega-pixel EL image, of a thin-film cell in only 3.4 minutes. The timing presented here depends obviously on the hardware involved. The equipment used was a reasonable PC with a high specification graphic card, but even this was not top of the range. The speed presented should, with some further adaptations, allow the application in commercial environments.

The following chapter will show the applicability of the PVONA-based 2-D SRMs by case studies. More specifically, Chapter 4 provides how SRMs can be used to investigate the impacts of internal and external inhomogeneities on the performance of PV cells. It will also illustrate the integration of the PVONA tool into a hierarchical architecture for modelling PV modules. In addition, an initial step towards quantifying EL measurements will be demonstrated, which will be further extended to a systematic and automated characterisation algorithm in Chapter 5.

Table 3.2
Incomplete list of member functions of a ***cell*** class.

* (p) denotes a pointer

Function	Arguments	Brief description
Configuration		
Config_Uni	***Cell*** (p)*	Model setup by a uniform configuration file. The default filename "UniConFiguretxt" is used.
Config_Full	***Cell*** (p)	Model setup by a full configuration file. The default filename "FullConFiguretxt" is used.
SaveConfig2File	***Cell*** (p), *filename*	Export the parameters and settings of the current simulation to a text file "*filename*.txt", using the format of a full configuration file.
Simulation		
GetOPbyI	***Cell*** (p), I_{bias}	Calculate the local operating points with a given current bias I_{bias}.
GetOPbyV	***Cell*** (p), V_{bias}	Calculate the local operating points with a given voltage bias V_{bias}.
GetOPbyR	***Cell*** (p), R_{bias}	Calculate the local operating points with a given ohmic load R_{bias}.
GetIV	***Cell*** (p), *nData*	Calculate the *I-V* curve of the cell under the configured environmental conditions. The number of the data points is set by *nData*.
Data export		
SaveOP2File	***Cell*** (p), *filename*	Export the local operating points to a text file "*filename*.txt".
SaveIV2File	***Cell*** (p), *filename*	Export the *I-V* data to a text file "*filename*.txt".

Chapter 4

Investigation of effects of inhomogeneities in PV devices using PVONA

4.1 Overview

The previous chapter introduced the PVONA toolset developed in this thesis. It enables fast and accurate 2-D simulations of high-resolution spatially-resolved models (SRMs) of PV cells. A PV cell normally extends over a large area (of a semiconductor device) and may therefore be affected by inhomogeneities. These can be due to the nonuniformity of internal properties such as material quality or of external factors such as environmental conditions, or a mix of both. This chapter will use these tools to investigate the effect of inhomogeneities on device performance.

Describing localised properties is the major advantage of an SRM over a lumped model and this can be used as a complementary tool to the global *I*-*V* analysis. For example, Mack *et al*. [176] and Ott *et al*. [64] reported work that utilised SRMs to investigate the effects of local shunts in thin-film CIGS modules. Vorasayan *et al*. [62] introduced an SRM to study the electrical mismatch effects in LBIC measurements and to evaluate the improved limited-LBIC approach. Gupta *et al*. [13] analysed LIT measurement results supported by an SRM. Guo *et al*. [17] showed the impacts of e.g. broken fingers on the performance of wafer-based cells. Pieters introduced a variable meshing strategy [12] for better representations of local inhomogeneities and extended this in [148] to simulate complicated geometries of the contact grids in c-Si PV cells. Thus there is a plethora of applications for such a method, but, as discussed in the previous chapter, the resolution of any simulation is limited by the exponential increase in computation time of conventional circuit simulation tools. This chapter will demonstrate the advantages of PVONA in terms of resolution and minimum size of faults.

In this chapter, the application of the SRMs is further developed for various purposes. Firstly, Section 4.2 will illustrate that the PVONA-based cell-level SRMs can be further integrated into a hierarchical architecture as an extension of the Bishop's [177] approach for modelling PV modules. The approach introduced in the case study given in Section 4.3 allows the estimation of the effects of inhomogeneous irradiance caused e.g. by imperfect optics in concentrated PV (CPV) by combining an optical model [178]. This provides not only global *I*-*V* characteristics but also detailed maps of performance distribution and operating conditions.

PVONA requires a reliable parameterisation process to build SRMs. Conventional fitting methods can produce parameters that reconstruct global *I-V* characteristics based on the lumped model. To fit the SRMs, the geometries of the meshing grid need to be considered [71]. Section 4.4 details how the localised parameters with respect to the meshing size need to be configured to achieve accurate results. PVONA simulations are used to study the localised effects of lateral resistances in c-Si and thin-film devices. This allows the description of local defects e.g. a disconnected finger and local shunts detected in EL images, which were normally assessed qualitatively. Results presented in a case study in Section 4.5 provide accurate reconstruction of features in EL measurements using image-sized SRMs, shown the potential of PVONA towards quantifying full resolution EL images.

4.2 Modelling PV modules using PVONA

4.2.1 Hierarchical architecture

The development of PVONA-based SRM enables the simulation of single PV cells in a spatially-resolved point of view. Individual PV cells can only produce a limited amount of power. In real applications, PV cells are electrically connected together into a network following a specific topological structure so that the overall power output can meet the required specification. For example, a commercial c-Si module typically consists of 36 to 72 interconnected solar cells. Multiple modules can be then wired together to form a PV array for a more complex PV system. The SRM-based modelling and simulation of PV cells can be extended to a level that contains complicated electrical topologies, i.e. modules or arrays.

Conventionally, the behaviour of a PV module is described by simply combining the *I-V* characteristics of lumped diode models. Such a relation based on single-diode models can be written as

$$I = N_p \left\{ -I_{ph} + I_{sat} \left[\exp\left(\frac{q\left(\frac{V}{N_s} - \frac{I}{N_p} R_s\right)}{nkT} \right) - 1 \right] + \frac{\frac{V}{N_s} - \frac{I}{N_p} R_s}{R_p} \right\} \tag{4.1}$$

where N_s and N_p denote the number of the series cells and parallel cells, respectively [179]. This is based on the assumption that there is no electrical mismatch among all the components, i.e. all the cells in the module have an identical *I-V* characteristic. This relation can be extended to PV arrays if the ideal conditions can apply, which in reality does not happen since cells and modules are manufactured with tolerances.

A simulation approach based on a hierarchical model architecture without the assumption of ideal conditions was introduced to construct the complicated electrical topology in PV modules or arrays by Bishop [177]. Cells are the most elementary components in a PV module. A complicated structure of a PV module is considered to be composed by three types of interconnected circuits, namely the simple series strings, series-parallel blocks and a series connection of series-parallel blocks. Bishop proposed a six-level hierarchical architecture that divides a PV array into branches (each of which can be protected by a blocking diode), then blocks (each of which can be bridged by bypass-diodes). A block can then be further split into series sub-blocks which consist of parallel strings.

However, in the original hierarchical architecture, the cells were based on the lumped model, which has been indicated in this work to be insufficient to fully describe the characteristics of a PV cell if e.g. production flaws are to be investigated. To enable the devices described in a spatially-resolved manner, the SRM is implemented. This is achieved by extending the six-level hierarchical architecture with a seventh level, the subcell level, where the PVONA-based SRMs are applied. By specifying the number of proximate lower-level units in each level (*nBranch*, *nBlock*, *nSubBlk*, *nString* and *nCell*, respectively), an electrical topology of the array can be precisely described. This is demonstrated in Figure 4.1 with an example. The extension enables spatially-resolved description of complex PV device network and can be used in modelling of the whole PV system connected to the converter.

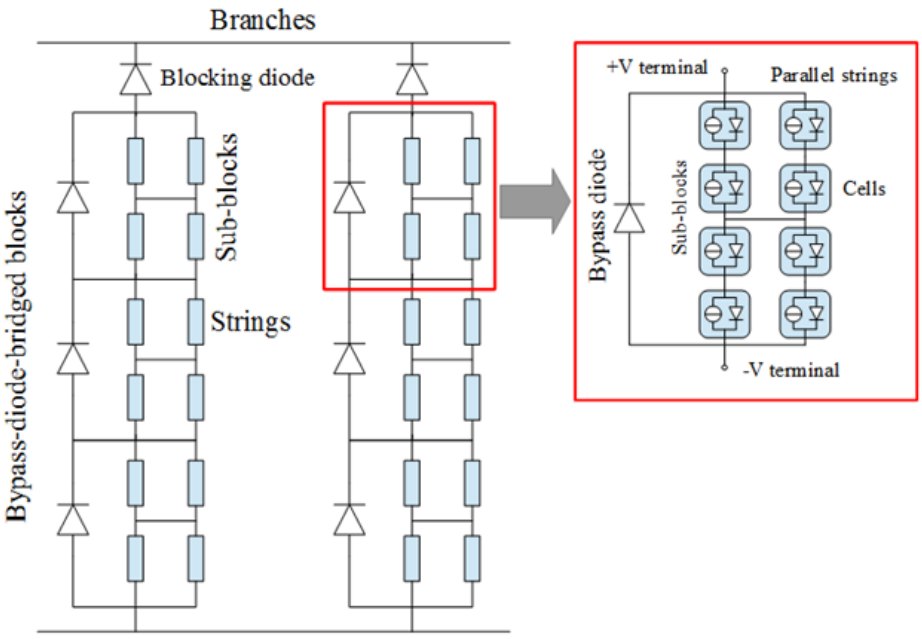

Figure 4.1. Demonstration of a complex electrical topology in a PV array using the hierarchical architecture. PV cells are electrically connected together for higher overall power. In this example, *nBranch* = 2, *nBlock* = 3, *nSubBlk* = 2, *nString* = 2 and *nCell* = 2. In this work, the cells are replaced by the SRMs to which the PVONA toolset can be applied.

4.2.2 Combining *I-V* curves and tracing operating points

In the hierarchical model, the electrical behaviour of all the components above the cell level is described only by their *I-V* characteristics. This is the result of combining the *I-V* curves of each circuit element following a bottom-up manner from the cell level upwards. Unlike the original model in which the *I-V* characteristic of a cell is obtained by solving a lumped model, the PVONA-based cell model generates the *I-V* curve by performing the programming interface *getIV* (see Table 3.2) to the SRM of the cell.

The manipulation of *I-V* curves follows the Kirchhoff's circuit laws [180]. To combine the *I-V* curves, the first step is to define the reference data series and its range. The reference data series, i.e. the fixed current or fixed voltage, is determined by the pattern of connection. For the components connected in series, e.g. individual cells in a series string, the higher level *I-V* curve is obtained by the summation of voltages at fixed current steps; and for the components connected in parallel, e.g. series strings in a series-parallel block, the higher level *I-V* curve is obtained by the summation of

currents at fixed voltage steps. After the *I-V* curves of all the levels are obtained, the operating point of each component can be determined by a top-down tracing process, according to the Kirchhoff's laws. Once the tracing process reaches the cell level, the PVONA tool calculates the local operating points by invoking the programming interface *GetOPbyI* or *GetOPbyV* (see Table 3.2).

The calculations for combining the *I-V* curves and tracing the operating point rely on an interpolation algorithm. Here, the recursive Newton polynomial $P(x)$ for interpolation is utilised, which is formulated as

$$P_N(x) = P_{N-1}(x) + a_N(x - x_0)(x - x_1) \dots (x - x_{N-1}) \tag{4.2}$$

where N is the order of the polynomial; x_0 … $x_{N\text{-}1}$ are the known independent variables. a_k denotes the divided differences [159]

$$a_k = [y_0, y_1 \dots y_k] \tag{4.3}$$

where y_0 … y_k are the known dependent variables pairing x_0 … x_k, respectively. The cubic polynomial (N = 3) is used in this work as it can appropriately reconstruct the *I-V* data pairs in practice.

Figure 4.2 demonstrates an example of *I-V* combining and operating point tracing. Two individual cells, Cell1 and Cell2, are connected to form a series string (*series*) and a parallel block (*parallel*) respectively. The electrical parameters used in the example are listed in Table 4.1. The curves Cell1 and Cell2 are obtained by PVONA. To calculate the Series curve, Cell1 and Cell2 are reshaped with respect to a reference current data series by the interpolation algorithm described above, and then the two calculated voltage data series are summed up. Similarly, the *parallel* curve is obtained by summing up the two reshaped current data series with respect to a reference voltage data series.

For a given operating point of the series string (S), the operating points of the two cells (S1 and S2) can be traced by the current I_S, as the cells connected in series have the identical operating current. The operating voltages corresponding to S1 and S2 can be obtained by solving the SRM with PVONA at a specific current load, i.e. using the function *GetOPbyI*. Similarly, P1 and P2 are obtained by setting the global operating voltage V_P of the parallel block as the voltage load in the SRM of the cells,

using the function *GetOPbyV*. Figure 4.3 demonstrate the normalised voltage and current maps of the two cells at S1, S2, P1 and P2, respectively, showing the effects of the mismatch on the local operating points. This can provide valuable information for e.g. the investigation the localised impacts of inhomogeneities on a PV module, which is a significant benefit of from the PVONA-extended hierarchical architecture.

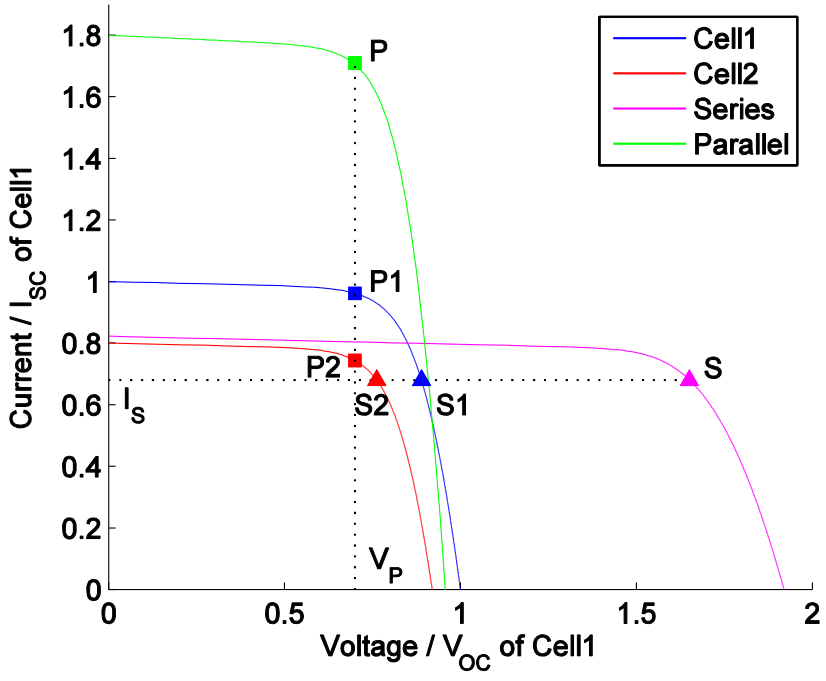

Figure 4.2. Example shows the *I-V* combining and operating point tracing in the hierarchical model architecture. Cell1 and Cell2 are connected to form a series string and a parallel block respectively. Both *I-V* combining and operating point tracing follow the Kirchhoff's circuit laws.

Table 4.1
Electrical parameters for the SRM of the virtual PV cell

	Cell1	Cell2
J_{sat}	5.0×10^{-7} A/cm^2	4.0×10^{-7} A/cm^2
n	1.4	1.3
Γ_{sh}	8.35×10^{4} Ω·cm^2	8.35×10^{4} Ω·cm^2
Γ_s^i	0.05 Ω·cm^2	0.05 Ω·cm^2
$R_{\blacksquare\text{emitter}}$	80.0 Ω/□	60.0 Ω/□
$R_{\blacksquare\text{grid}}$	1.0×10^{-3} Ω/□	1.0×10^{-3} Ω/□

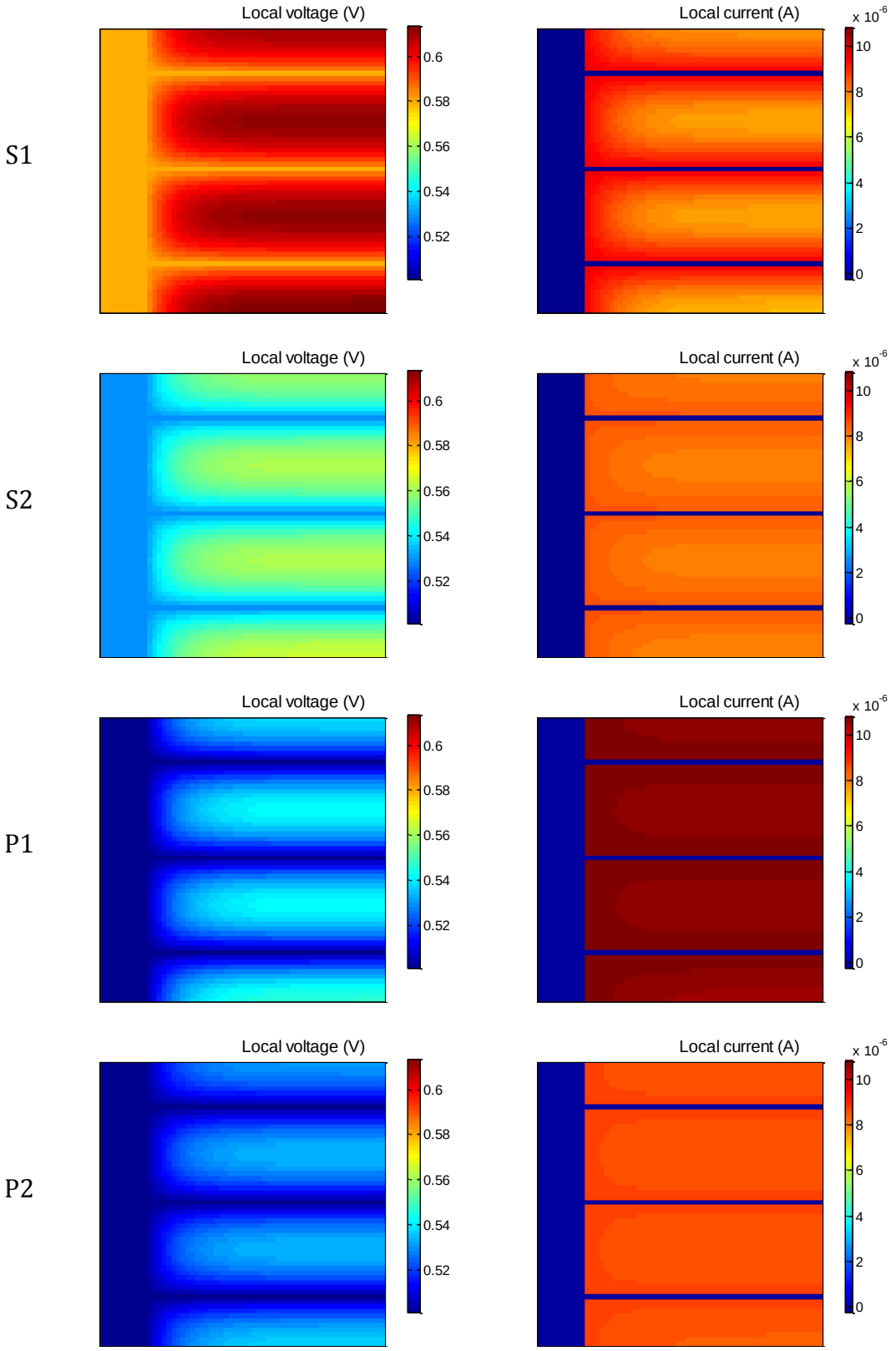

Figure 4.3. Normalised current and voltage maps of Cell1 and Cell2 operating at S1, S2, P1 and P2, as in the example demonstrated in Figure 4.2. The maps are obtained by calling the function *GetOPbyI* for S1 and S2, and *GetOPbyV* for P1 and P2, respectively. It shows the benefit of the PVONA-extended hierarchical architecture.

4.2.3 Model of bypass diodes in PV modules

A PV module is an assembly of single cells and is therefore easily subjected to mismatch effects due to individual variations among the cells or due to nonuniform environmental conditions. As shown in Figure 4.2, both series and parallel cell strings can suffer from mismatch effects. Comparatively, the series mismatch effects can cause worse impacts on the module performance than parallel mismatches.

It is common that in PV modules cells are connected in a series string and the overall output of the string is limited by the cell with poorest performance. The mismatch effects can be studied from *I*-*V* characteristics. Any difference between two *I*-*V* curves may lead to some mismatch losses. However, serious mismatch problems are most commonly caused by the differences in either the V_{OC} or, more significantly, the I_{SC} in the case of series interconnections. Especially in the low voltage range, the limited I_{SC} of the module can bring the poorest cell into reverse-bias, dissipating power. The exceeded photocurrent generated in the good cells is forced to be dissipated across their own junctions. This can result in not only the reduction of overall power generation, but also irreversible damages to the module due to serious hot-spot heating in the device.

The power loss in series mismatches can be circumvented by using bypass diodes [25, 177]. A bypass diode can be connected in parallel to a single cell or a string of cells, but with opposite polarity. For the case of a single cell for example, the *I*-*V* curve of a bypass-diode-protected cell is demonstrated in Figure 4.4a. The bypass diode is reverse-biased under normal operating conditions and does not influence the performance of the bypassed unit. When the protected unit encounters a series mismatch, the reversed voltage across the cell activates the diode, allowing the surplus current from the good cells to flow through the bypass circuit rather than to be dissipated within the junctions.

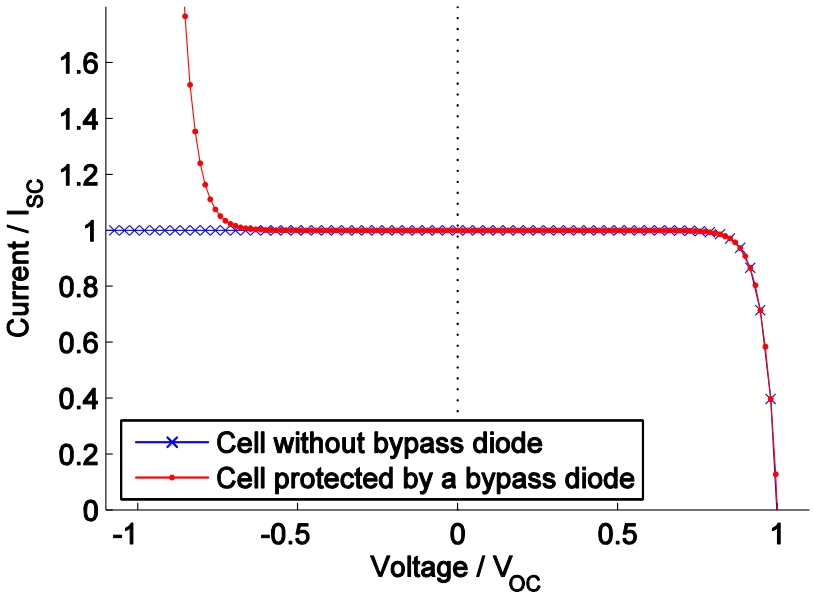

(a)

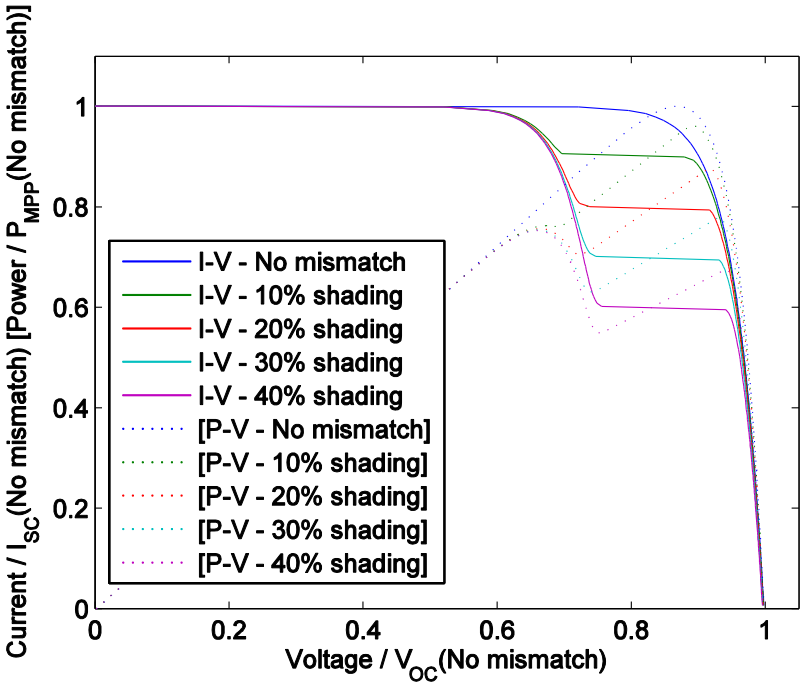

(b)

Figure 4.4. (a) Normalised *I-V* curve of a bypass-diode-protected cell; (b) Normalised *I-V* and *P-V* curves of a mismatched module composed by 4 good cells and 1 partially shaded cell. The overall characteristics of the module are reshaped and the output power losses due to the mismatches are reduced by utilising bypass diodes.

It is notable that there is still a reverse bias across the poor cell, but the strength is limited to the voltage drop over the diode, i.e. 0.6 V to 0.8 V. Figure 4.4b demonstrates the normalised *I*-*V* and *P*-*V* curves of a module consisting of 5 cells in series in which one is partially shaded. The overall characteristics are reshaped by the active bypass diode and the output power losses due to the mismatch module are reduced. The simulation of bypass diodes allows the investigation of PV modules operating in realistic conditions. Further detailed studies of mismatch losses can be found in [181-185].

4.3 Case study: Effects of non-uniform irradiation in CPV

4.3.1 Introduction and simulation setup

In this case study, PVONA-based simulations are utilised to research the influence of non-uniform irradiance on the performance of concentrator PV (CPV) systems. A CPV unit employs an optical concentrator to achieve high illumination and thus high efficiency conversion of sunlight to electrical power, as illustrated in Figure 4.5. It utilises either lenses or curved mirrors to focus sunlight onto small, but highly efficient, commonly multi-junction (MJ) PV cells. The project reported in [178] provided a detailed study on the modelling of CPV systems, including the properties of the optical components by means of ray tracing techniques. It suggested that the performance of the optical components e.g. lenses can suffer from uncertainties during the manufacturing processes or during installation, which may significantly affect the final energy output. However, there has not been an effective means for evaluating the influences of these sources of uncertainties on the electrical energy output in a CPV system.

The performance of a CPV unit can be affected by the behaviour of both the optical sub-system (lens) and the cell itself. A simulation tool is therefore useful as an analysis tool to aid the manufacturing and the assembly of the components to make sure the design objectives are met. This is achieved here by establishing a joint spatially-resolved modelling framework consisting of an optical model and the PVONA-based electrical SRM. The optical model [178] produces ray-traced irradiance profiles as the environmental input of the SRM, which is then solved by the PVONA

tools for global and localised operating points. This framework therefore provides a new means to evaluate the performance of CPV systems.

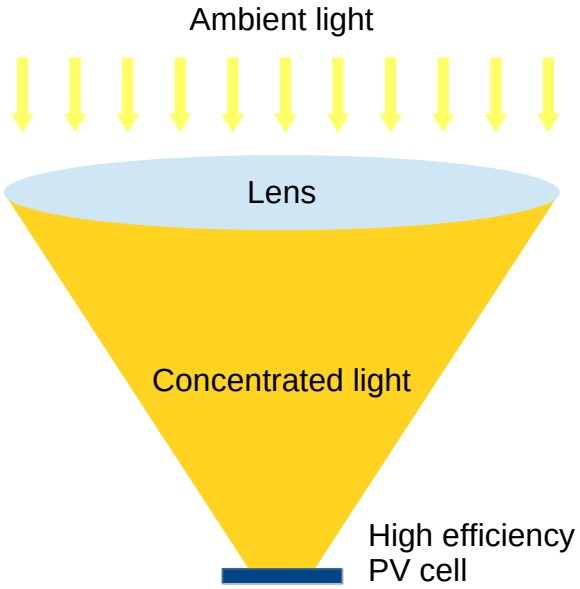

Figure 4.5. Schematic shows the components of a CPV unit. Ambient light is concentrated by a lens. The concentrated light is absorbed by e.g. a multi-junction PV cell to achieve high efficiency energy conversion. Either manufacturing tolerance or assembly error can cause distortion of the concentrated light spot.

Here, the modelling framework is employed to study the effects of uncertainty-affected irradiance profiles on the electrical output of a CPV unit. This approach can provide valuable information to e.g. the prediction of energy yield of a CPV system, which was normally done with lumped modelling techniques. Two types of lenses, i.e. plano-convex lens and Fresnel lenses, are considered in this case study. Two types of uncertainties, namely the manufacturing errors (e.g. due to the tolerance during lens manufacturing) of the plano-convex lenses and the mounting errors (e.g. due to the deformation of the frame) of the Fresnel lenses, are modelled using the ray-tracing tool described in [178].

The simulated 99 × 99 ray-traced irradiance profiles are shown in Figure 4.7 and Figure 4.9, respectively. Both the ideal and uncertainty-affected profiles are provided for comparison. A 99 × 99 SRM of a virtual 1 cm × 1 cm c-Si cell is configured with the electrical parameters listed in Table 4.2 and used as the target sample. The SRM configured here is a single-junction device for demonstration. Although MJ devices

are commonly used in actual CPV systems, this simplification is still valid for revealing the performance influences of inhomogeneities. The layout of the front contact grid of the cell is sketched in Figure 4.6 and the *I-V* curve (STC) of the cell is also displayed. The blue parts represent the active cell areas (the emitter layer), while the metal busbar and fingers are represented by grey strips. In the SRM, which the busbar occupies 2 columns, and each finger occupies a row. The global *I-V* curves as well as the voltage and current maps at MPPs are simulated for analysis.

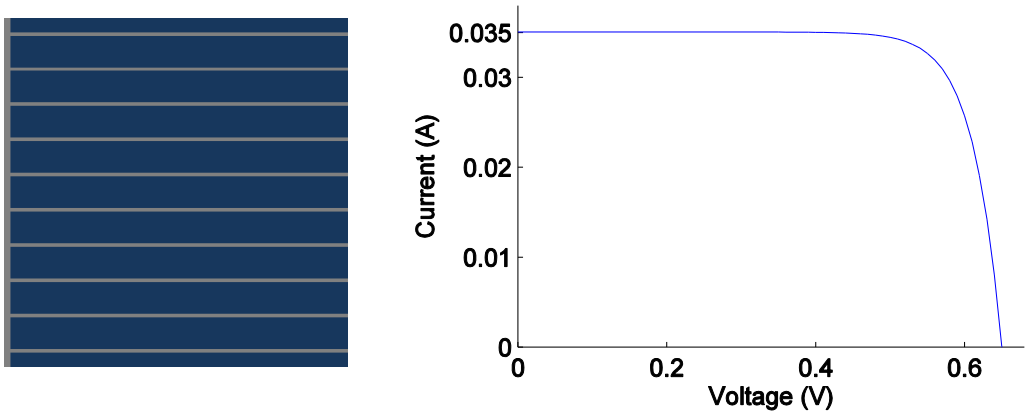

(a) (b)

Figure 4.6. (a) Schematic shows the layout of the 99 × 99 SRM of a virtual c-Si cell. The blue parts represent the active cell areas i.e. the emitter layer, while the metal busbar and fingers are represented by grey strips; (b) The *I-V* curve (STC) of the cell.

Table 4.2
Electrical parameters for the SRM of the virtual PV cell

J_{sat}	5.0×10^{-7} A/cm^2
n	1.4
Γ_{sh}	8.35×10^{4} Ω·cm^2
Γ_s^i	0.05 Ω·cm^2
$R_{\blacksquare\text{grid}}$	1.0×10^{-3} Ω/□
$R_{\blacksquare\text{emitter}}$	80.0 Ω/□

4.3.2 Simulation results

In the optical modelling, a total amount of incident power P_{in} = 2.10 W is applied. This is equivalent to, in average, a 2.10×10^{4} W/m^2 irradiance level. For the case of the

plano-convex lenses, the illumination profiles demonstrate a centralised high irradiance spot, with the irradiance up to approximately 3.5×10^5 W/m^2 i.e. 350 Suns (1 Sun = 1000 W/m^2). The impacts of the concentric-circle-shaped illumination profiles are clearly shown in the voltage and current maps in Figure 4.8. The variations between the ideal and the production tolerance afflicted profiles were due to a 0.15mm (1.5%) difference in the central thickness, while the manufacturing tolerance is normally 0.2mm. The lateral variations of the local voltage and local current are distinct. The global *I-V* characteristics are plotted in Figure 4.11a. For comparison, a uniform irradiance profile with 2.10×10^4 W/m^2 is configured and the corresponding *I-V* curve is overlaid. The results show that the effects of nonuniform irradiance are substantial. The ideal case and the uncertainty affected case have a 13% and 18% difference in the P_{MPP} comparing the uniform case, respectively. And a 5% difference in the P_{MPP} between the ideal and the uncertainty affected case means the overall conversion efficiency of the CPV unit has the same relative variation, since the P_{in} remains unchanged.

For the case of the Fresnel lenses, the variations of the illumination profiles are from a miss-aligned lens on the frame during installation. The misalignment is a compounded result from a deformed housing unit, with angled, twisted and elongated frames as well as normal production tolerances in optical components. The ray-traced uncertainty affected illumination profile demonstrates, comparing with the ideal profile, (i) an approximately 10% linear shift in the position of the central point; (ii) a 20% increase in ring size; and (iii) a 15% reduction in the maximum intensity. The two profiles are displayed in Figure 4.9. There is also a 'flowering' effect that results from the aberrations of the lens, specifically the difference in refraction at the lens centre and the lens edges [178]. The localised variations are shown by the voltage and current maps in Figure 4.10, and the global *I-V* characteristics in Figure 4.12a reveal a 3% difference in the P_{MPP} between the ideal and the uncertainty affected case, but the latter gives a higher P_{MPP}. The variations with respect to the uniform case are also distinct.

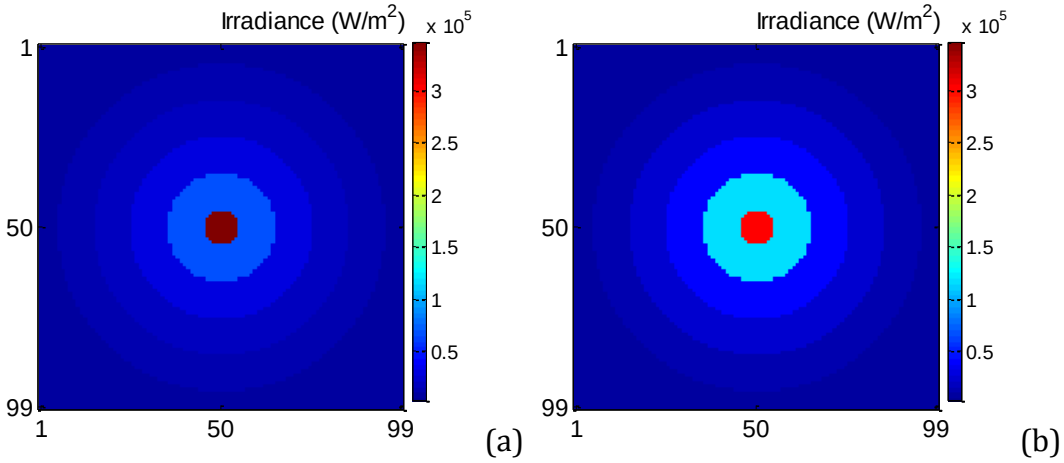

Figure 4.7. Simulated 99 × 99 (a) ideal and (b) production tolerance affected irradiance profiles of a plano-convex lens, using the ray-tracing tool described in [178]. The variations come from a 1.5% difference in the central thickness.

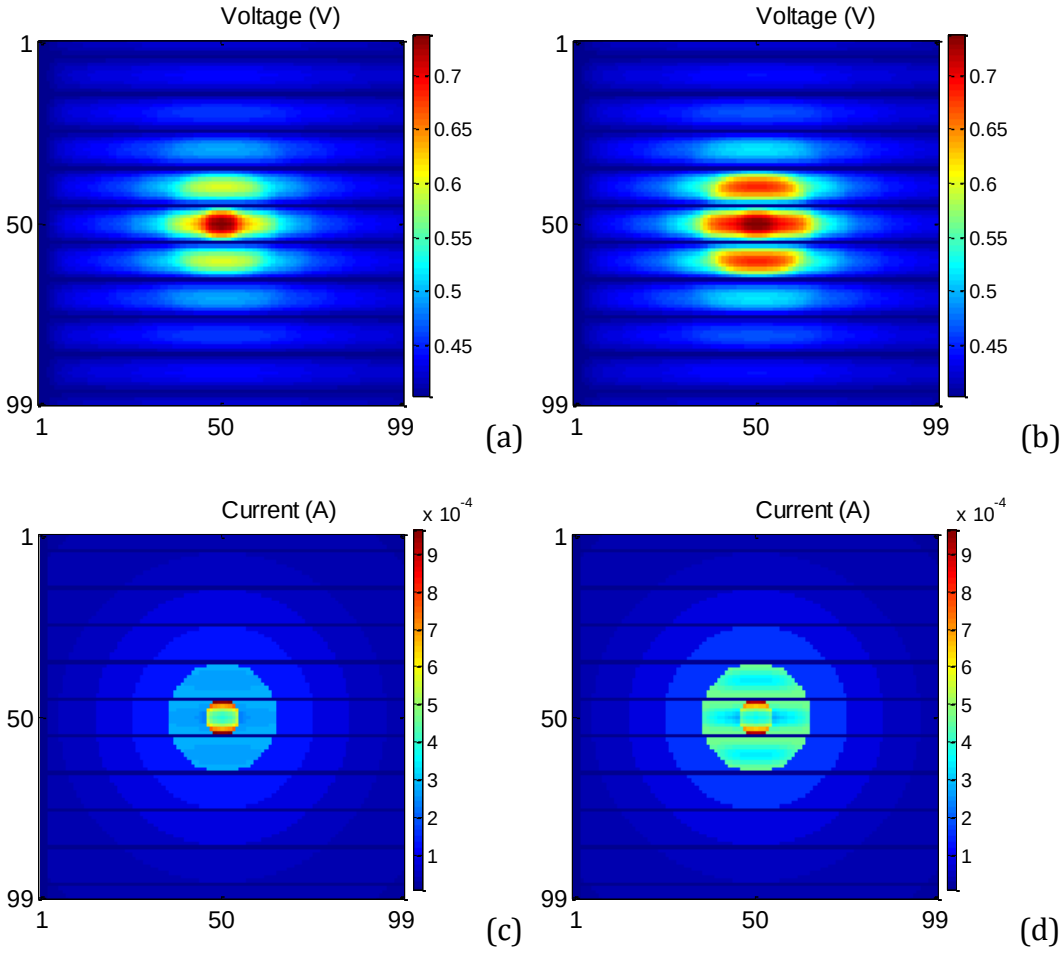

Figure 4.8. Simulated voltage and current maps of the ideal and the production tolerance affected CPV units, operating at the MPPs. (a) and (c) corresponds to the ideal case; (b) and (d) are for the production tolerance affected case.

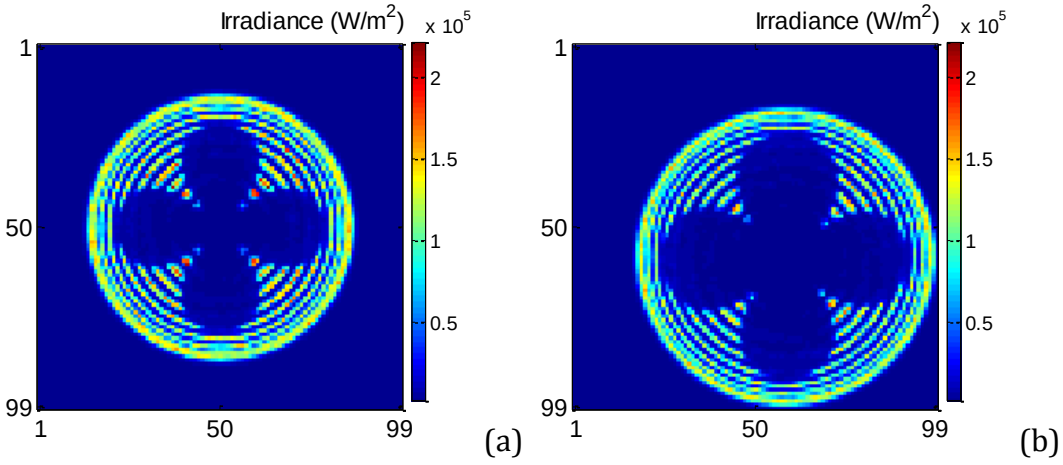

Figure 4.9. Simulated 99 × 99 (a) ideal and (b) uncertainty affected illumination profiles of a Fresnel lens, using the ray-tracing tool described in [178]. The variations mainly came from the installation errors.

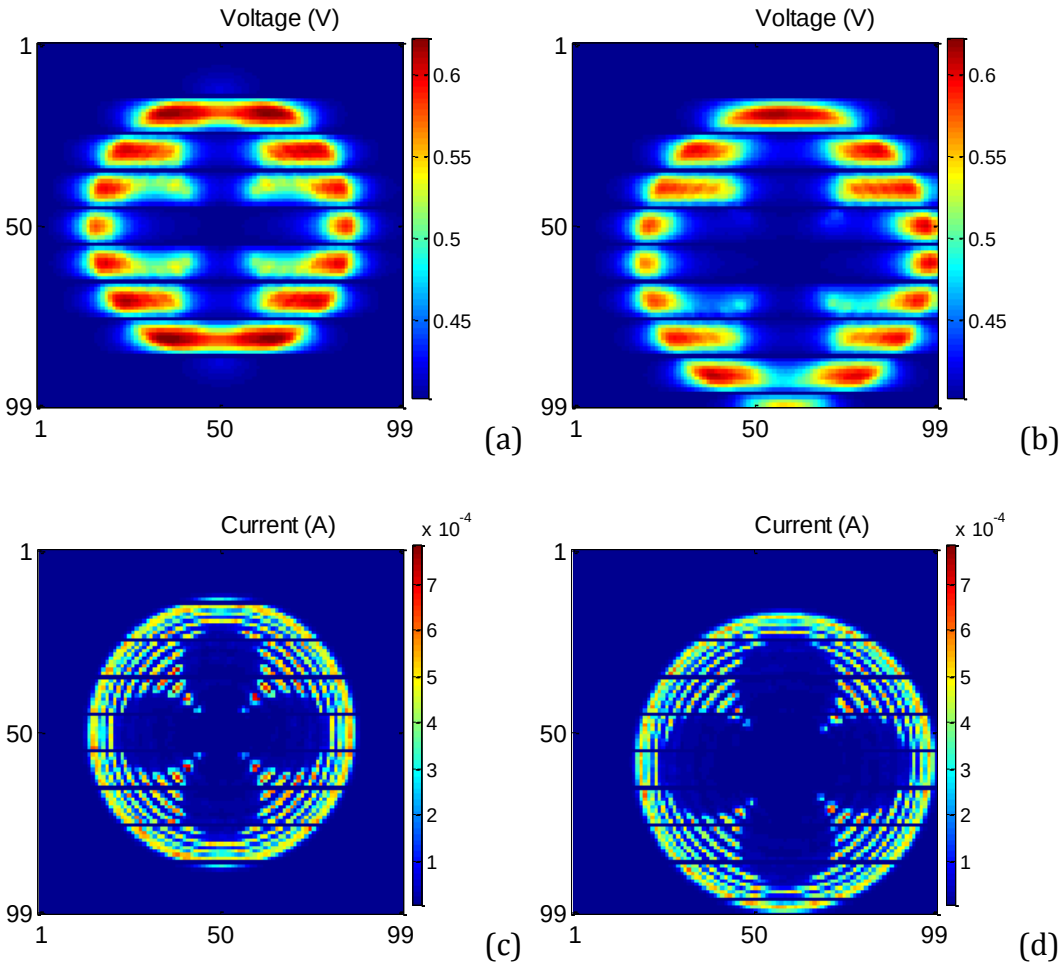

Figure 4.10. Simulated voltage and current maps of the ideal and the uncertainty affected CPV units, operating at the MPPs. (a) and (c) corresponds to the ideal case; (b) and (d) are for the uncertainty affected case.

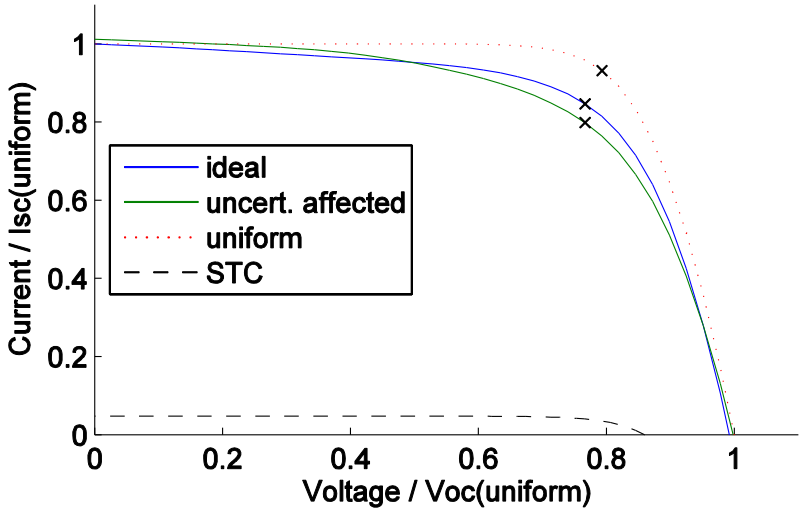

(a)

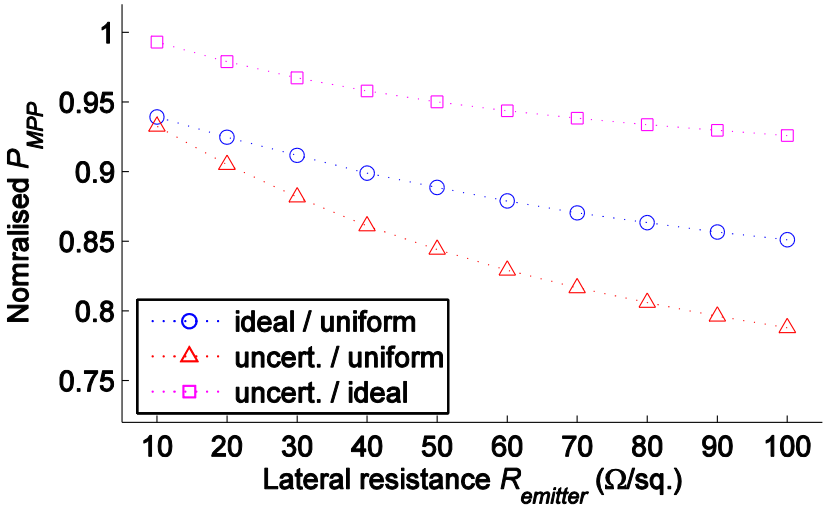

(b)

Figure 4.11. Simulation results of the plano-convex lens case. (a) Simulated *I-V* curves of the virtual c-Si cell operating under the ideal and the lower quality optics affected illumination conditions. The reference *I-V* is obtained by applying the same amount of incident power to the sample, homogeneously distributed. (b) A sensitivity analysis with respect to the lateral series resistance of the emitter layer $R_{\blacksquare\,\mathrm{emitter}}$.

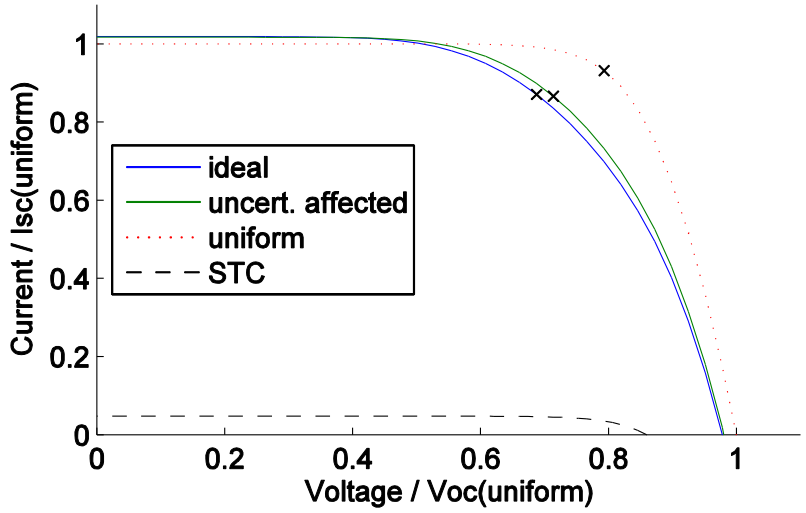

(a)

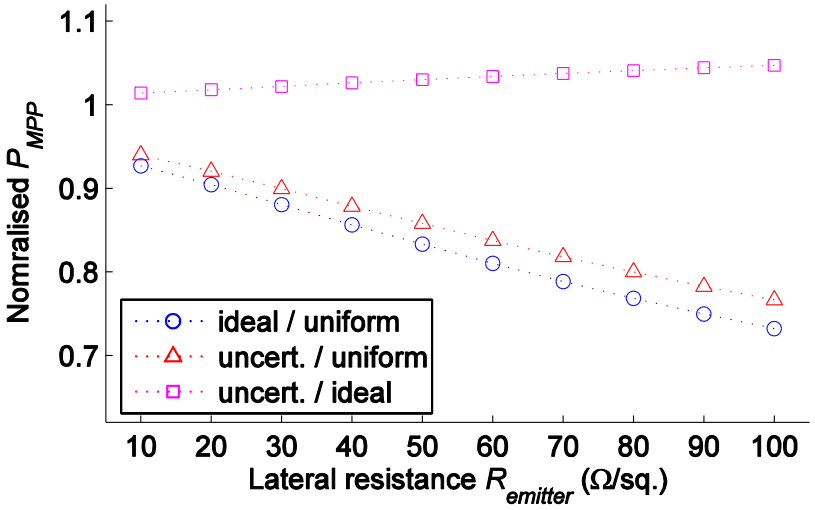

(b)

Figure 4.12. Simulation results of the Fresnel lens case. (a) Simulated *I-V* curves of the virtual c-Si cell operating under the ideal and the production tolerance affected illumination conditions. The reference *I-V* is obtained by applying the same amount of incident power to the sample, homogeneously distributed. (b) A sensitivity analysis with respect to the lateral series resistance of the emitter layer $R_{\blacksquare\text{emitter}}$.

4.3.3 Discussion and conclusion

The cases shown above demonstrated that the nonuniform illumination can result in distinct variations comparing the uniformly distributed case. The reduction in P_{MPP} is apparent. Furthermore, increased overall series resistances are found in both cases in Figure 4.11a and Figure 4.12a. This is mainly due to the high lateral resistance ($R_{\blacksquare}$) of the emitter layer. The power losses on $R_{\blacksquare}$ increase with the increasing local current. Since CPV devices are designed to operate under high illumination intensity and thus high current, the effects of $R_{\blacksquare}$ need to be considered.

A sensitivity analysis is carried out to investigate the influences of $R_{\blacksquare}$ in the P_{MPP} under different illumination conditions. The results for the plano-convex case and the Fresnel case are plotted in Figure 4.11b and Figure 4.12b, respectively. The $R_{\blacksquare}$ varies from 10 Ω/□ to 100 Ω/□ with a step width 10 Ω/□. The relative variations between the uniform and nonuniform cases are given. The higher the $R_{\blacksquare}$, the stronger the impact on the P_{MPP}. This is also an indicator of the changes in the conversion efficiency η, defined by Equation (2.18), provided that the incident power P_{in} remains unchanged in the simulations.

In the plano-convex case, the uncertainty i.e. a manufacturing error can result in a reduction in the P_{MPP}, comparing the ideal scenario. In the Fresnel case, however, the uncertainty i.e. a distorted and misaligned lens produced a higher P_{MPP} (thus η) than the ideal condition. These case studies suggested that uncertainties in CPV systems may play both positive and negative roles. But this is highly dependent on the features of the input irradiance profile and therefore analyses should be done in a case-by-case manner.

Fresnel lenses based concentrations in Figure 4.12a revealed strong R_{sh} effects caused by the nonuniform illumination. An evident V_{OC} reduction can been read from the *I-V* curve if a nonuniform illumination profile is applied, comparing with the uniform case. In the plano-convex case shown in Figure 4.11a, the R_{sh} effects are not evident. This can be explained by local current absorption. The negative current i.e. absorption maps are provided in Figure 4.13. These were obtained by rescaling the current maps displayed in Figure 4.8 and Figure 4.10. The two maps of the Fresnel case contain large areas of negative current, caused by mismatch effects due to the

highly nonuniform irradiance profiles. These regions received no incident light and thus act as shunts. Since these "shunts" are nonlinear and the conductivity of the local diodes increases as the voltage increases, the global R_{sh} effects become recognisable in the high voltage region (Figure 4.12a). Practically, these effects can be weakened by using e.g. round-shaped cells that fit the illumination area.

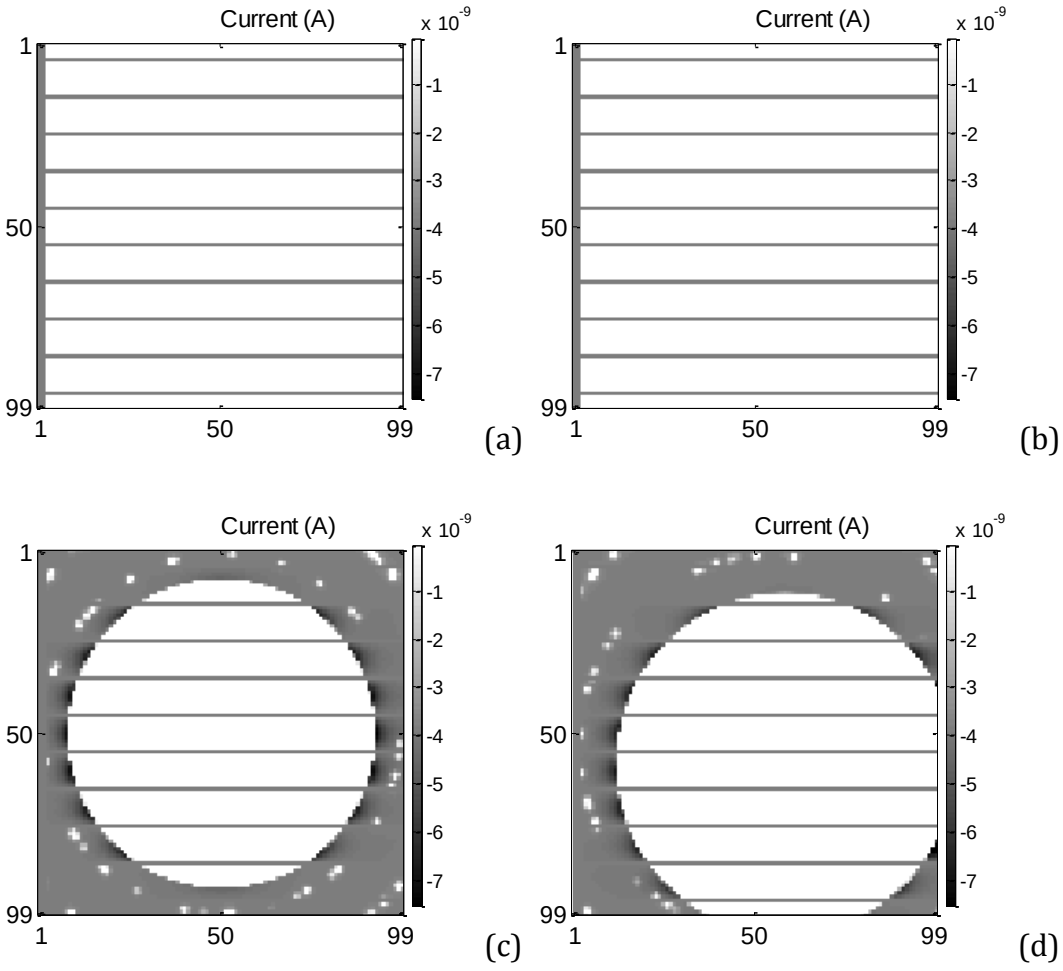

Figure 4.13. Rescaled current maps that show the current absorption (negative current) in the nonuniform cases illustrated in Figure 4.8 and Figure 4.10. The large areas of negative current in the two maps of the Fresnel case are caused by mismatch effects due to the highly nonuniform irradiance profiles. These regions received no incident light and thus act as nonlinear shunts.

Another factor that may result in shunt effects is lateral resistances. In the emitter layer, lateral voltage variations are established as current flows through $R_{\blacksquare}$. The distance that current flows depends on the design of the metal grid i.e. the spacing between fingers. In high current devices e.g. CPV, an increasing spacing can cause such a high local operating voltage that exceeds the V_{OC} of the local sub-cell. As a

consequence, the local diode model operates under a reverse current bias, i.e. absorbing rather than generating current. This effect is graphically shown in Figure 4.14 by running simulations with a cell with only 4 fingers (i.e. increased spacing). By using MJ devices, the local V_{OC} is increased and this effect barely exists. But the impacts of R_s should also be assessed since the increase of spacing between fingers causes stronger R_s effects.

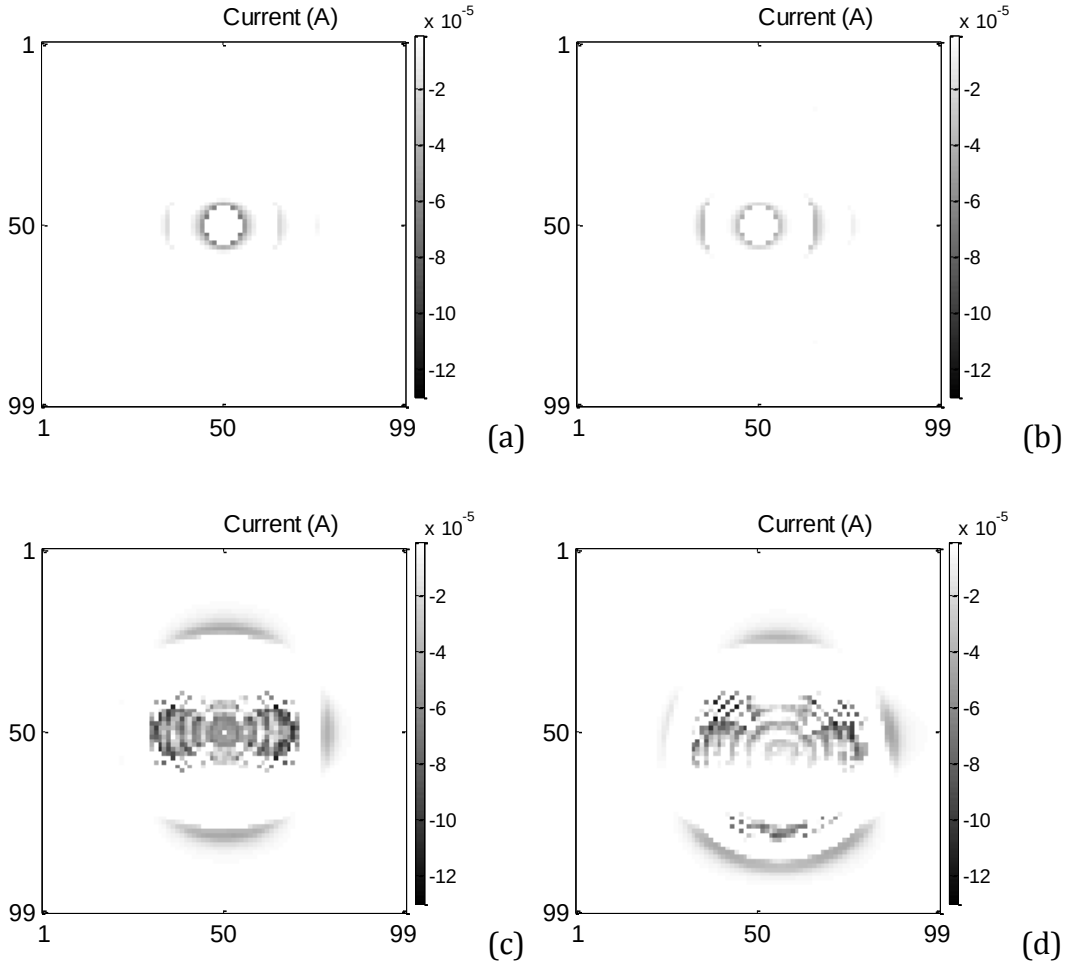

Figure 4.14. Current maps that show the current absorption (negative current) of a cell with increased finger spacing under nonuniform illumination. The increased spacing results in high lateral resistances and the local operating voltage can exceed the V_{OC} of the local diode model. Thus the affected sub-cells act as shunts.

In a real CPV system, the differences in the global performance must be understood in terms of e.g. quality of lenses and electrical mismatch between interconnected CPV units. This can be further studied by the module modelling tool as described in Section 4.2 for e.g. the prediction of the electrical energy yield and thus the

optimisation of the system. The variations read from the voltage and current maps in Figure 4.8 and Figure 4.10 can indicate potential harmful hot-spot heating effects in the devices. This may be analysed by means of a thermal model which can produce valuable information on e.g. the assessment of reliability of the systems.

4.4 Parameterisation of the spatially-resolved models

4.4.1 Global parameters

In the previous case study, virtual parameters and geometries were used to construct the sample for demonstration. To enable simulations for more realistic operating conditions, the input parameters of a device are required to be chosen such that the outputs of the model can match the measurement results of the sample involved. Therefore, for reproducing the behaviour of a real device, a parameterisation method is crucial.

The global parameterisation provides an effective way to estimate the electrical parameters from measured *I-V* characteristics, which is widely used now. Lumped single- and double- diode models are widely used for parameter extraction. As formulated by Equation (2.5) and (2.9) respectively, diode models are formulated by implicit nonlinear equations. In the single-diode model, for example, the undetermined parameters include the photocurrent I_{ph}, series resistance R_s, shunt resistance R_{sh}, as well as the diode parameters i.e. the saturation current I_{sat} and diode ideality factor n. To eliminate the area dependence, as introduced in Section 2.4.1, it is common to use the current density i.e. J_{ph} and J_{sat}, and the resistivity i.e. Γ_s and Γ_{sh}. n represents the material quality and is area-independent.

Since an *I-V* curve usually consists of dozens of data points, an over-determined nonlinear equation system can be generated. To extract parameters, various methods can be applied. Iterative fitting approaches are commonly used [35, 38, 46, 47, 58, 186-193]. A fitting algorithm is a method that “fine tunes” a given set of estimated parameters with respect to an error function. Initial values are estimated from the measured *I-V* curve, which are subsequently adjusted and in each iterative loop and are then used to calculate a new *I-V* curve. The iterative loops repeat until the error

between the generated and the measured curves has reached the desired maximum error threshold.

Araki *et al*. [58] suggested that strictly fitting the diode parameters can leads to unrealistic values e.g. $n > 2$ or negative resistances. To solve this problem, his work introduced a new parameter i.e. the non-dimensional length of surface voltage modulation *l*. However, since the use of ideality factor *n* is omitted, this method has not been widely accepted. Recently, parameter determination methods using the Lambert *W* function were reported in [186-190, 192-194]. By implementing the Lambert *W* function, the implicit diode equations can be rewritten into an explicit form, from which the analytical expressions of the undetermined parameters can be derived. The evaluation of the use of Lambert *W* function to extract diode parameters is provided in [192], indicating that good accuracy and applicability can be achieved. But the calculation speed can be slower than the fitting approaches.

In CREST, a fitting program WinFit was developed [46] for parameter extraction. The fitting process is shown in Figure 4.15, and described by Equation (4.4) and (4.5).

$$J = -J_{ph} + J_{sat}\left\{\exp\left[\frac{q(V - J\Gamma_s)}{nkT}\right] - 1\right\} + \frac{V - J\Gamma_s}{\Gamma_{sh}} \tag{4.4}$$

$$\begin{bmatrix} -1 & \exp\left[\dfrac{q(\boldsymbol{V} - \boldsymbol{J}\Gamma_s)}{nkT}\right] - 1 & \boldsymbol{V} - \boldsymbol{J}\Gamma_s \end{bmatrix} \begin{bmatrix} J_{ph} \\ J_{sat} \\ G_{sh} \end{bmatrix} = [\boldsymbol{J}] \tag{4.5}$$

In WinFit, the diode parameters are divided into two categories: linear and nonlinear, which simplifies the fitting processes [38]. In this hybrid approach, J_{ph}, J_{sat} and G_{sh} (i.e. $1/\Gamma_{sh}$) are considered to be linear while Γ_s and n are nonlinear. The linear and nonlinear parts are processed separately. The simplex algorithm is applied to update the nonlinear parameter set (n, Γ_s) in each iterative sequence of the fitting. With (n, Γ_s) fixed, Equation (4.4) becomes a linear equation with respect to the parameter set (J_{ph}, J_{sat}, G_{sh}), which can then be solved by using the singular value decomposition (SVD) [160]. The area criterion is chosen as the error function in the hybrid algorithm [46]. The same principle can be implemented for fitting the parameters for other model types, e.g. the double-diode model.

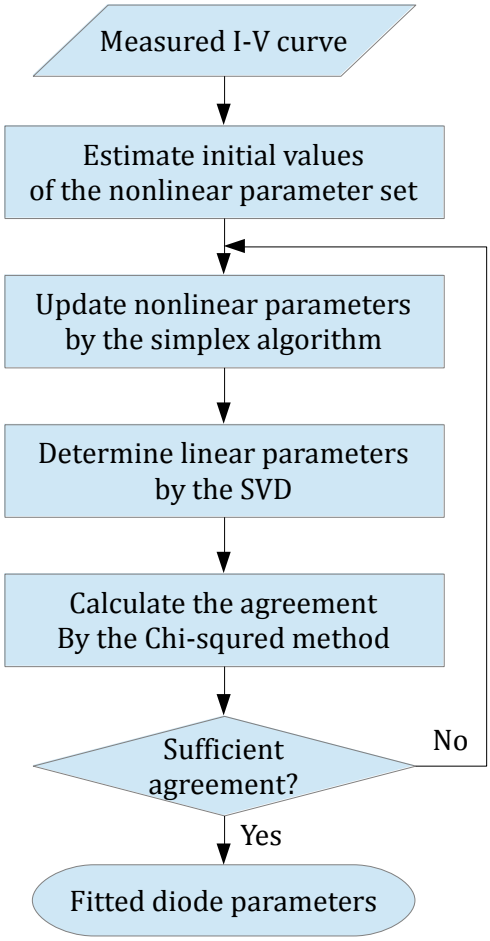

Figure 4.15. Flowchart of the hybrid algorithm for fitting an *I-V* curve. The fitting process is split into a nonlinear part and a linear part. The nonlinear part is handled by the simplex algorithm and the linear part is processed by the SVD. The area method is used as the error criterion.

4.4.2 Localised parameters

The localised parameters for an SRM need to be adjusted according to the geometries of the cell and the resolution of the model [71]. A local sub-cell (see Figure 3.1) at the location $\boldsymbol{r} = (x, y)$ requires a parameter set $I_{ph}(\boldsymbol{r})$, $I_{sat}(\boldsymbol{r})$, $n(\boldsymbol{r})$, $R_s^i(\boldsymbol{r})$, $R_{sh}(\boldsymbol{r})$, $R_{\blacksquare W}(\boldsymbol{r})$ and $R_{\blacksquare S}(\boldsymbol{r})$ to describe its behaviour. Here, $I_{ph}(\boldsymbol{r})$ is the photocurrent; $I_{sat}(\boldsymbol{r})$ is the diode saturation current; $n(\boldsymbol{r})$ is the diode ideality factor; $R_s^i(\boldsymbol{r})$ is the internal series resistance; $R_{sh}(\boldsymbol{r})$ is the shunt resistance; $R_{\blacksquare W}(\boldsymbol{r})$ and $R_{\blacksquare S}(\boldsymbol{r})$ are the lateral resistances, representing the "west" and "south" fractions (Figure 3.2) respectively.

Equation (4.6)-(4.15) show the corrections of the local parameters with respect to the geometries of a cell with L cm in length, W cm in width and d cm in thickness. The dimension of the SRM is R rows (width) and C columns (length).

$$I_{ph}(\boldsymbol{r}) = J_{ph}\frac{WL}{RC} \tag{4.6}$$

$$I_{sat}(\boldsymbol{r}) = J_{sat}\frac{WL}{RC} \tag{4.7}$$

$$R_s^i(\boldsymbol{r}) = \Gamma_s^i\frac{RC}{WL} \tag{4.8}$$

$$R_{sh}(\boldsymbol{r}) = \Gamma_{sh}\frac{RC}{WL} \tag{4.9}$$

$$n(\boldsymbol{r}) = n \tag{4.10}$$

Here, the ideality factor n remains constant and is independent of the geometries. This may clearly change if there are production issues in the device, but it is a good starting estimation. There is no known method to extract the localised diode ideality factor short of extracting the localised *I-V* characteristic from global measurements (as attempted in Chapter 5).

Lateral resistances for the front contact layer of a sub-cell model (Figure 3.3) are determined using following equations

$$R_{\blacksquare\mathrm{fw}}(\boldsymbol{r}) = \rho_{\mathrm{f}}\frac{W}{Ld} \tag{4.11}$$

$$R_{\blacksquare\mathrm{fs}}(\boldsymbol{r}) = \rho_{\mathrm{f}}\frac{L}{Wd} \tag{4.12}$$

where ρ_{f} is the resistivity of the front contact layer, in Ω·cm. Here, the subscripts "fw" and "fs" represent "front-west" and "front-south", respectively. Similarly, if a back contact layer is used, the "back-east" and "back-south" components in a sub-cell are calculated by

$$R_{\blacksquare\mathrm{be}}(\boldsymbol{r}) = \rho_{\mathrm{b}}\frac{W}{Ld} \tag{4.13}$$

$$R_{\blacksquare \mathrm{bs}}(\boldsymbol{r}) = \rho_{\mathrm{b}} \frac{L}{Wd} \tag{4.14}$$

where ρ_{b} is the resistivity of the back contact layer. Especially, for a square piece of specimen i.e. $W = L$, the concept of sheet resistance $R_{\blacksquare}$ is commonly used, as defined by

$$R_{\blacksquare} = \frac{\rho}{d} \tag{4.15}$$

Here, the unit of $R_{\blacksquare}$ is Ω/□ or Ω/square (sq.). For nonuniform materials e.g. nonuniformly doped emitter layer [25], the definition of $R_{\blacksquare}$ becomes

$$R_{\blacksquare} = \frac{1}{\int_0^d \frac{1}{\rho(x)} \mathrm{d}x} \tag{4.16}$$

In the global parameterisation, it is not able to separate the internal and lateral series resistances as the global R_s is simply represented by the summation of all the sources or series resistances [194-196]. In some 2-D simulation approaches, empirical values were chosen for the lateral resistances, e.g. as done in [17, 62]. Helbig *et al*. [57] proposed a method that can fit the $R_{\blacksquare}$ from EL measurements using a 1-D model, but neglecting R_s^i. There has not yet been a method that can accurately separate these two types of series resistances.

4.4.3 Effects of lateral resistances

The consideration of the lateral resistances distinguishes the SRMs. The utilisation of the resistor networks for the front and back contact schemes builds up connections between the sub-cells through the lateral current flows and lateral voltage drops. But at the same time, it complicates the characterisation by introducing a variable $R_{\blacksquare}$ which is implicit and is coupled with respect to the global resistive effects. Monokroussos *et al*. [195] proposed an initial study on the influences of the $R_{\blacksquare}$ with respect to the width of cells using a 1-D distributed model. In this section, 2-D simulations are used to demonstrate how $R_{\blacksquare}$ affects the overall and localised behaviour of PV devices.

The reported variations in $R_{\blacksquare}$ are large and dependent on the type of PV material. For example, the $R_{\blacksquare}$ for the TCO layer of a thin-film device is normally in the range 5 Ω/□

- 20 Ω/□ [7], while for the emitter layer of a c-Si device, it can be around 80 Ω/□ - 100 Ω/□ [17, 25]. To investigate the effects of varying $R_{\blacksquare}$ values on these two types of PV devices, PVONA-based simulations are setup to produce *I-V* curves under the STC, 2-D voltage and current distributions and line-plots of local voltage and current profiles.

The parameters for 3 virtual c-Si cells are listed in Table 4.3. The size of the cell is defined as 1 cm × 1 cm, with 1 busbar and 3 fingers. A 60 × 60 SRM is configured for a balance between fast computation speed and detailed investigation of localised electrical properties. In the SRM, 10 columns are configured for the busbar while each finger occupies one row. The distance between two fingers is 19 rows. 80 Ω/□, 100 Ω/□ and 120 Ω/□ are used as the $R_{\blacksquare}$ values of the emitter layer, while all other parameters remain unchanged. Figure 4.16, Figure 4.17 and Figure 4.18 show the simulation results.

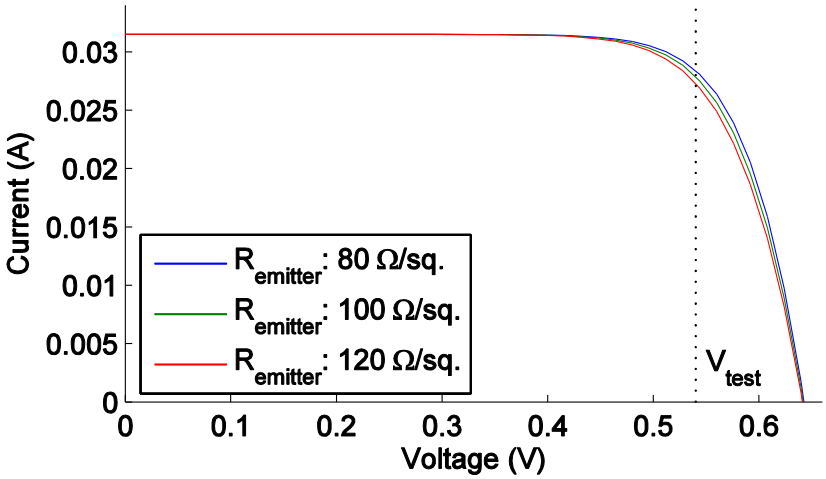

Figure 4.16. Simulated *I-V* curves of the 3 virtual c-Si PV cells with varying $R_{\blacksquare\text{emitter}}$ values. The change in lateral resistance mainly affects the global R_s and alters the fill factor.

As detailed in Figure 4.16, varying $R_{\blacksquare}$ values show an immediate impact on the overall *I-V* characteristic, by affecting the global R_s i.e. the variations in the knee area, as described in Section 2.4.2. The 2-D voltage and current maps shown in Figure 4.17 graphically illustrate the lateral variations in the cells. The 3 cells operate at the voltage bias V_{test} = 0.54 V, as marked in Figure 4.16. Waved patterns are observed in the voltage and current maps. This is because the length of the pathway for the

locally generated current to be collected by the metal grid is dependent on the position with respect to the fingers and the busbar [48]. The longer the distance, the more severe the voltage drops caused by the lateral current flow in the emitter layer. The local current changes accordingly following the nonlinear *I-V* relationship as formulated by Equation (2.6).

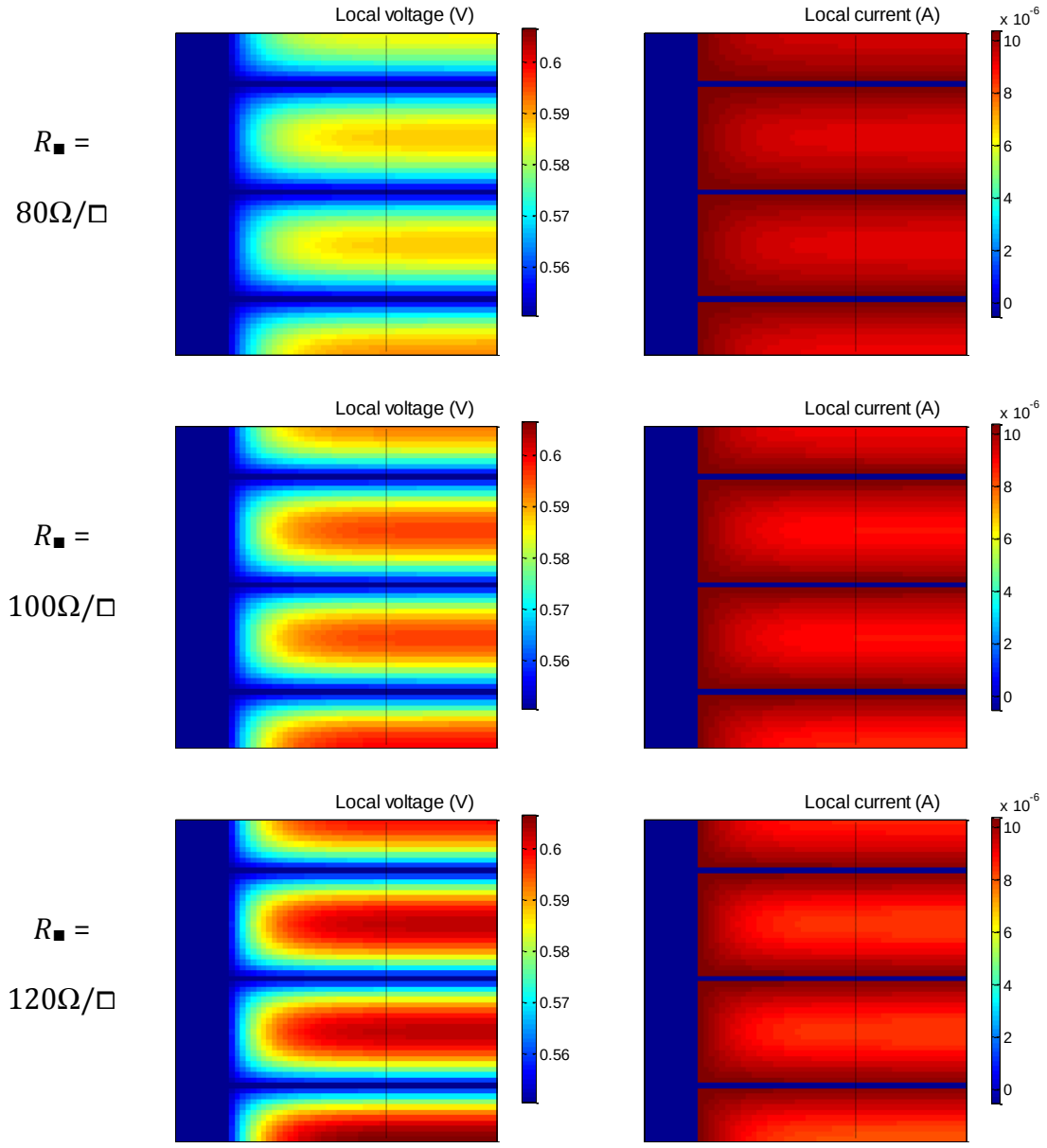

Figure 4.17. Simulated voltage and current maps at V_{test} = 0.54 V of the 3 virtual c-Si cells with varying $R_{\blacksquare emitter}$. The impacts of the lateral resistances on the local operating point is clearly visible.

The voltage maps clearly show that the largest $R_{\blacksquare}$ = 120 Ω/□ produces the highest peak voltages, and thus the most distinct lateral variations i.e. voltage drops in the

areas between the fingers. This is due to the fact that a higher $R_{\blacksquare}$ can result in greater voltage drops so that the voltage across the metal grid retains V_{test}. Meanwhile, a higher local voltage correspondingly results in a lower operating current, according to the local *I-V* characteristics, as shown in the current maps. The line-plots across the cells (as marked in Figure 4.17) in Figure 4.18 reveal this trend clearly.

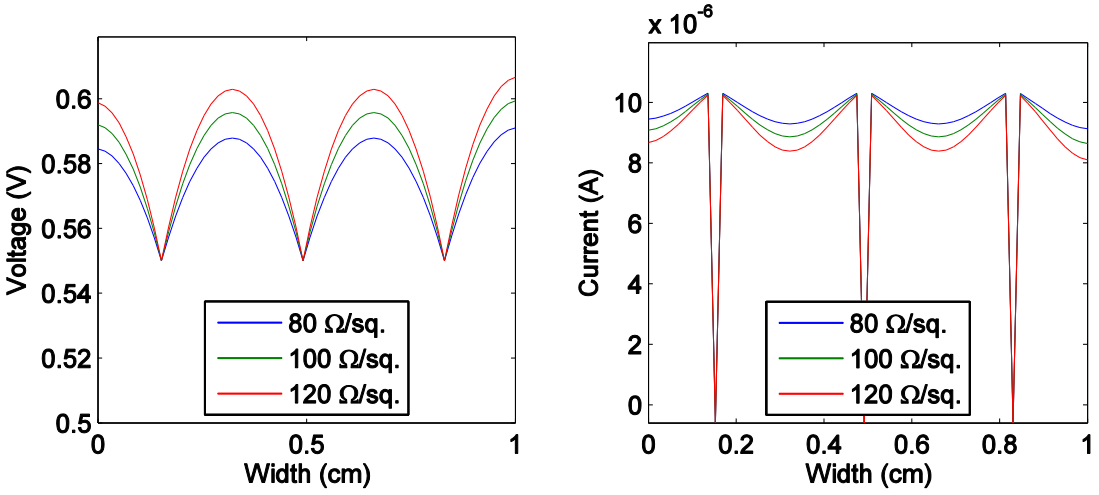

Figure 4.18. Line-plots of the voltage and current profiles across the 3 cells (marked in Figure 4.17) with varying $R_{\blacksquare\text{emitter}}$ values, demonstrating the variation in the local operating point caused by the lateral voltage drops.

The parameters for the virtual thin-film modules with varying $R_{\blacksquare\text{TCO}}$ values, 5 Ω/□, 10 Ω/□ and 15 Ω/□, are listed in Table 4.4. Each module is composed by 3 cells connected in series. The simulation of the module follows the rules introduced in Section 4.2. The size of a cell is defined as 3 cm × 0.9 cm. A 60 × 18 SRM is configured correspondingly for each cell. Figure 4.19, Figure 4.20 and Figure 4.21 show the simulation results.

Table 4.3
Electrical parameters for the SRMs of 3 virtual c-Si PV cells with varying $R_{\blacksquare}$ values of the emitter layer

J_{ph}	0.04 A/cm^2
J_{sat}	5.0×10^{-10} A/cm^2
n	1.4
Γ_{sh}	8.35×10^4 Ω·cm^2
Γ_s^i	0.03 Ω·cm^2
$R_{\blacksquare\text{grid}}$	1.0×10^{-3} Ω/□
$R_{\blacksquare\text{emitter}}$	80.0 Ω/□, 100.0 Ω/□, 120.0 Ω/□

Table 4.4
Electrical parameters for the SRMs of 3 virtual thin-film PV modules with varying $R_{\blacksquare}$ values of the TCO layer

J_{ph}	0.0135 A/cm^2
J_{sat}	1.0×10^{-10} A/cm^2
n	2.0
Γ_{sh}	5.30×10^4 Ω·cm^2
Γ_s^i	5.0 Ω·cm^2
$R_{\blacksquare TCO}$	5.0 Ω/□, 10.0 Ω/□, 15.0 Ω/□

Similarly, the immediate impacts of the increasing $R_{\blacksquare TCO}$ on the overall R_s can be seen from the *I-V* characteristics shown in Figure 4.19. Compared to c-Si devices, thin-film PV products are more sensitive to lateral resistive losses because the current needs to flow through the full width of the cell, while the distance between two fingers in a c-Si cell is normally only a few millimetres. The effects are clearly shown in Figure 4.20. An operating point is setup so that each cell operates at the same voltage bias V_{test} = 0.76 V, as marked in Figure 4.19. A large gradient can be seen in both the voltage and current maps. This also explains why the EL images of thin-film devices always show a gradient along the width of each cell. The line-plots across the width of the modules shown in Figure 4.21 more clearly reveal the patterns of the voltage drops due to the increasing $R_{\blacksquare}$ and the corresponding changes in the local current distribution.

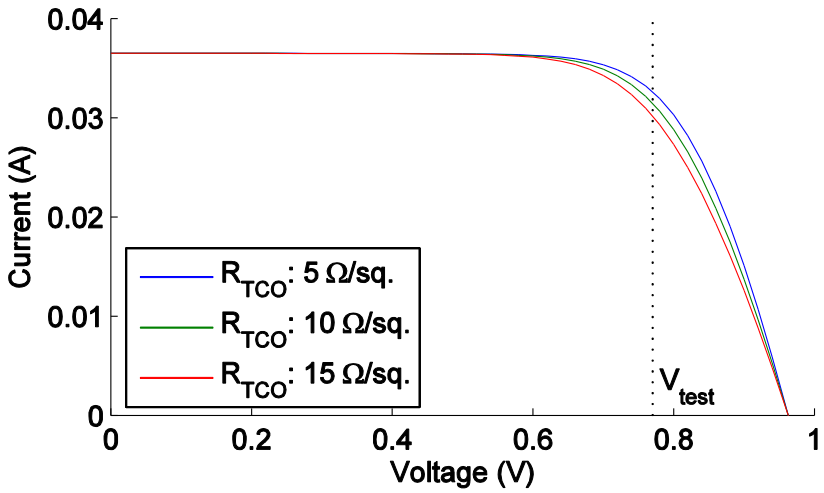

Figure 4.19. Simulated *I-V* curves of the 3 virtual thin-film PV cells with varying $R_{\blacksquare TCO}$. The changes in lateral resistance mainly affect the global R_s and alter the fill factor.

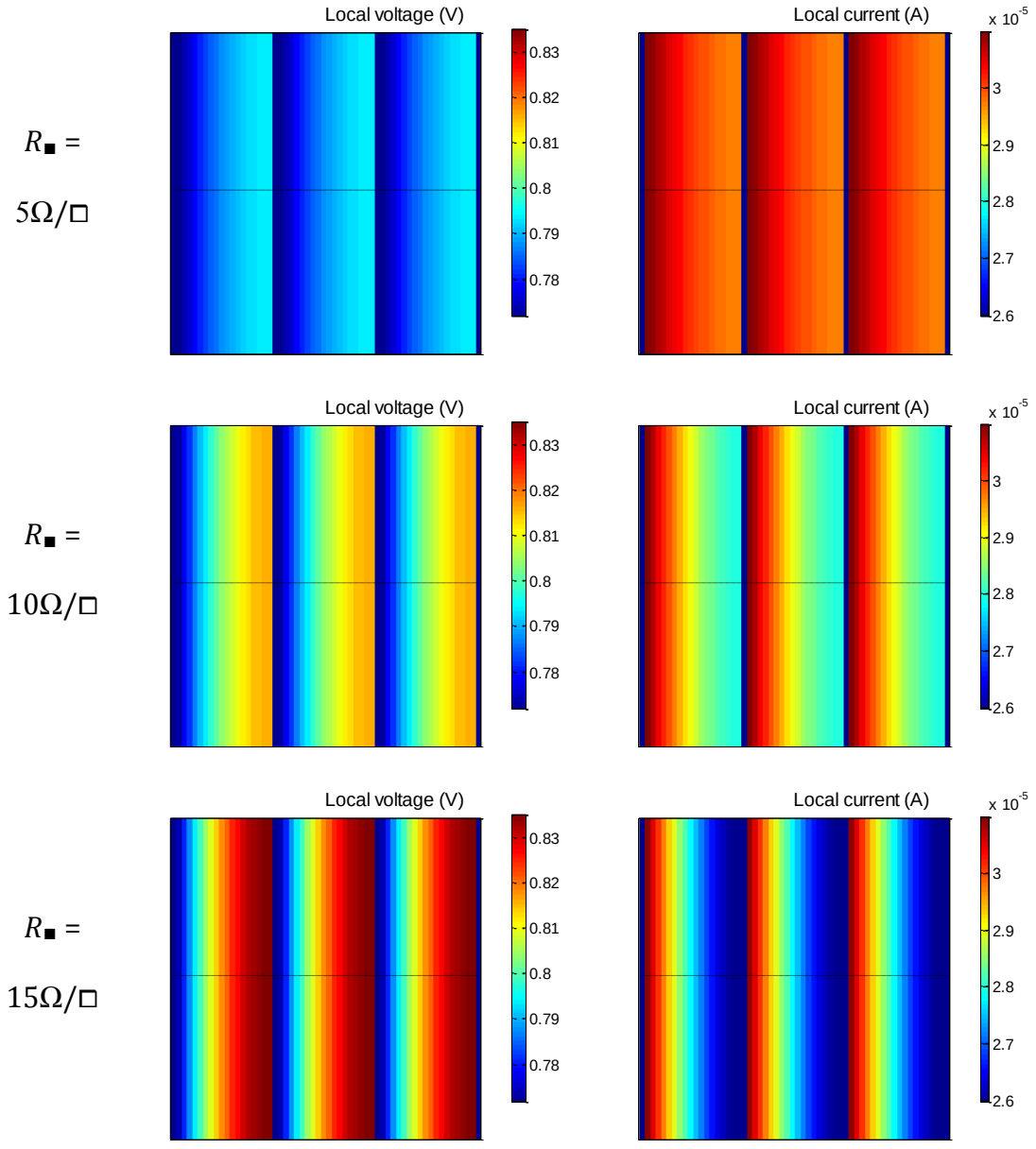

Figure 4.20. Simulated voltage and current maps of the 3 virtual 3-cell thin-film modules with varying $R_{\blacksquare TCO}$ at a voltage bias of V_{test} = 0.76 V showing the impact of the lateral resistance on the local operating points.

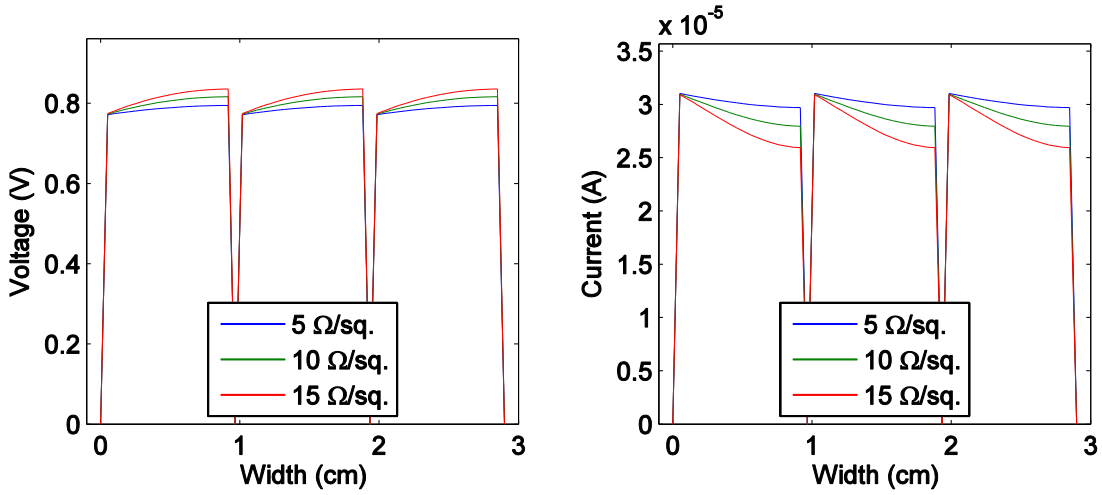

Figure 4.21. Line-plots of the voltage and current profiles along the width (marked in Figure 4.20) of the three virtual 3-cell thin-film modules with varying $R_{\blacksquare TCO}$. The variation in the local operating point caused by the lateral voltage drop is demonstrated.

4.5 Case study: Defects in EL measurements

4.5.1 Introduction and simulation setup

The case study presented in Section 4.2 mainly focused on the effects of external inhomogeneities i.e. the nonuniform illumination profiles. Here, the intrinsic inhomogeneities (i.e. defects) are investigated with the emphasis on localised parameterisation. One of the aims of developing the PVONA-based SRM is the analysis and quantification of imaging techniques e.g. EL. Here, this is investigated with two examples, which provide the initial steps towards 2-D analysis combining the SRMs and EL images.

Two EL images with notable defects are shown in Figure 4.22 and Figure 4.23 for a c-Si cell and for a thin-film a-Si module respectively. An SRM is setup for each sample with the parameters listed in Table 4.5 and Table 4.6. Some of these global parameters (marked in the tables) were extracted by the hybrid fitting algorithm introduced in Section 4.4.1 from the *I-V* curves measured under STC, and were correlated by Equations (4.6)-(4.10) with respect to the sizes of the SRMs.

Table 4.5
Initial electrical parameters for the SRM of the c-Si PV cell

J_{sat}	5.0×10^{-7} A/cm^2	Fitted from the *I-V* curve
n	1.12	
Γ_{sh}	8.35×10^{4} Ω·cm^2	
Γ_s^i	0.1 Ω·cm^2	Empirically chosen
$R_{\blacksquare\text{grid}}$	1.0×10^{-3} Ω/□	
$R_{\blacksquare\text{emitter}}$	80.0 Ω/□	

Table 4.6
Initial electrical parameters for the SRM of the thin-film a-Si PV modules

J_{sat}	3.35×10^{-9} A/cm^2	Fitted from the *I-V* curve
n	3.82	
Γ_{sh}	684.96 Ω·cm^2	
Γ_s^i	2.0 Ω·cm^2	Empirically chosen
$R_{\blacksquare\text{TCO}}$	15.0 Ω/□	

The simulation of an EL image is achieved by setting the illumination level of all the sub-cells to zero and reversing the direction of the current at the electrodes of the cell. The conversion from the local operating points to EL intensities is done using Equation (4.17) [9] at the sub-cell level,

$$\Phi(\boldsymbol{r}) = C\exp\left[\frac{qV_j(\boldsymbol{r})}{kT}\right] \tag{4.17}$$

where Φ is the local EL intensity; C is the calibration factor; and V_j is the local junction voltage.

It shows that by properly adjusting the local R_s^i and $R_{\blacksquare}$, an excellent reproduction of all features seen in the given examples can be achieved, although the calibration factor remains an unknown variable. The adjustment of parameters was done empirically, and the features are illustrated using a line-plot, as it demonstrates the agreement between simulations and measurements better.

4.5.2 Simulation results

Figure 4.22a shows the EL image (about 230 × 380 pixels) of a multi-crystalline Si PV cell taken under a current bias equal to its I_{SC} at STC (0.914 A). The EL intensity in the

areas between the fingers demonstrate trough-like pattern due to the impacts of lateral resistances in the emitter layer, as discussed in Section 4.4.3. The grains spread over the cell are most likely to be the material features e.g. grain boundaries. The characterisation of these features is out of the scope of this work. The EL image clearly reveals a dark strip in the rectangular area marked, which is typically caused by an interruption in, or lack of contact off, the metal finger. This is because the disconnected finger cuts the current pathway from the particular area to the metal contact grid and therefore the local current has to flow a longer distance to be collected. As a consequence, the increasing voltage drop results in lower local junction voltages, which are exponentially proportional to the EL intensity [121], as formulated by Equation (4.17).

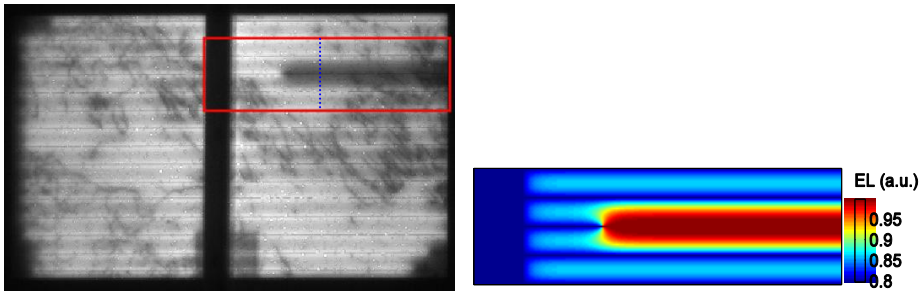

(a) (b)

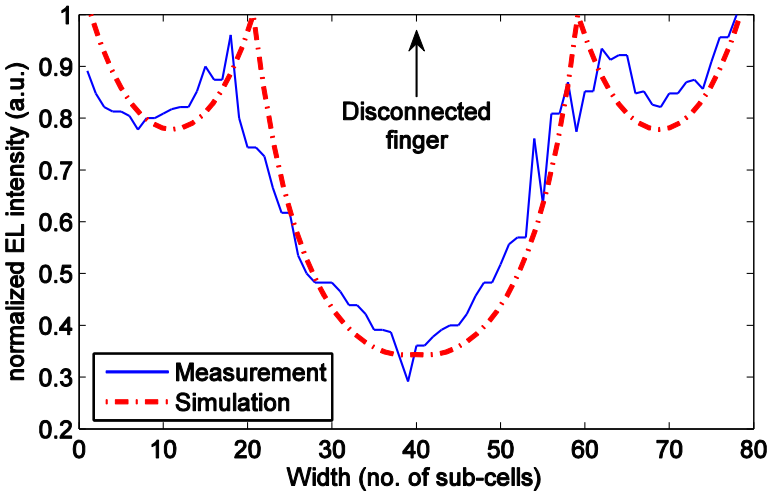

(c)

Figure 4.22. (a) EL image shows a partially disconnected finger in a c-Si cell; (b) Simulated EL image of the rectangle area marked in (a); (c) Comparison of the measured and simulated (normalised) EL profile of the line marked in (a). Agreement between the simulation and the measurement is demonstrated.

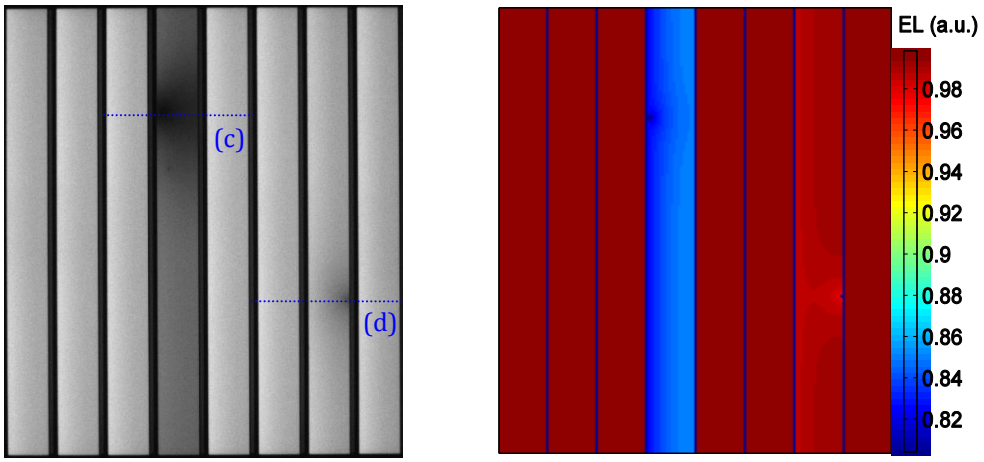

(a) (b)

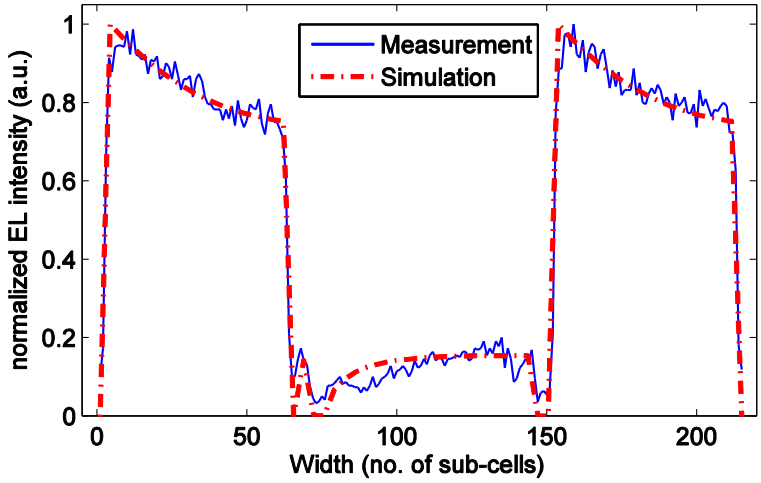

(c)

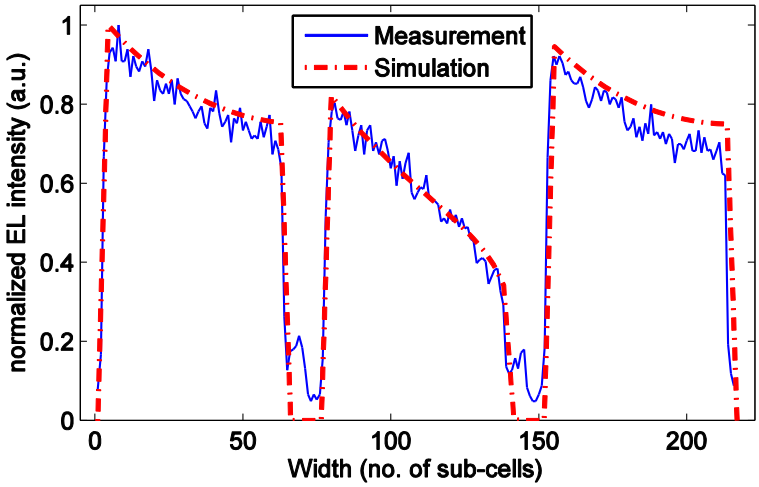

(d)

Figure 4.23. (a) EL images shows two local shunts in a thin-film a-Si mini-module; (b) Simulated EL image of the mini-module. (c) and (d) Comparison of the measured and simulated (normalised) EL profiles of the lines marked in (a). Good agreement between the simulation and the measurement is demonstrated.

In the 2-D modelling, the rectangle area was reconstructed using the same resolution (a 0.43 cm × 1.47 cm area with 65 × 220 nodes), with the initial parameters listed in Table 4.5. The disconnection point was simulated by setting the resistance of the finger at that location to $R_{\blacksquare\text{finger}} = R_{\blacksquare\text{emitter}}$. The Γ_s^i and $R_{\blacksquare}$ were gradually adjusted, stopped at Γ_s = 0.05 Ω·cm² and $R_{\blacksquare}$ = 65.0 Ω/□ respectively, so that the pattern of the simulated normalised EL profile in Figure 4.22b agrees with the original. The line-plot shown in Figure 4.23c clearly demonstrates the agreement. One can notice that the features are represented excellently but there remains some room for improvement in showing smaller variations of the device across area, i.e. a single set of parameters does not fully represent the measured data. This now demonstrates the strength of PVONA as well, as the simulation speed is high enough to develop an optimiser that will allow a better estimation of parameters within a reasonable time.

The approach can be extended to the module level by implementing the hierarchical architecture as described in Section 4.2. Figure 4.23 shows the EL image of a thin-film a-Si mini-module taken under the current bias equals to its I_{SC} at STC (0.034 A) and simulated global and line-scanned EL profiles. The gradient of the EL profile across each cell due to the voltage drop on lateral resistances is clearly in the line-plots. Two local shunts are found in the 4th cell and the 7th cell respectively. The initial parameters in Table 4.6 were used for the 680 × 65 SRMs to fit the EL images. For the stronger shunt in the 4th cell, Γ_s^i = 0.001 Ω·cm² and Γ_{sh} = 0.02 Ω·cm² were applied, and for the weaker shunt in the 7th cell, Γ_s^i and Γ_{sh} were set to 0.001 Ω·cm² and 0.065 Ω·cm² respectively to fit the EL profiles.

4.5.3 Discussion and conclusion

The consideration of lateral resistances allows the description of the lateral variations in PV devices detected by imaging techniques such as EL. By configuring an SRM with a resolution equivalent to the EL image, a one-to-one relationship can be established between the simulation results and measurements. Practically, empirical parameter adjustments are effective to reconstruct features caused by defects such as shunts and disconnected fingers, as investigated, seen in the measurement results.

There is still a shortage of methods to interpret material-related properties such as grain boundaries in Figure 4.22a from EL images. But it is important to separate

material features like this from defects since they both result in variations in EL images and otherwise the characterisation results can mislead. Further research can be achieved by utilising spectral characterisation techniques [197] since the grain boundaries or dislocations are recombination-active and can show specific spectral response [198].

The jitters seen in Figure 4.22c, Figure 4.23c and Figure 4.23d are most likely not due to production inhomogeneities in the device but more likely due to read out issues of the EL camera involved. Image filtering techniques can be applied to improve the quality of the EL images. For example, a medium filter is used in the next chapter for pre-processing EL images. Further work is required to firstly qualify the EL camera for a better image quality. In order to move this towards a systematic quantitative characterisation, a fitting-based automated process is desired. This is applicable by employing the effective PVONA tools and will be introduced in the next chapter. This approach can also work for other types of defects e.g. cracks. The fault analysis like these can provide valuable information for the assessment of the performance of PV devices in different stages in their lifecycle.

4.6 Chapter conclusions

The work in this chapter showed how PVONA-based SRMs are used to run high resolution simulations for various purposes. Internal and external spatial inhomogeneities can be quantitatively modelled and investigated. By utilising PVONA tools, the simulation for a high-resolution (e.g. equivalent to an EL image) takes up to only a few minutes. This allows the quantification of spatially-resolved analysis of PV devices applicable for real characterisation tasks, while it was not widely used before due to inefficient solving processes limited by highly complexity of inhomogeneities.

The joint modelling framework in the case study showed that the nonuniformity of illumination can have evident impacts on the global *I-V* characteristics of devices in terms of the R_s and R_{sh} effects, and thus the P_{MPP} i.e. the conversion efficiency. The performance of a CPV unit can also be affected by the uncertainties introduced in various stages. The changes of P_{MPP} with respect to the $R_{\blacksquare}$ were quantitatively investigated by means of a sensitivity analysis. It suggested that the losses in a CPV

system are due to a mixed effect of both design parameters of the devices and the inhomogeneous irradiance. For understanding the performance of various types of systems with different types of inhomogeneities, case-by-case investigations should be carried out.

The joint modelling framework showed the potential of the PVONA tools in various aspects. Firstly, the environmental interface can be used to combine not only optical but also thermal models to study e.g. hot spot effects in devices. Secondly, the PVONA-based simulations can assist optimising the performance of CPV units in terms of selecting optical components and PV devices by modelling and quantifying the potential loss mechanisms. This can be further extended to achieve system-level design and optimisation by considering mismatch losses. Thirdly, cell designers may be benefit from spatially-resolved simulations by investigating the impacts of varying design parameters e.g. finger spacing.

The consideration of lateral resistances allows SRMs to quantitatively reconstruct EL images. One-to-one links have been established between an EL images and an SRM with the same resolution. This allows pixellation of localised electrical properties, which helps detailed investigation of spatially-resolved characterisation methods. The achievement presented here is a step towards quantitative analysis as it allows simulations in reasonable times and reasonable computing expense for the potential iterative-based 2-D parameter determination algorithms, which will be investigated in the following chapter.

Chapter 5

Extraction of local electrical parameters of thin-film PV devices using electroluminescence imaging

5.1 Overview

The previous chapter discussed some of the basic aspects of spatially-resolved parameterisation of PV devices. Quantitative parameter extraction from 2-D measurements such as EL imaging is gaining attention in research and industrial applications. An EL system in a production line can examine the final products for otherwise invisible or underlying defects that may cause unexpected performance degradation, as a means of quality control. However, the EL applications are mostly qualitative nowadays and require quantification. The case study given in the previous chapter showed that by empirically adjusting the local parameters it was possible to reproduce the measurement results with simulations, from which localised parameters of a 2-D SRM for describing defects were determined. However, in practice, adjusting local parameters empirically is inefficient, and more systematic approaches are needed.

Studies on various imaging techniques for quantitative interpretation have been reported in recent years. Ramspeck *et al.* [19] developed the recombination current and series resistance imaging (RESI) method that combines an EL image and a dark-LIT image to calculate the resistance profile. Hinken *et al*. [128] proposed a method that uses differential EL images with respect to the applied voltage to yield the effective series resistance map. Kampwerth *et al*. method [20] utilized two luminescence images obtained under two different operating points but with the same luminescence intensities to map the effective series resistances. Breitenstein *et al*. [124] introduced an iterative algorithm to fit the local series resistances and the dark saturation current from EL images taken at two bias levels. Shen *et al*. [108] developed a PL-based parameter extraction method that utilizes at least 5 PL images taken under different conditions to derive an abundant set of localized parameters including voltage, current density, power density, efficiency, fill factor, series resistance and dark saturation current densities of the double-diode model.

From the reported methods it is apparent that distributed models were utilised to describe the localised behaviour of the cells and to establish a one-to-one relationship with the measured images. However, the common assumption made in many methods [19, 20, 108, 124, 128] is that the local series resistance is

represented by a lumped "effective series resistance (R_s^*)", in which the effects from the internal (e.g. the resistance in the junction) and the external (e.g. the lateral resistance in the contact schemes) are mixed. The use of R_s^* simplifies the theoretical analyses for building up links between a 2-D model and measurement results i.e. the luminescence images. However, the validity of using R_s^* in 2-D modelling has not been fully proven. For example, results from 2-D simulations in [18] demonstrated that the R_s^* shows a nonlinear voltage-dependent behaviour, and thus can result in misinterpretation of the local electrical properties in a full 2-D model. Therefore, to fully describe the 2-D properties of a device, efforts need to be made to separate the lateral resistances from the overall series resistance effects.

In this chapter, a new method to extract the full parameter set of thin-film (TF) devices using the 2-D SRMs is demonstrated. TF devices are used because they suffer more severely from lateral resistance losses than c-Si devices due to the use of the transparent conducting oxide (TCO) layer and thus it is more relevant to these devices. This new method utilises EL images and PVONA-based 2-D fitting to separate the lateral resistances from the overall series resistance effects. It requires a reference sample without defects and employs fast 2-D fittings to produce the full parameter set of the SRM that can simultaneously reconstruct the measurement results of dark *I*-*V* and EL images taken under different electrical bias conditions. The extracted parameters can then be used as the initial values for further quantitative analysis of defects e.g. shunts.

This chapter first explains the theoretical principles of the EL measurements and their relationship with the local device properties including the lateral resistance. This is followed by a detailed description of the newly developed characterisation method. Furthermore, the method is verified by PVONA-based virtual simulations and validated in a case study using TF amorphous silicon (a-Si) modules.

5.2 EL imaging of PV devices

5.2.1 Basic theory of EL imaging

A PV cell can be regarded as a large flat diode with an optimised balance between light absorption and charge carrier collection. The principle of EL in a PV cell is

similar to that of a light emitting diode (LED). With a certain level of injected current, band-to-band radiative recombination occurs in a cell, generating light emission (see Section 2.2). Although in a piece of indirect bandgap semiconductor [23], e.g. silicon, the intensity of radiative recombination is relatively low compared to Shockley-Read-Hall recombination and Auger recombination, there is still a flux of photons that can be sensed by a detector [199].

The emission of EL is the reciprocal process to the normal operation of a PV cell. Considering a *p*-*n* junction, according to the reciprocity theorem [139], the typical conversion of the forward electrical bias into the EL intensity at position $\boldsymbol{r} = (x, y)$ can be formulated by

$$\Phi_{\mathrm{EL}}(E, \boldsymbol{r}) = Q_e(E, \boldsymbol{r})\phi_{bb}(E)\exp\left[\frac{qV_j(\boldsymbol{r})}{kT}\right] \tag{5.1}$$

where $\Phi_{\mathrm{EL}}(E, \boldsymbol{r})$ is the local EL intensity; E is photon energy; $V_j(\boldsymbol{r})$ is the local internal junction voltage; kT/q is the thermal voltage. $Q_e(E, \boldsymbol{r})$ and $\phi_{bb}(E)$ are the local external quantum efficiency (EQE) and the spectral photon density of a black body, respectively, which can be further expanded as

$$Q_e(E, \boldsymbol{r}) = [1 - R(E, \boldsymbol{r})]Q_i(E, \boldsymbol{r}) \tag{5.2}$$

$$\phi_{bb}(E) = \frac{2\pi E^2/(h^3c^2)}{\exp(E/kT) - 1} \tag{5.3}$$

where $R(E, \boldsymbol{r})$ is the local front surface reflectance; $Q_i(E, \boldsymbol{r})$ is the local internal quantum efficiency; h is the Planck's constant; and c is the speed of light in vacuum.

The local emission profile reveals the quality of the material in that particular region. However, to record and analyse the local EL spectrum by using a monochromator (also referred to as localised EL spectroscopy) can be very time-consuming. Instead, a charge-coupled device (CCD) camera was used as the detector of EL signals in Fuyuki's first study of EL imaging for characterisation of PV cells in 2005, enabling fast EL measurements within only a few seconds [9]. Imaging-based EL then became a valuable tool for fast and spatially-resolved characterisation for PV cells and modules [118, 121, 200].

The intensity of EL signal captured by a camera depends on the sensitivity $Q_{cam}(E)$ of the CCD. The local EL signal detected by the camera $S_{cam}(\boldsymbol{r})$ at each pixel can be derived by

$$S_{cam}(\boldsymbol{r}) = \int Q_{cam}(E) Q_e(E, \boldsymbol{r}) \phi_{bb}(E) \mathrm{d}E \exp\left[\frac{qV_j(\boldsymbol{r})}{kT}\right] \tag{5.4}$$

In this sense, EL imaging is able to capture all the losses occurring in a PV cell in a relatively short period of time with high spatial resolution [199]. Here, the effects of optical losses in the camera e.g. uncertainties from the lenses are neglected. The full process for calibrating an EL system is detailed in [201]. However, the validity of this simplified correlation was proven in [57] and is suitable for demonstration purposes in this thesis.

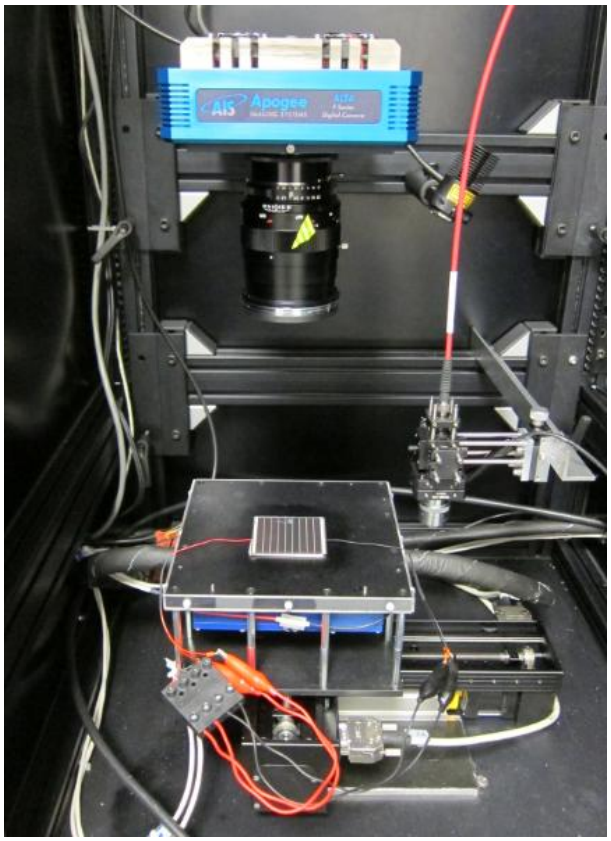

Figure 5.1. Photograph shows the setup of a global EL measurement system in CREST. An external forward electrical bias is applied to the sample under test to excite radiative recombination. The emission profile is recorded by the Si CCD chip in the camera.

A typical EL imaging measurement system was illustrated in Figure 2.19. Figure 5.1 shows the setup of the EL imaging system in CREST [197]. The camera used in is a 16-bit Apogee Alta F-series camera with a cooled 8.3 mega-pixel Si CCD. The temperature of the detector is actively stabilised at -10°C to reduce thermal bias current and to regulate the spectral response. To remove the background signal, an image is taken with the same exposure time as applied to the sample, but without excitation (electrical bias) as the reference dark image which is then subtracted from the raw EL images. Furthermore, salt-and-pepper noise (i.e. defective bright and dark pixels) can be removed by applying e.g. a 3 × 3 median filter with threshold (i.e. if the pixel value exceeds the median of the surrounding pixels by more than the threshold, its value is set to the median). An XY-stage is used to adjust the position of the sample in the field of view.

5.2.2 Characterisation of PV cells using EL

From Equation (5.4) it is apparent that the factors Q_{cam} and ϕ_{bb} depend on only the photon energy E but not the location $\boldsymbol{r}$ on the device tested. This is because the lateral variations obtained from the resultant EL image originate only from the lateral variations of Q_e [Equation (5.2)] and V_j. Here, the assumption that Q_e is spatially independent is made. This is reasonable because, according to in Equation (5.4), the influences from the exponential dependence of the variations of V_j can overwhelm the possible spatial variations of Q_e [199]. Consequently, Equation (5.4) can be rearranged into

$$V_j(\boldsymbol{r}) = \frac{kT}{q}\left\{\ln[S_{cam}(\boldsymbol{r})] - \ln\left[\int Q_{cam}(E)Q_e(E)\phi_{bb}(E)\mathrm{d}E\right]\right\} \tag{5.5}$$

and hence

$$\frac{kT}{q}\ln[S_{cam}(\boldsymbol{r})] = V_j(\boldsymbol{r}) + \frac{kT}{q}\ln\left[\int Q_{cam}(E)Q_e(E)\phi_{bb}(E)\mathrm{d}E\right] = V_j(\boldsymbol{r}) + V_{\mathrm{offs}} \tag{5.6}$$

where V_{offs} is an unknown spatially constant offset voltage. By applying Equation (5.6), an EL image can therefore be translated into a relative image of the spatial variations of the local junction voltages. The voltage drop $\Delta V(\boldsymbol{r}_1, \boldsymbol{r}_2)$ between two neighbouring points at $\boldsymbol{r}_1$ and $\boldsymbol{r}_2$ contains the influences from both the lateral

resistances and the internal series resistances. By neglecting the internal series resistances, as done in [57], the voltage difference $\Delta V(\boldsymbol{r}_1, \boldsymbol{r}_2)$ is considered due to the lateral resistances.

Practically, Equation (5.4) can be further approximated by introducing a local calibration factor $C(\boldsymbol{r})$, yielding a widely used correlation between the EL signal and the junction voltage [9, 121, 124]

$$S_{cam}(\boldsymbol{r}) = C(\boldsymbol{r})\exp\left[\frac{qV_j(\boldsymbol{r})}{kT}\right] \tag{5.7}$$

or

$$V_j(\boldsymbol{r}) = \frac{kT}{q}\ln[S_{cam}(\boldsymbol{r})] + V_{\text{offs}}(\boldsymbol{r}) \tag{5.8}$$

where $V_{offs}(\boldsymbol{r})$ is a local offset constant. If the spatial variation of $C(\boldsymbol{r})$ is negligible, as assumed in some studies [20, 128], the determination of the local junction voltage can be further simplified. The local junction voltage $V_j(\boldsymbol{r})$ directly relates to the local current $I_d(\boldsymbol{r})$ of the diode by

$$I_d(\boldsymbol{r}) = I_{sat}(\boldsymbol{r})\left\{\exp\left[\frac{qV_j(\boldsymbol{r})}{n(\boldsymbol{r})kT}\right] - 1\right\} \approx I_{sat}(\boldsymbol{r})\exp\left[\frac{qV_j(\boldsymbol{r})}{nkT}\right] \tag{5.9}$$

where $I_{sat}(\boldsymbol{r})$ is the local dark saturation current and n is the ideality factor. Consequently, a connection between the EL intensity and the local saturation current can be established and is approximated by

$$\ln[S_{cam}(\boldsymbol{r})] = n\ln[I_{sat}(\boldsymbol{r})] + A(\boldsymbol{r}) \tag{5.10}$$

where $A(\boldsymbol{r})$ is a spatially dependent constant, as introduced in [121].The calibration constants and the offset constants need to be eliminated by means of a calibration processes such as the subtraction of multiple EL images [128] before a quantitative analysis of the local electrical properties can be achieved.

5.2.3 Simulation of EL using PVONA

The simulation of EL images with the PVONA-based SRM helps to establish the relationship between the local electrical properties and the EL signals under

specified measurement conditions. As illustrated in the previous chapters, the PVONA toolset is equipped with a flexible spatially-resolved model structure and abundant programming interfaces to cope with simulations for PV cells with different geometries and varying environmental conditions. The steps used to configure a simulation of EL images is illustrated in Figure 5.2. A function *ELSim* is defined in the PVONA library to include these processes.

The procedure starts by configuring the model of the cell as detailed in Section 3.2. Secondly, the environmental conditions i.e. irradiance and temperature are set. Since the EL measurements are carried out in the dark, there is no photocurrent generation in the cell, and the local irradiance is set as nil. The local temperature is uniformly configured to 25 °C by default, but can be individually defined. After these two steps, the external current or voltage bias can be applied by invoking the PVNOA interface function *GetOPbyI* or *GetOPbyV* (see Table 3.2) respectively, and the local operating points are modelled and recoded. In addition, the dark *I-V* characteristics of the cell can be simulated by an I-based or V-based sweep.

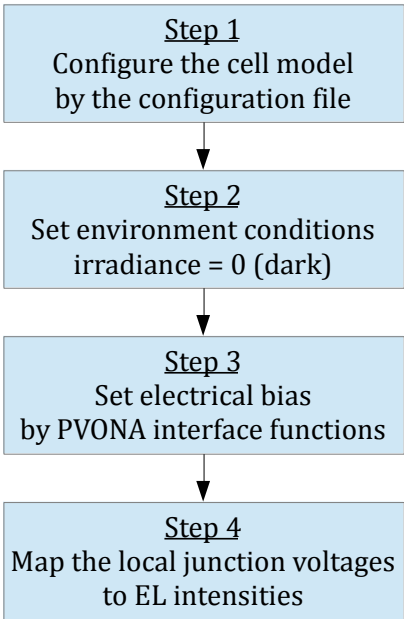

Figure 5.2. Flowchart shows the steps to generate an EL image in simulation using the PVONA toolset. All these steps can be processed by PVONA programming interfaces. The procedure is enclosed in the *ELSim* function in the PVONA framework and is subject to customisation.

The local operating points are converted to EL signals by utilising Equation (5.7). The local calibration factor $C(\boldsymbol{r})$ is normally unknown. However, as discussed earlier, $C(\boldsymbol{r})$ can be assumed to be location-independent. This yields a linear relationship between the EL intensity and the exponential of the junction voltage [121]

$$S_{EL}(\boldsymbol{r}) \propto \exp\left[\frac{qV_j(\boldsymbol{r})}{kT}\right] \tag{5.11}$$

Since the local V_j values are available through the PVONA-based SRM solver, this correlation is therefore used to translate the local junction voltages into relative EL signals in the simulation, while there is a linear scaling factor missing.

5.3 Determination of local electrical parameters and verification by simulations

5.3.1 Investigation of the effective series resistance

SRMs are desired for quantitative spatially-resolved analysis of the localised behaviour of devices, ideally in the same resolution as the measured images. The utilisation of the resistor network for the contact scheme in the SRM builds up connections between the sub-cells through lateral current flow and lateral voltage drop. But at the same time, it complicates the characterisation by introducing a variable $R_{\blacksquare}$ which is implicit and is coupled with respect to the global resistive effects.

As explained earlier in Section 5.1, a number of EL-based parameter extraction methods [19, 20, 108, 124, 128] have been published to-date. However, the underlying assumption of the methods is an over-simplification. It is assumed that the local series resistance (R_s) is equal to a lumped "effective R_s" (R_s^*), as defined by Equation (5.12). This combines the effects of internal (e.g. the resistance in the junction) and external (e.g. the lateral resistance in the contact schemes) resistances. At a location $\boldsymbol{r} = (x, y)$ in a cell, $R_s^*(\boldsymbol{r})$ is defined as the voltage difference between the local junction (i.e. the local diode) and the terminal divided by the local current.

$$R_s^*(\boldsymbol{r}) = \frac{V_{term} - V_j(\boldsymbol{r})}{I(\boldsymbol{r})} = \frac{\Delta V(\boldsymbol{r})}{I(\boldsymbol{r})} \tag{5.12}$$

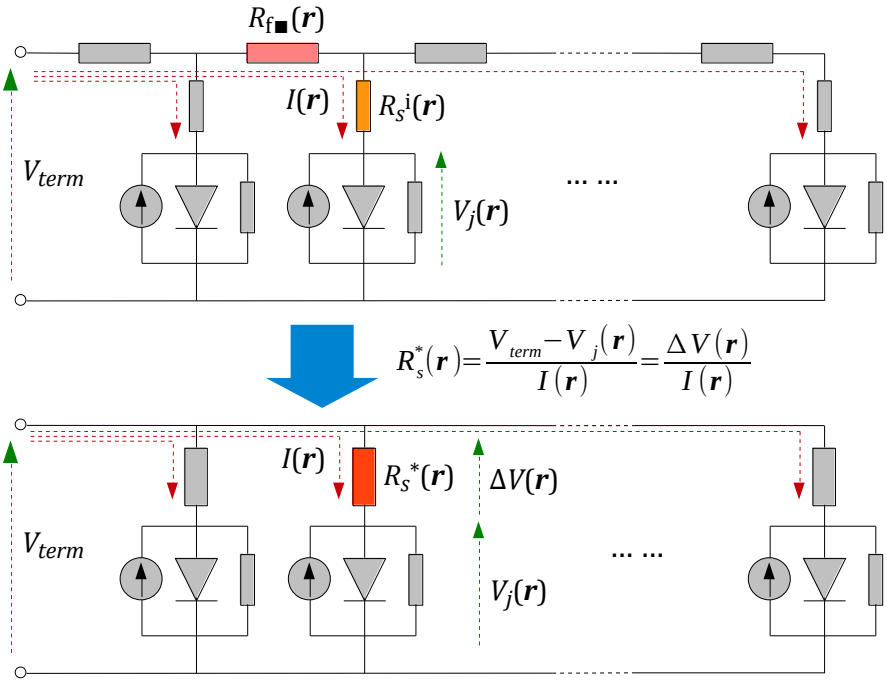

(a)

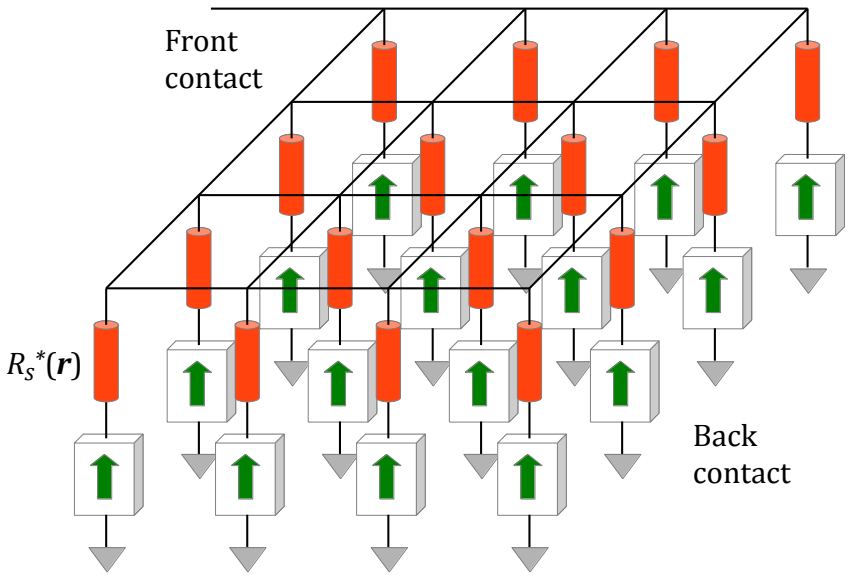

(b)

Figure 5.3. (a) 1-D and (b) 2-D schematics that demonstrate the use of effective series resistance R_s^* in SRMs. At location $\boldsymbol{r}$, an accumulated local R_s is used to represent the mixed effects of the intrinsic resistance and lateral resistances. The SRM of the cell becomes an array of diode models (with R_s^*) connected in parallel.

Here, V_{term} is the global operating voltage obtained at the terminal of the cell and $V_j(\boldsymbol{r})$ is the local junction voltage. The concept of $R_s^*(\boldsymbol{r})$ is graphically demonstrated by a 1-D distributed model in Figure 5.3a. $R_s^*(\boldsymbol{r})$ contains the $R_{\blacksquare}$ effects along the current pathway and the model of a cell becomes an array of diode models connected in parallel. In a 2-D SRM, an area effect is contained in the local $R_s^*(\boldsymbol{r})$. In the model shown in Figure 5.3b, each local $R_s^*(\boldsymbol{r})$ represents accumulated R_s effects between the sub-cell and the terminal. The use of R_s^* simplifies the theoretical analyses for building up links between an SRM and measurement results e.g. EL images.

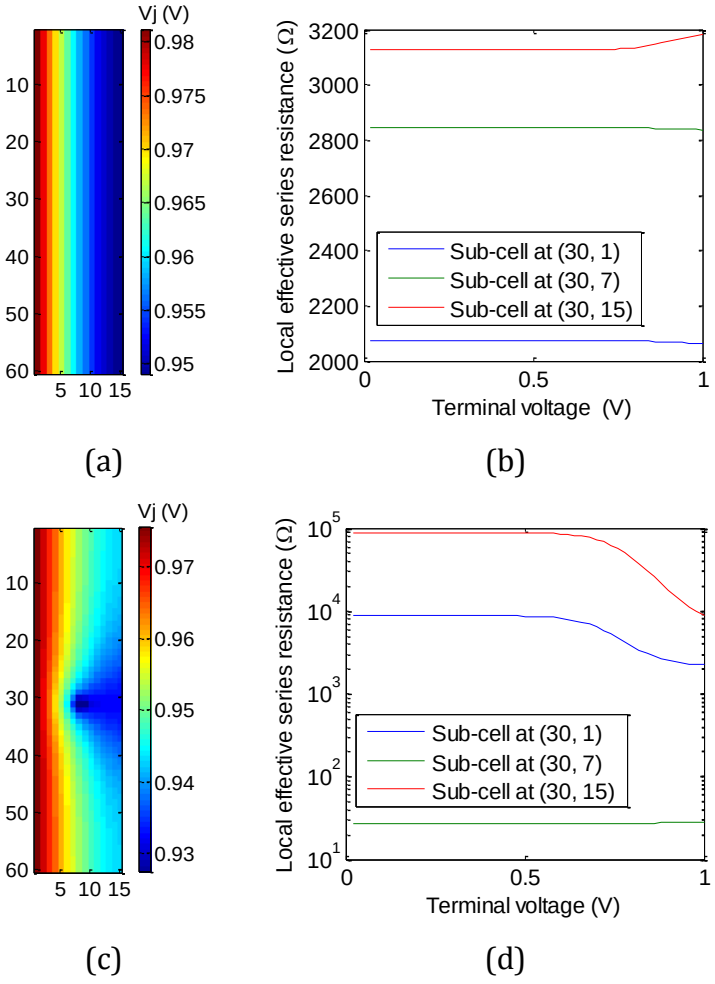

Figure 5.4. (a)(c) V_j maps obtained under EL conditions with V_{term} = 1.0 V and (b)(d) local R_s^* with respect to changing V_{term} of the SRM of 3 sub-cells in a thin-film cell. R_s^* is nonlinear and voltage-dependent. The local R_s^* of the same location from the shunted and un-shunted cases cannot match to each other.

This is because $V_j(\boldsymbol{r})$ and $I(\boldsymbol{r})$ in Equation (4.3) holds a nonlinear relationship, i.e. the diode equation, where the conductivity of the diode increases exponentially along with the local voltage. The local shunt becomes a current sink and extracts current

from the surrounding area through $R_{\blacksquare}$. This implicitly changes the local operating points in the affected area and therefore brings greater uncertainty. This means that the use of the R_s^* can result in misinterpretation of the localised behaviour in PV cells.

5.3.2 Method and simulation setup

The method aims to quantitatively determine a parameter set for the full 2-D SRM of the TF devices including separated lateral resistances from the overall series resistance effects. The structure of a full 2-D SRM has been demonstrated in Figure 3.1. The dimension of the mesh grid is adjustable to fit the resolution of EL images. For demonstration, the type of the local diode model is the single-diode model, although in principle it can be adjusted for using other types of models as introduced in Section 2.3. Here, each local single-diode model has 5 parameters: I_{ph}, I_{sat}, n, R_{sh} and R_s^i. The lateral resistance of the front TCO layer is described by the sheet resistance ($R_{\blacksquare}$), while that of the metal back contact is neglected, as done in [58, 71].

As discussed earlier, a sub-cell in a 2-D SRM is not simply a two-electrode component with respect to the positive and negative terminals of the cell, due to the existence of the resistor network of the contact schemes. It is thus impossible to analytically formulate equations from which the local electrical parameters can be derived by giving only the input-output relationship at the terminals or the relative EL measurement results as done in the earlier detailed methods, which use the simplified models with the R_s^*. Instead, a fitting algorithm is utilised and is more effective in parameter determination in such a 2-D case.

The method described here requires a reference sample without visible defects, which can be confirmed by EL measurements. This is because the electrical mismatch effects may significantly reshape the *I-V* characteristics and thus the global parameters extracted by the hybrid fitting algorithm can become an inaccurate coarse approximation of the overall performance. The parameter extraction from shunted devices will be discussed in Section 5.5. The measurement techniques involved are dark *I-V* and EL under different forward current bias levels. The method firstly utilises a hybrid fitting algorithm [202] to extract parameters I_{sat}, n and R_{sh} from the dark *I-V* curve. Secondly it searches for the optimum R_s^i-$R_{\blacksquare}$ pair that generates the minimum relative mean-square deviation (RMSD) [203] between the

simulated and measured EL images under various bias conditions, as well as the dark *I-V* curve simultaneously. The dark *I-V* is chosen to eliminate the possible influences of nonlinear I_{ph} in e.g. a-Si devices, as explained in [45]. The flowchart of the method is illustrated in Figure 5.5.

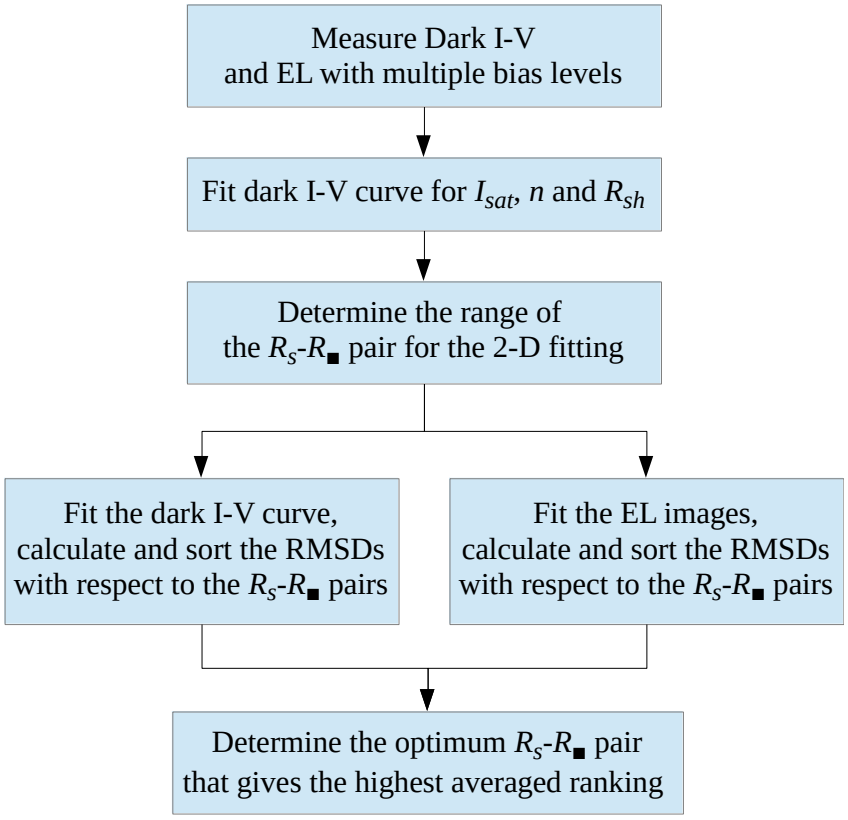

Figure 5.5. Flowchart shows the newly developed method for the parameter extraction of the full 2-D SRM of a non-shunted thin-film PV device. A dark *I-V* curve and EL images taken with varying forward current bias levels are used for 2-D fitting.

Both simulations and experiments (Section 5.4) are used to verify this method. PVONA-based 2-D simulations are setup in a virtual experiment for a virtual cell with the input parameters listed in Table 5.1. A 2-D SRM for a virtual 5.2 cm × 0.5 cm TF cell is configured using a 104 × 10 meshing grid, with the spatial resolution 0.05 cm × 0.05 cm. The local parameters are correlated by Equation (4.6)-(4.15). The lateral resistances of the back contact are neglected, as discussed in Section 3.2. As described in Section 5.2.3, the PVONA tool provides programming interfaces for introducing external environmental conditions (irradiance and electrical biases) and for obtaining localised operating points, through which the measurement techniques

i.e. dark *I-V* and EL can be simulated,. The interpretation from the local junction voltage to the EL intensity is based on Equation (5.11).

Table 5.1
Electrical parameters of the single-diode model for a 5.2 cm × 0.5 cm thin-film cell

	Inputs	**Extracted**	
J_{sat}	1.0×10^{-10} A/cm^2	1.03×10^{-10} A/cm^2	Hybrid fitting
n	2.0	2.00	
Γ_{sh}	5.30×10^{5} Ω·cm^2	5.73×10^{5} Ω·cm^2	
Γ_s^i	8.0 Ω·cm^2	8.04 Ω·cm^2	2-D fitting
$R_{\blacksquare}$	12.0 Ω/□	11.98 Ω/□	

5.3.3 Global parameters extraction

The dark *I-V* characteristic of a PV device based on the single-diode model is described by Equation (5.13), by setting the photocurrent generation I_{ph} in Equation (2.5) to 0. Here, the single-diode model is used for demonstration, while the methods can be easily adjusted to be applied to other type of equivalent models listed in Section 2.3.

$$I = I_{sat}\left\{\exp\left[\frac{q(V-IR_s)}{nkT}\right]-1\right\}+\frac{V-IR_s}{R_{sh}} \tag{5.13}$$

Section 4.4 explained that the fitting of the single-diode model for global electrical parameters can be carried out using a hybrid algorithm developed by Gottschalg *et al*. [202], in which the undetermined variables are grouped into a nonlinear and a linear sub-set, being iteratively treated by the Nelder-Mead (NM) simplex and singular value decomposition (SVD) respectively.

Similarly, the fitting of the dark *I-V* characteristics can utilise the hybrid algorithm as well, in which n and R_s are in a nonlinear space, making Equation (5.13) a linear equation with respect to I_{sat} and R_{sh}. The fitting process is formulated by means of an overdetermined linear equation system (the number of equations is greater than the number of unknown variables) as expressed by Equation (5.14).

$$\left[\exp\left(\frac{q(\boldsymbol{V}-\boldsymbol{I}R_s)}{nkT}\right)-1 \quad \boldsymbol{V}-\boldsymbol{I}R_s\right]\begin{bmatrix} I_{sat} \\ 1/R_{sh}\end{bmatrix}=[\boldsymbol{I}] \tag{5.14}$$

More specifically, the iterative hybrid algorithm implements a two-variable NM searching loop to update the nonlinear space (n, R_s), which thus overwrites the coefficient matrix in each iterative sequence. The overdetermined linear equation system can then be fitted by the SVD with respect to the linear space (I_{sat}, R_{sh}). These four parameters are then fed into Equation (5.13) to calculate a new dark *I*-*V* curve. The loop is repeated until a very small RMSD e.g. 10^{-8} A is achieved between the measured and the updated calculated curves.

The global I_{sat}, R_{sh} and n values are then corrected with respect to the dimension of the sub-cell mesh grid following Equation (4.6)-(4.15). The extracted parameters of the virtual cell are marked in Table 5.1. The J_{sat} and Γ_{sh} show 3% and 8% variations respectively compared with the input values. However, the distortion of the dark *I*-*V* curve is negligible and, as will be shown in the following sections, the full parameter set extracted shows excellent agreement to the inputs.

5.3.4 Determination for series resistances

After $I_{sat}(\boldsymbol{r})$, $R_{sh}(\boldsymbol{r})$ and $n(\boldsymbol{r})$ are determined, a 2-D fitting procedure is carried out in the (R_s^i, $R_{\blacksquare}$) space to search the optimum R_s^i-$R_{\blacksquare}$ pair. This can be done with a two-variable NM simplex algorithm [160]. A stepping-through approach is used to demonstrate the distribution of RMSD values in the (R_s^i, $R_{\blacksquare}$) space. The range of the R_s^i, i.e. 0 Ω·cm² - 15.0 Ω·cm², and of $R_{\blacksquare}$, i.e. 5.0 Ω/□ - 20.0 Ω/□, are empirically chosen. The step widths are 0.5 Ω·cm² and 0.5 Ω/□ respectively.

The fitting results for the dark *I*-*V* and the RMSD map are shown in Figure 5.6. The examples demonstrated in Figure 5.6a show that the varying (R_s^i, $R_{\blacksquare}$) combination mainly changes the global R_s of the cell, which can be read from the shapes of the dark *I*-*V* curves. Here, the best fit gives R_s^i = 8.04 Ω·cm² and $R_{\blacksquare}$ = 11.98 Ω/□. The "low R_s" (R_s^i = 0.0 Ω·cm², $R_{\blacksquare}$ = 5.0 Ω/□) and the "high R_s" (R_s^i = 15.0 Ω·cm², $R_{\blacksquare}$ = 20.0 Ω/□) cases are provided for comparison. It is important to note that there is a many-to-one relationship i.e. multiple combinations can result in very close RMSD values (the banding shown in Figure 5.6b), implying that a sole *I*-*V* fitting is insufficient for parameter extraction.

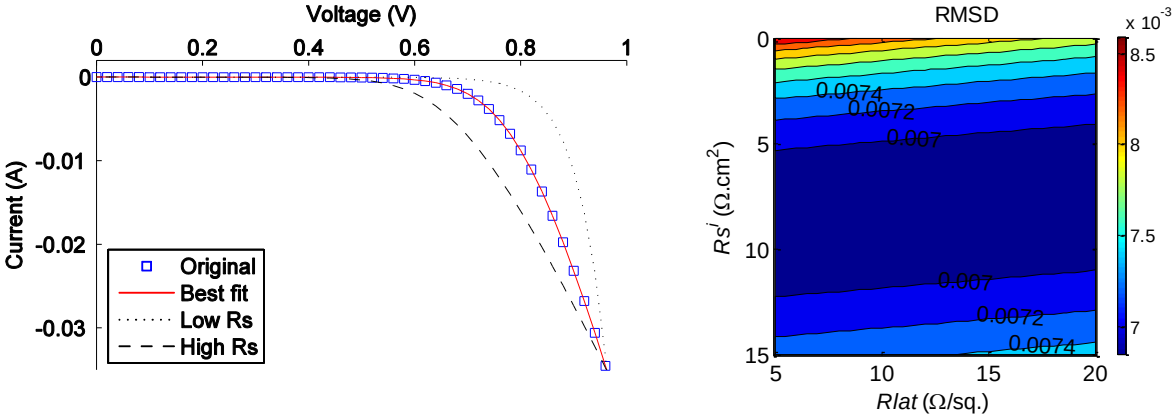

(a) (b)

Figure 5.6. (a) Fitting results and (b) RMSD map of the simulated dark *I-V* curve fitting for the (R_s^i, $R_{\blacksquare}$) set. The best final result is highlighted and demonstrates excellent agreement to the original data. The banding in the RMSD map indicates a many-to-one relationship between the (R_s^i, $R_{\blacksquare}$) sets and the overall R_s effects in the dark *I-V*.

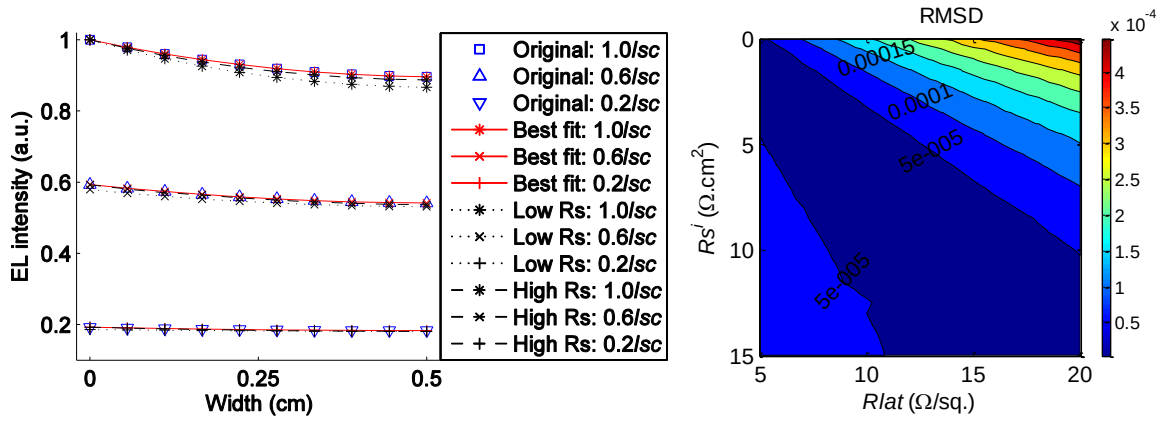

(a) (b)

Figure 5.7. (a) Fitting results (line-plot) and (b) RMSD map of the simulated 2-D EL fitting for the (R_s^i, $R_{\blacksquare}$) set. The best final result is highlighted and demonstrates excellent agreement to the original data. The banding in the RMSD map indicates a many-to-one relationship between the (R_s^i, $R_{\blacksquare}$) sets and the lateral variations in EL images.

Three EL images, with the external forward current bias at short-circuit current (I_{SC}), $0.6I_{SC}$ and $0.2I_{SC}$, respectively were simultaneously utilised for R_s^i-$R_{\blacksquare}$ fitting. In EL imaging, higher forward bias level requires shorter imaging time than lower bias levels. However, EL measurements with low current bias are necessary since some defects e.g. shunts are sensitive to the injection level [57], and are therefore helpful to identify a non-shunted reference cell. Similarly, the EL fitting also reveals a banding as shown in Figure 5.7b. This means a sole EL fitting is also insufficient for determining the (R_s^i, $R_{\blacksquare}$) set. The two bandings in the RMSD maps of dark *I*-*V* and EL fitting intersect the best (R_s^i, $R_{\blacksquare}$) set, i.e. R_s^i = 8.0 Ω·cm^2 and $R_{\blacksquare}$ = 12.0 Ω/□, which perfectly matches the data given in Table 5.1. The dark *I*-*V* curve and the line-plot EL profiles using these parameters are compared with the original data in Figure 5.6a and Figure 5.7a. with excellent agreement.

5.4 Experimental verification

5.4.1 Sample and experimental setup

The sample used for experimental demonstration is a TF a-Si module consisting of 9 cells connected in series, as shown in Figure 5.8. The EL images taken at different bias levels, i.e. I_{SC}, $0.6I_{SC}$ and $0.2I_{SC}$, are provided, where I_{SC} is the short-circuit current of the sample measured under STC. There are no flaws detected, thus the sample is suitable to be used as a reference.

The dark *I*-*V* of the module is measured from 0A to $-I_{SC}$ at room temperature. The dark *I*-*V* of a single cell is obtained by dividing the operating voltages of the module by 9, assuming all cells in the module perform identically, while the corresponding operating current values remain unchanged. The EL images were taken with an integration time of 10 minutes at room temperature. Three measurements were taken at each bias condition and averaged to reduce noise from the camera. The active imaging area is about 1200 × 1200 pixels, in which a single cell occupies about 1040 × 100 pixels. The size of a single cell is 5.2 cm × 0.5 cm. A 1040 × 100 meshing grid i.e. 50 μm × 50 μm spatial resolution is configured for 2-D fitting.

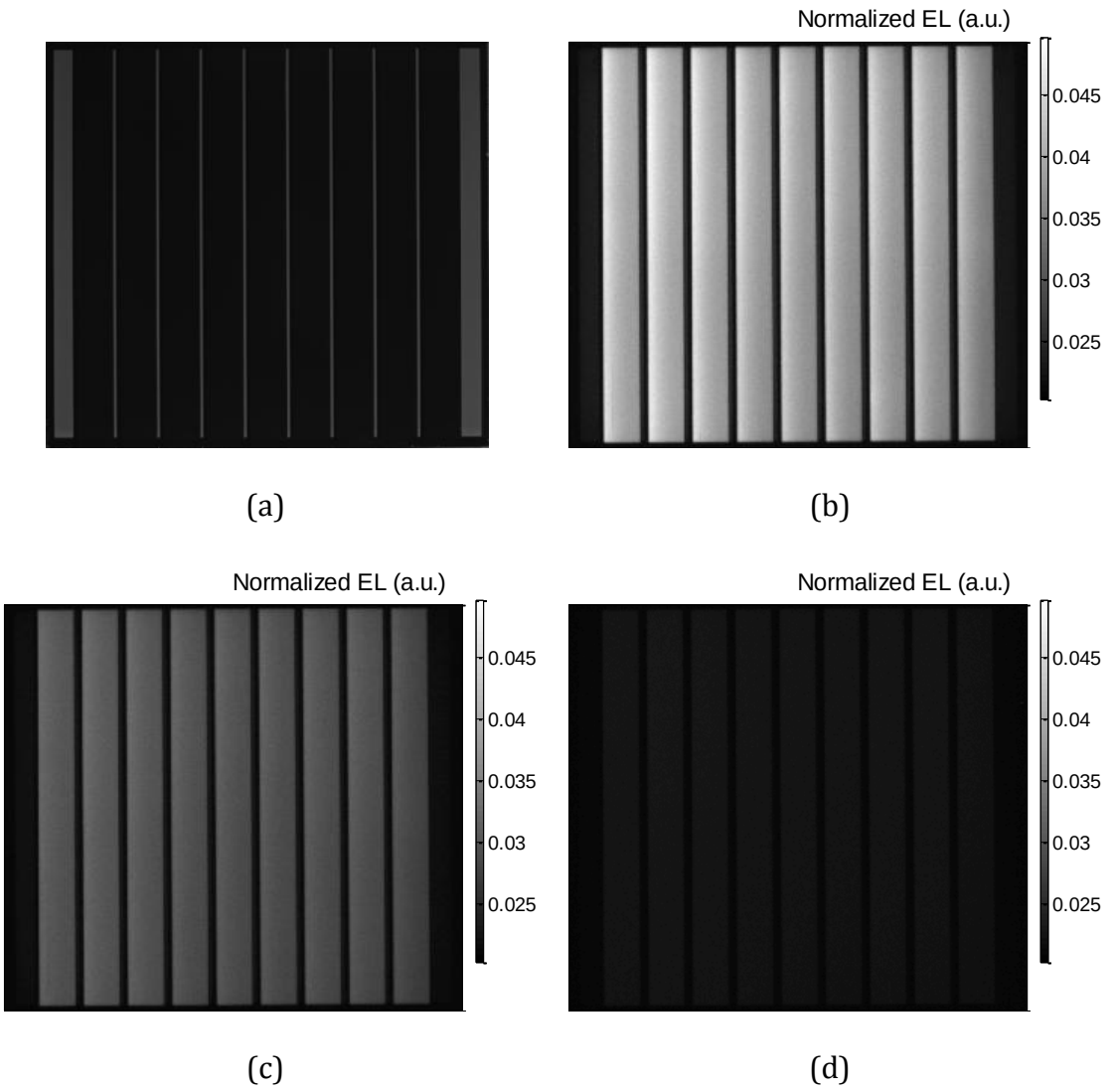

Figure 5.8. (a) A photo of the 9-cell thin-film a-Si module used as the reference sample; and EL images of the sample taken at current bias levels (b) $1.0I_{SC}$, (c) $0.6I_{SC}$, and (d) $0.2I_{SC}$. No flaws are detected visibly.

5.4.2 Results and discussion

The extracted parameters using the proposed method are listed in Table 5.2. The parameters obtained by the hybrid fitting were adjusted according to the resolution to fit the sub-cells by Equations (4.6)-(4.15). The dark *I*-*V* curve and the line-plotted EL profile generated by the optimum parameter set are highlighted and compared with the original experiment data in Figure 5.9a and Figure 5.10a. The jitters seen in the EL profile are most likely due to the read out noise of the camera rather than the

defects. These are averaged out by applying a 3 × 3 median filter[5], as introduced in Section 5.2.1. The best combination R_s^i = 1.97 Ω.cm^2 and $R_{\blacksquare}$ = 14.86 Ω/□ provides the best fit to both dark *I*-*V* and the multiple EL profiles.

The diode ideality factor extracted by the hybrid *I*-*V* fitting algorithm gives n = 3.82, which is out of the range $1 < n < 2$ and thus does not have physical meaning, as discussed in [40]. This can be due to the mismatch effects between cells, which slightly reshape the resultant dark *I*-*V* characteristic in the knee area and thus result in a larger n. However, since it produces an appropriate mathematical fitting based on the singe-diode model, the value is still considered reasonable, as also discussed in [39]. Additionally, the single-diode model can cause misinterpretation of the behaviour of drift-driven devices as such as a-Si TF solar cells [45]. The validity of other model types e.g. double-diode have been studied in [46] and reviewed in Section 2.3. These derivatives can be combined with this approach for more accurate results.

This method can be adjusted for characterising wafer-based c-Si devices as well. However, the material properties e.g. grain boundaries can be difficult to be represented in a diode model and thus can bring uncertainties in the fitting process. In addition, the 2-D model of a c-Si cell can be a large array of more than 1000 × 1000 sub-cells to match the geometry of the metal contact grid i.e. busbars and fingers. Therefore the solving of SRMs and thus the fitting can be time-consuming. Hence, methods for characterising c-Si devices require further investigations in terms of accelerating the 2-D simulation solver by e.g. applying fragmentization or variable meshing [148] and of material properties at e.g. grain boundaries.

Table 5.2
Extracted electrical parameters of a 9-cell a-Si thin-film module

J_{sat}	3.35×10^{-9} A/cm^2	Hybrid fitting
n	3.82	
Γ_{sh}	684.96 Ω.cm^2	
Γ_s^i	1.97 Ω.cm^2	2-D fitting
$R_{\blacksquare}$	14.89 Ω/□	

[5] This is done in Matlab with the *medfilt2* function.

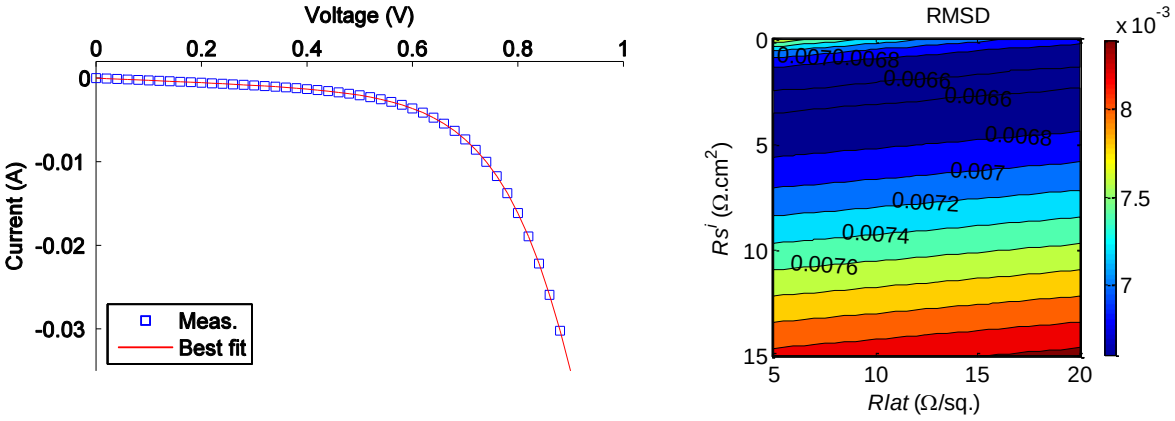

(a) (b)

Figure 5.9. (a) Fitting results and (b) RMSD map of the dark *I-V* curve fitting for the (R_s^i, $R_{\blacksquare}$) set. The best final result is highlighted and demonstrates excellent agreement to the measurement result.

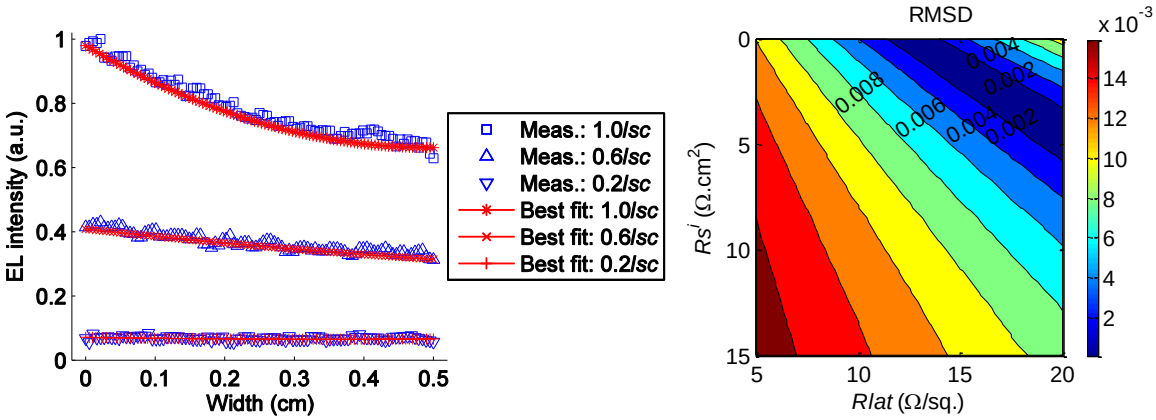

(a) (b)

Figure 5.10. (a) Fitting results and (b) RMSD map of the 2-D EL fitting for the (R_s^i, $R_{\blacksquare}$) set. The best final result is highlighted and demonstrates excellent agreement to the measurement results.

5.5 Application of the method: quantification of local shunts

5.5.1 Shunts in EL images

Local shunt is a common type of defect that can be found in thin-film PV devices, which is normally introduced during manufacturing or in the aging processes. A local shunt is a low resistance current pathway i.e. with low $R_s^i(\boldsymbol{r})$ and low $R_{sh}(\boldsymbol{r})$. As

detailed in Section 2.4, this can alter the local *I-V* characteristic and thus result in mismatch effects in the surrounding region. A shunt bypasses current that is supposed to flow through the local junction and thus acts as a current sink that extracts current from the surrounding sub-cells. This can also cause a drop in the local V_j. Consequently, the amount of current flowing through the junctions is reduced, resulting in the reduction of local radiative recombination and thus EL intensity. Therefore, a shunt appears in EL images normally as a dark spot with a circular blurred region.

The appearance of a shunt in EL images can be affected by various factors such as (i) its location, (ii) its strength, (iii) lateral resistances of the contact layer, and (iv) intensity of the forward bias, etc. Figure 5.11 demonstrates the influences of the above conditions on EL profiles by simulated EL images using PVONA-based SRMs. 60 × 18 SRMs are configured with parameters listed in Table 4.4 unless otherwise specified. A pin-hole shunt is introduced at the sub-cell (30, 1), (30, 9) and (30, 18) respectively. The strength of the shunt is defined as R_s^i = 0.05 Ω·cm^2 and R_{sh} = 0.15 Ω·cm^2. A forward current bias equivalent to the I_{SC} at STC is applied. The size of the shunt is for demonstration only, in order to show the effects of shunts.

Sub-figures (a)(b)(c) in Figure 5.11 show that a shunt can introduce a blurred region of which the shape and the size depends on the location. More specifically, a shunt at a longer distance away from the positive terminal in the SRM can be affected to a large degree by the lateral resistances and thus voltage drops compared to a closer one. The exponential relationship between EL intensity and junction voltage [Equation (5.11)] makes the local EL emission sensitive to variations in the voltage distribution established by the shunt.

To investigate the effects of the strength of the shunts, simulation results with R_s^i = 0.05 Ω·cm^2 and R_{sh} = 0.05 Ω·cm^2 are demonstrated in sub-figures (d)(e)(f). The reduction in the overall EL intensity is evident since the stronger shunt results in more current bypassed through the low resistivity pathway (i.e. directly from the front contact to the back without flowing through the junction) and thus the amount of charge carriers remaining for radiative recombination in the device becomes less.

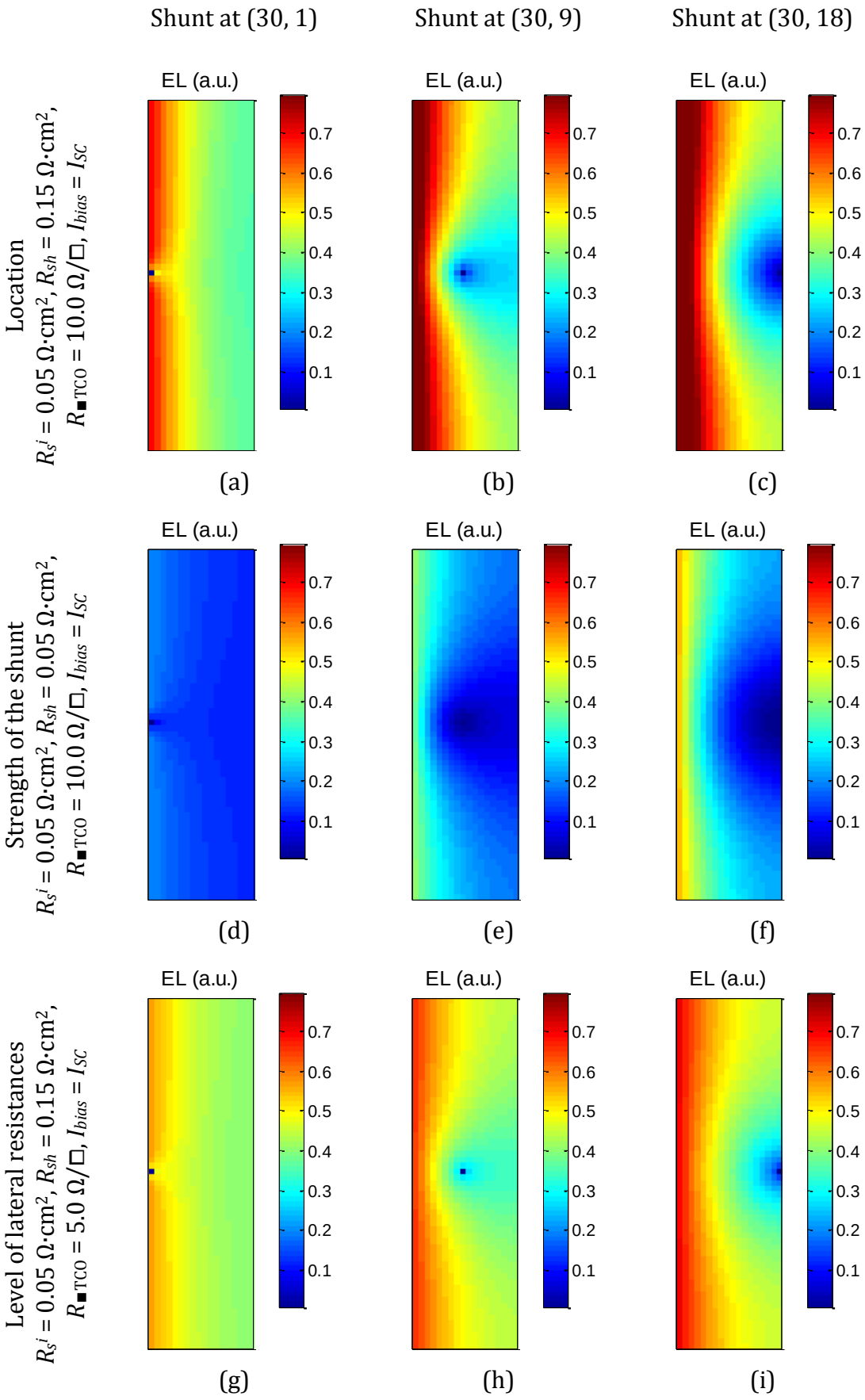
Shunt at (30, 1)
Shunt at (30, 9)
Shunt at (30, 18)
Location
R_s^i = 0.05 Ω·cm², R_{sh} = 0.15 Ω·cm²,
$R_{\blacksquare TCO}$ = 10.0 Ω/□, I_{bias} = I_{SC}
Strength of the shunt
R_s^i = 0.05 Ω·cm², R_{sh} = 0.05 Ω·cm²,
$R_{\blacksquare TCO}$ = 10.0 Ω/□, I_{bias} = I_{SC}
Level of lateral resistances
R_s^i = 0.05 Ω·cm², R_{sh} = 0.15 Ω·cm²,
$R_{\blacksquare TCO}$ = 5.0 Ω/□, I_{bias} = I_{SC}
EL (a.u.)
0.7
0.6
0.5
0.4
0.3
0.2
0.1
(a)
(b)
(c)
(d)
(e)
(f)
(g)
(h)
(i)

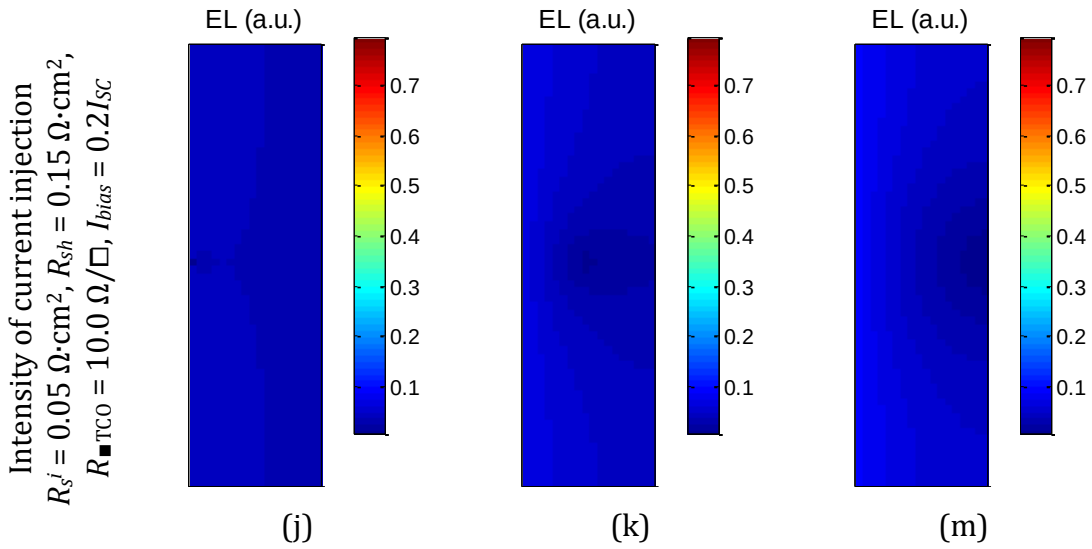

Figure 5.11. Simulated 60 × 18 EL profiles reveal the influences of various factors including location, strength, lateral resistances of the contact layer and intensity of the forward bias on the appearance of shunts in EL images. All images use the same arbitrary scale to highlight relative variations.

The impacts of lateral resistances on the shunted region are also evident. A lower lateral resistance $R_{\blacksquare}$ = 5.0 Ω/□ is configured in the SRM. It is clear that in sub-figures (g)(h)(i), that the size of the blurred areas significantly decrease compared with the original cases with $R_{\blacksquare}$ = 10.0 Ω/□. This is because the lower lateral resistance weakens mismatch effects among sub-cells and therefore less current is extracted from the surrounding area, and vice versa.

The strength of the forward bias determines the amount of charge carriers injected into the sample. A lower level of injection leads to a lower level of overall EL intensity and therefore longer integration time may be required to obtain clear EL images. A shunt tends to be more sensitive to lower bias levels because the conductance of the junction exponentially increases with the increasing junction voltage, which thus reduces the relative influences of the shunt in its surrounding region [57], as shown in sub-figures (j)(k)(m).

Figure 5.11 shows clear area effects of shunts. Shunts with different features have different appearances in EL images. However, the changes can not yet be described by analytical expressions as they contain mixed influences of the factors

demonstrated above. Instead, numerical fitting-based approaches become effective in this case. By applying properly designed iterative algorithms, quantification of local shunts can be achieved by tuning localised parameters, which results in an agreement between the simulation and measurement results, i.e. EL images.

5.5.2 Quantification of local shunts with EL

As discussed in Section 5.3, the parameters extracted from the reference sample can be used as initial values for further analysis of defects. This assumption is valid for the samples with the same type of material, especially for those produced in the same batch. This case study investigates the analyses of two local pin-hole shunts in an a-Si module of the same type shown in Figure 5.8a. To achieve this, EL images at different bias levels i.e. I_{SC} and $0.2I_{SC}$ are taken to identify and locate shunts, as shown in Figure 5.12. This was done by searching the pixel with the lowest EL intensity.

The shunt analysis is carried out by an iterative procedure that searches the best parameters that reproduce the EL measurement results. It is important to specify that the method presented here is developed only in the device's view rather than the region's view. For example, a spot in the blurred surrounding area of a local shunt appears darker than the ones far away from the area in an EL image. This is because the shunt attracts current from this area, which does not mean the spot itself contains a defect. As depicted in [109], the actual diameter of a shunt can be only a few micrometres and thus can be smaller than a pixel of an EL image. Therefore the extracted local (R_s^i, R_{sh}) set essentially represents the "averaged effects" of the shunt in the particular local region, which approximates the measured EL profiles best.

In the iterative fitting, a 208 × 20 SRM of the cell is configured using the parameters extracted from the reference sample, as listed in Table 5.2. The reduced resolution of the SRM can firstly eliminate some measurement noise by dividing the original EL images into 5 × 5 pixel blocks and calculating the average; and secondly accelerate the fitting process. The hotspot heating is neglected in this method. A two-variable NM simplex algorithm [159] is developed to allow an efficient searching and fitting process for the (R_s^i, R_{sh}) set.

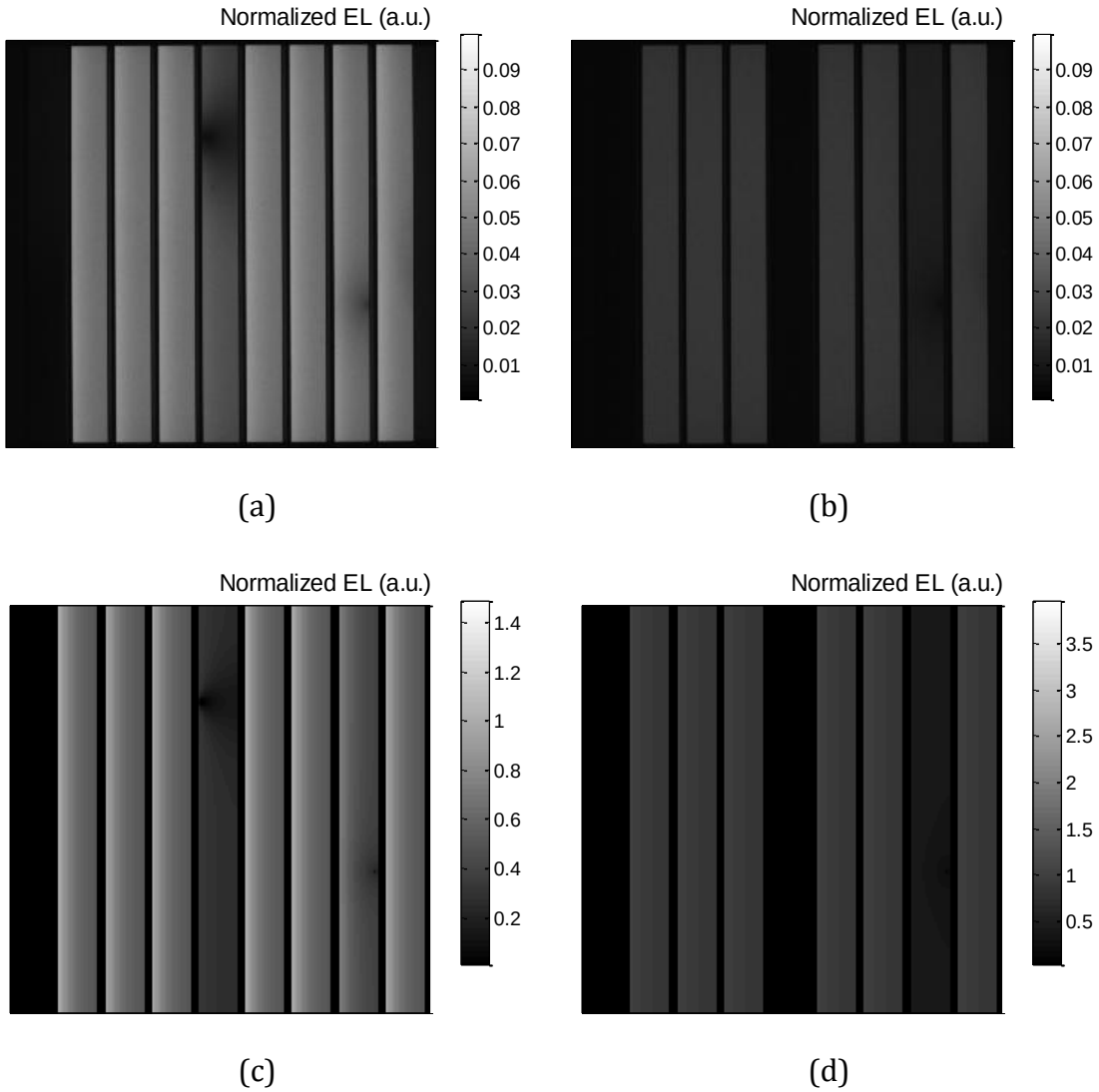

Figure 5.12. Measured EL images of the module at bias level (a) I_{SC} and (b) $0.2I_{SC}$; and reconstructed EL images using the extracted parameters at bias level (c) I_{SC} and (d) $0.2I_{SC}$. Excellent agreement is shown between the measurement and simulation results.

From Figure 5.12a and Figure 5.12b it is visible that the module tested has two shunts, one in the 5th cell [location (50, 2)] and one in the 8th cell [location (136, 19)]. The 1st cell is completely inactive. The NM fitting for the two know shunts in the 5th and the 8th cell starts with 3 random initial parameter sets of (R_s^i, R_{sh}). The NM algorithm stops at (6.25×10^{-4} Ω·cm^2, 2.56×10^{-2} Ω/□) and (0.02 Ω·cm^2, 0.69 Ω/□) for the 5th and the 8th cell respectively. The reconstructed EL images under I_{SC} and $0.2I_{SC}$ are shown in Figure 5.12c and Figure 5.12d. An excellent agreement is shown between the measured and simulated EL images. For a better demonstration, the EL line-plots of the shunt in the two cells are provided in Figure 5.13 to show the

agreement. Different scales shown in Figure 5.12c and d were used to compensate the different calibration factor in Equation (5.11) for different bias conditions.

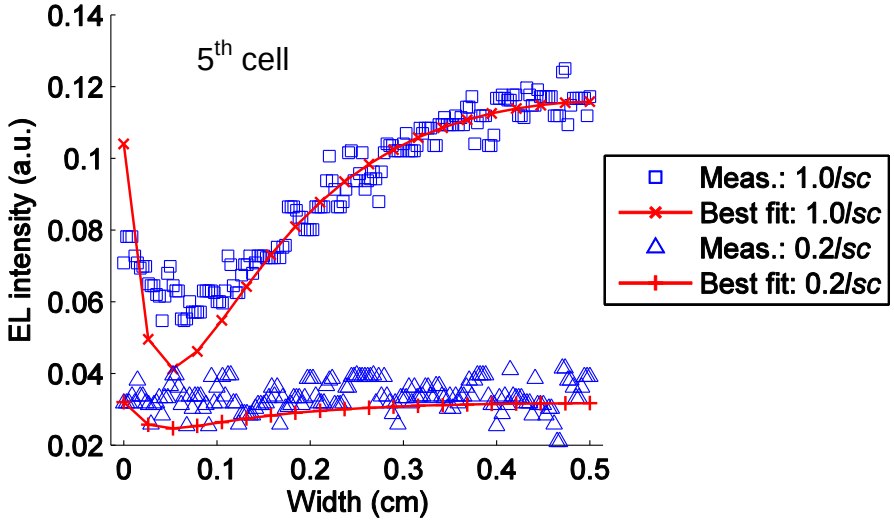

(a)

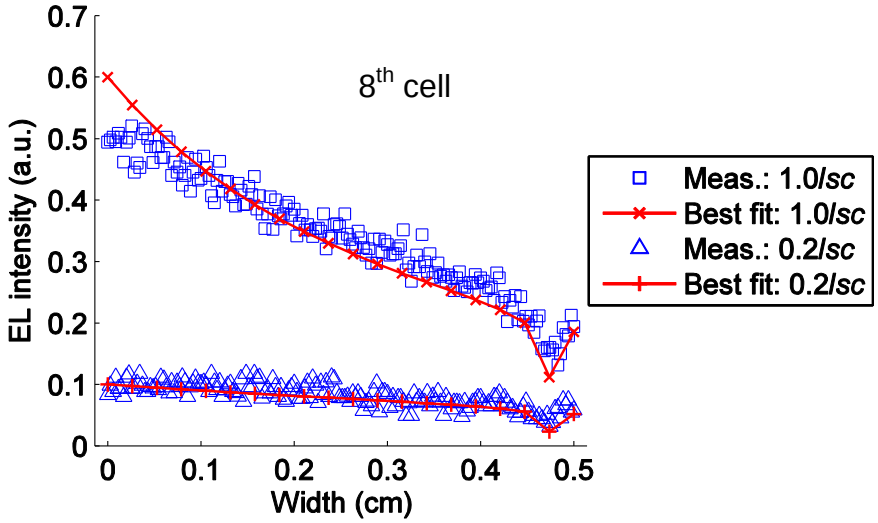

(b)

Figure 5.13. Line-plots show the agreement between the measured and the simulated EL profiles in (a) the 5th cell and (b) the 8th cell. EL measurements were taken at bias level I_{SC} and $0.2I_{SC}$.

5.6 Chapter conclusions

The majority of electrical parameter extraction methods of PV devices are based on lumped or 1-D modelling and fitting technique. This does not allow investigations of spatial effects. However, the lateral variants in TF devices require spatially-resolved approaches for better representations of e.g. local series resistance effects and local shunts. In this chapter, a new method for quantitative determination of localised electrical parameters of TF PV devices based on 2-D fitting of dark *I*-*V* characteristics and EL images has been developed and verified.

This method utilises a hybrid fitting algorithm to extract global I_{sat}, R_{sh} and n from the dark *I*-*V* curve as initial values, and implements 2-D fittings with a fast simulation tool i.e. PVONA to search the optimum combination of R_s^i and $R_{\blacksquare}$ that provides the best fit to the EL images and the overall dark *I*-*V* curve simultaneously. This method has been verified using PVONA-based simulations by accurately extracting the parameters that match the inputs of a virtual cell. The experimental validation using an a-Si module showed that the method can not only separate the lateral resistance effects from intrinsic series resistances, but can also help quantifying effects of local shunts.

A case study showed that two pin-hole-like shunts detected by EL images were accurately reconstructed by a fitting algorithm. An SRM with a lower resolution than the EL images were applied to accelerate the fitting processes. This allows the description of shunt effects in a relatively short time and thus can be utilised in e.g. a production line for spatially-resolved quality assessment with the initial values available from reference samples. To further extend this approach for independent characterisation (i.e. without reference values), a multi-dimensional searching method such as a variable NM simplex algorithm can be developed to implement the extraction for the full parameter set.

For more detailed studies of device properties, for example the size and the nature of a shunt, SRMs can be used to produce simulations with various resolution, or various number of shunted sub-cells for further investigation. Moreover, for the flaws of other types or shapes, the method is still applicable by employing e.g. multi-variable

NM algorithm, although the efficiency and convergence of the searching and fitting method should be examined carefully to prevent disturbances such as local minima.

It is also notable that the macroscopic view of this method can be a limitation. For this reason, parameter determination based on e.g. localised *I-V* fitting can be potentially useful for evaluating the behaviour of not only whole devices but also small defective regions.

The method demonstrated the possibility of utilising SRMs to describe the localised behaviour in PV devices, which may be applied to provide improved means of quality control in a production environment with respect to design parameters, or to evaluate e.g. degradation in devices for e.g. prediction of energy yield for finished products.

Chapter 6

Conclusions

This work develops and implements a spatially-resolved simulation tool to describe PV devices. It allows the evaluation of spatial inhomogeneities in not only a global but also a local fashion. This can be achieved by employing existing spatially-resolved modelling and quantitative characterisation techniques. However, existing approaches tend to be sub-optimal and the developed toolset improves on these methods in terms of the efficiency of computation, and thus makes quantitative characterisation in a high resolution that is equivalent to an EL image possible. A spatially-resolved modelling and characterisation framework has been established utilising the outcomes of this project, as a complementary tool to global *I-V* characterisation to analyse different factors affecting device performance in PV systems.

The development of PVONA allows high resolution evaluation of localised electrical properties in PV devices. The PVONA toolset utilised a specifically designed sparse data structure to organise the SRM. Compared with nodal analysis solvers e.g. in SPICE for general circuit simulations, the SRM structure of PV cells is with a fixed interconnection topology. The dedicated sparse data structure is thus optimised with respect to this feature by recording only substantial interconnected sub-cells and by treating the local diode model as an entire entity rather than a collection of individual circuit elements. These resulted in 50% fewer nodes and 43% fewer circuit elements than those required by standard SPICE tools. This allows high resolution (e.g. a 1000 × 1000 SRM which is equivalent to a mega-pixel EL image) simulations to run on economic hardware e.g. normal desktop PCs.

The PVONA-based simulations have been approved valid to achieve quantitative analysis in various tasks. The case study of CPV showed the application of a joint optical-electrical modelling and simulation approach to achieve analysis of effects of non-uniform illumination profiles. By taking the ray-traced irradiance profiles from the optical model as environmental inputs, the PVONA tools can calculate the global and local operating points. By using this joint modelling and simulation framework, the effects of inhomogeneities are revealed by maps of local operating points and overall *I-V* characteristics.

The joint modelling framework in the case study showed that the nonuniformity of illumination can have evident impacts on the global *I-V* characteristics of devices in terms of the R_s and R_{sh} effects, and thus the P_{MPP} and the conversion efficiency. The uncertainty-affected irradiance profiles alter the global *I-V* characteristic and the MPP in both directions, although these uncertainties are from the tolerance of manufacturing and system assembly. For example, a 1.5% difference in the central thickness of a plano-convex lens led to a 5% reduction in the MPP; and a 3% increase in the MPP was found with an imperfectly mounted Fresnel lens. A sensitivity analysis showed that the variations depend on lateral resistance effects, and that case-by-case investigations should be carried out for understanding the performance of various types of systems with different types of inhomogeneities.

Simulation results suggest that the significant changes in *I-V* characteristics can be due to a mixed effect of both design parameters of the devices and the inhomogeneous irradiance. An improper design of a CPV unit can cause electrical power losses due to various mechanisms such as high R_s and R_{sh} issues. These can be investigated by not only global behaviour but also voltage and current maps, from which the localised power dissipations are clearly demonstrated. This evaluation method can be extended to normal PV systems for detailed analysis of e.g. loss mechanisms.

This approach shows the potential of the PVONA tools in various aspects. Firstly, the environmental interface can be used to combine not only optical but also thermal models to study e.g. hot spot effects in devices. This can be achieved by involving a distributed thermal (temperature) profile as an input of the SRM. The local temperature is fed into of a single sub-cell by Equation (2.5), and the trend of the effects of varying temperature on the local *I-V* characteristics is demonstrated in Figure 2.15.

Secondly, the PVONA-based simulation can assist optimisation of the performance of CPV units in terms of selecting optical components and PV devices by modelling and quantifying the potential loss mechanisms. The losses can be assessed by the changing performance indicators in the global *I-V* curves, as well as local operating points. This can also be utilised in normal PV systems with non-uniform irradiance

profiles, e.g. with partial shading. By considering the mismatch losses between individual devices, this framework is useful for e.g. prediction of system performance under varying weather conditions in long-term operations.

Thirdly, cell designers may benefit from spatially-resolved simulations by investigating the impacts of varying design parameters including the thickness of the semiconductor layers, doping concentration, pattern of the contact grid, etc. These require a one-to-one relationship between such design parameters and local electrical parameters of the diode model. This approach can provide valuable information about the global and localised behaviour of a PV device to the optimisation in the research and development stages.

The consideration of lateral resistances allows PVONA-based SRMs to quantitatively reconstruct full-size EL images. To date, the majority of electrical parameter extraction methods of PV devices are based on lumped or 1-D modelling and fitting technique. This does not allow investigations of spatial effects. By utilising the PVONA tools, one-to-one links have been established between an EL image and an SRM with the same resolution. This allows pixellation of localised electrical properties, which helps detailed investigation and development of spatially-resolved characterisation methods. A new method for quantitative determination of localised electrical parameters of TF PV devices based on 2-D fitting of dark *I*-*V* characteristics and EL images has been developed and verified. The experimental validation using an a-Si module showed that the method can not only separate the lateral resistance effects from intrinsic series resistances, but can also help quantifying effects of local shunts.

This approach managed to separate lateral resistances and thus avoided commonly used over-simplifications e.g. lumped effective series resistance. The capability of producing localised electrical parameters of various fault mechanisms enables the information from qualitative characterisation techniques e.g. EL can be further utilised for more detailed description of device properties.

As an example, a case study showed that two pin-hole-like shunts detected by EL images were accurately reconstructed by the fitting algorithm developed. An SRM with a lower resolution than the EL images were applied to accelerate the fitting

processes. This allows the description of shunt effects in a relatively short time and thus can be utilised in e.g. a production line for spatially-resolved quality assessment with the initial values available from reference samples.

To further generalise this approach for independent characterisations, a multi-dimensional searching and fitting method such as a variable NM simplex algorithm can be developed to implement the parameter extraction. For the flaws of other types or shapes, the method is still applicable by employing e.g. multi-variable NM algorithm. The requirement of a reference device should be discarded in further development to enable a more robust analysis method. This can be potentially achieved by iteratively fitting local parameters directly from multiple EL images or localised *I*-*V* characteristics. It is useful for evaluating the behaviour of not only whole devices but also small defective regions, which can provide valuable information to design and manufacturing processes.

As to the PVONA toolset itself, attempts can be made to further optimise it. Although the current PVONA version has achieved improvements in terms of computation efficiency than PSpice and LTSpice, there is still a gap to fill to enable it to be applied in a production environment for real-time calculations. This is possible by upgrading to a dedicated GPU and higher power CPUs. A pre-conditioned CG algorithm may result in faster convergence for solving linearised nodal equation systems. A dynamic variable meshing strategy can also accelerate the computational process and, additionally, can be useful to configure PV devices with complex grid patterns of the metal contact.

In short, the PVONA tools and the new parameter extraction method described in this thesis achieved significant steps forward towards fast spatially-resolved modelling and simulation and quantitative investigation of localised electrical properties in PV devices. With certain optimisation work, they can be used to support a wide range of investigations in the whole lifecycle of PV products, from the design and testing of cells in the laboratory or the production line to the performance analyses of the whole PV module arrays in the field.

Appendix A

A.1 PVONA Infrastructures – struct definitions

```
// definition of a "cell"
typedef struct aCell
{
      int n_mySubRows;  // number of rows of the sub-cell array
      int n_mySubCols;  // number of columns of the sub-cell array
      int n_myNodes;    // number of nodes
      double myVoltage; // terminal (global) voltage of the cell
      double myCurrent; // global current of the cell
      struct_aSubcell** ptr_ptr_mySubcells; // array of sub-cells
      struct_aSparseNodalSystem* ptr_myNodalSystem; // the nodal system
      struct_anIVCurve* ptr_myIVCurve; // the I-V characteristics
}struct_aCell;

// definition of a "sub-cell"
typedef struct aSubcell
{
      double myV_top;  // node voltage (top node)
      struct_aOneDiodeUnit* ptr_myOneDiodeUnit; // the local PV unit
      double myRtop_west;  // 'west' lateral resistance
      double myRtop_south; // 'south' lateral resistance
}struct_aSubcell;


// definition of a "PV unit (local single-diode model)"
typedef struct aOneDiodeUnit
{
      float G;     // local irradiance in [W/m^2]
      float TinK;  // local temperature in K
      double Iph, Isat, n, Rs, Rsh; // parameters for the diode model
      double Ieq, Geq; // intermediate parameters for linearisation
      double Vop, Iop; // local operating voltage and current
}struct_aOneDiodeUnit;

// definition of a "nodal equation system"
typedef struct aSparseNodalSystem
{
      int mySize;                // number of nodes
      struct_aNode* ptr_myNodes; // list of 'node' objects
}struct_aSparseNodalSystem;

// definition of a "node"
typedef struct aNode
{
      int myIndex;      // index of the node
      double myVoltage; // node voltage
```

```
      double myCurrent;          // current flow into the node
      int n_myConnections;       // number of neighbouring nodes
      int* ptr_myConnections;    // list of the neighbouring nodes
      int* ptr_myDirections;     // indices of the neighbouring nodes
      double* ptr_myG4Equation; // the conductance matrix G
}struct_aNode;
```

A.2 PVONA programming interfaces – function prototypes

```
// get an operating point with a voltage bias
int struct_aCell__GetOPbyV
    (struct_aCell* ptr_theCell_in, // the cell object
     double theVop_in,             // voltage bias
     const double theInitV_in      // initial value for the N-R solver
    );

// get an operating point with a current bias
int struct_aCell__GetOPbyI
    (struct_aCell* ptr_theCell_in, // the cell object
     double theIop_in,             // current bias
     const double theInitV_in      // initial value for the N-R solver
    );

// get an operating point with an ohmic load
int struct_aCell__GetOPbyR
    (struct_aCell* ptr_theCell_in, // the cell object
     double theRop_in,             // external ohmic load
     const double theInitV_in      // initial value for the N-R solver
    );

// get an I-V curve
int struct_aCell__GetIV
    (struct_aCell* ptr_theCell_in, // the cell object
     int n_theDataPoints_in        // number of the data pairs 0-V(Isc)
    );
```

A.3 Programming example

```
// a simulation task that calculates the voltage and current maps under
Vbias = 0.55V
int main(int argc, char* argv[])
{
    // create and initialise a cell
    struct_aCell* ptr_myCell = NULL;
    ptr_myCell = (struct_aCell*)malloc(sizeof(struct_aCell));
    struct_aCell__Initialize(ptr_myCell);

    // load a full configuration file
    struct_aCell__ConfigFromFile_Distrib(ptr_theCell_in);

    /*
    environmental conditions and extra defects can be configured here
    */

    // calculate the local operating points
```

```
    // Vbias = 0.55 V, the initial value Vinit = 0.8 V
    struct_aCell__GetOPbyV(ptr_theCell_in, 0.55, 0.8);

    // export the voltage and current maps to text files
    struct_aCell__SaveOP2File(ptr_theCell_in);

    // finalise and 'destroy' the cell
    struct_aCell__Finalize(ptr_myCell);
    free(ptr_myCell);
    ptr_myCell = NULL;

    return 0;
}
```

Appendix B

B.1 Program for generating configuration files

```
// configuring the SRM for Section 4.3 (99x99, 1 busbar and 10 fingers)
int main(int argc, char* argv[])
{
    // size of the model
    int nRow = 99;
    int nCol = 99;

    // geometric measures of the cell in [cm]
    double L = 1.0;
    double W = 1.0;

    // calculate the resolution
    double dL = L / (double)nRow;
    double dW = W / (double)nCol;
    double dA = dL * dW; // area of a sub-cell

    // diode parameters
    double J_ph = 0.0398;   // in [A/cm^2]
    double J_sat = 5.0e-10; // in [A/cm^2]
    double R_s = 0.03;      // in [Ohm.cm^2]
    double R_sh = 8.35e+4;  // in [Ohm.cm^2]
    double n = 1.4;

    // lateral resistances
    double R_top = 10.0;    // in [Ohm/square]
    double R_metal = 1e-6;  // in [Ohm/square]
    double R_high = 1e+10;  // in [Ohm/square]

    // prepare the configuration file
    FILE* ptr_theFullConfigFile = NULL;
    ptr_theFullConfigFile = fopen("FullConfig_CPV.txt", "w");

    fprintf(ptr_theFullConfigFile, "################################\n");
    fprintf(ptr_theFullConfigFile, "# The full configuration file #\n");
    fprintf(ptr_theFullConfigFile, "################################\n");
    fprintf(ptr_theFullConfigFile, "\n");

    // the data
    fprintf(ptr_theFullConfigFile, "# Size of the array
                                    (n_SubRows, n_SubCols)\n");
    fprintf(ptr_theFullConfigFile, "%d, %d\n", nRow, nCol);
    fprintf(ptr_theFullConfigFile, "\n");
    fprintf(ptr_theFullConfigFile, "# Full configuration\n");

    double Rtop_west, Rtop_south, Iph;
```

```
    for(int cnt_Row = 0; cnt_Row < nRow; cnt_Row++)
    {
        fprintf(ptr_theFullConfigFile,
                "# Rtop_west, Rtop_south,
                Iph, Isat, Rs, Rsh, n, G, TinC\n");

        for(int cnt_Col = 0; cnt_Col < nCol; cnt_Col++)
        {
            // the busbar
            if(cnt_Col < 2) // width of the busbar
            {
                Rtop_west = R_metal;
                Rtop_south = R_metal;
                Iph = 0.0; // sub-cell beneath is shaded
            }
            // fingers
            else if((cnt_Row % 10) == 4)//else if((cnt_Row % 28) == 0)
            {
                Rtop_west = R_metal;
                Rtop_south = R_top;
                Iph = 0.0;
            }
            else
            {
                Rtop_west = R_top;
                Rtop_south = R_top;
                Iph = J_ph * dA;
            }

            fprintf(ptr_theFullConfigFile, "# Subcell(%d, %d)\n",
                                            cnt_Row, cnt_Col);
            fprintf(ptr_theFullConfigFile,
                    "%e, %e, %e, %e, %e, %e, %e, %f, %f\n",
                    Rtop_west, Rtop_south,
                    Iph, J_sat*dA, R_s/dA, R_sh/dA, n, 1000.0, 25.0);
        }
    }

    // close file
    fprintf(ptr_theFullConfigFile, "# end");

    // clean up
    fclose(ptr_theFullConfigFile);
    ptr_theFullConfigFile = NULL;

    printf("Configuration data have been saved to file.\n");

    return 0;
}
```

B.2 Example of a configuration file of a c-Si cell

```
# a segment a the configuration file for the sample used in Section 4.3

################################
# The full configuration file #
################################
```

```
# Size of the array (n_SubRows, n_SubCols)
99, 99

# Full configuration
# Rtop_west, Rtop_south, Iph, Isat, Rs, Rsh, n, G, TinC
# Subcell(0, 0)
1.000000e-06, 1.000000e-06, 0.000000e+00, 5.101520e-14, 2.940300e+02,
8.183835e+08, 1.400000e+00, 1000.000000, 25.000000
# Subcell(0, 1)
1.000000e-06, 1.000000e-06, 0.000000e+00, 5.101520e-14, 2.940300e+02,
8.183835e+08, 1.400000e+00, 1000.000000, 25.000000
# Subcell(0, 2)
8.000000e+01, 8.000000e+01, 4.060810e-06, 5.101520e-14, 2.940300e+02,
8.183835e+08, 1.400000e+00, 1000.000000, 25.000000
# Subcell(0, 3)
8.000000e+01, 8.000000e+01, 4.060810e-06, 5.101520e-14, 2.940300e+02,
8.183835e+08, 1.400000e+00, 1000.000000, 25.000000
# Subcell(0, 4)
8.000000e+01, 8.000000e+01, 4.060810e-06, 5.101520e-14, 2.940300e+02,
8.183835e+08, 1.400000e+00, 1000.000000, 25.000000
# Subcell(0, 5)
8.000000e+01, 8.000000e+01, 4.060810e-06, 5.101520e-14, 2.940300e+02,
8.183835e+08, 1.400000e+00, 1000.000000, 25.000000
# Subcell(0, 6)
8.000000e+01, 8.000000e+01, 4.060810e-06, 5.101520e-14, 2.940300e+02,
8.183835e+08, 1.400000e+00, 1000.000000, 25.000000
# Subcell(0, 7)
8.000000e+01, 8.000000e+01, 4.060810e-06, 5.101520e-14, 2.940300e+02,
8.183835e+08, 1.400000e+00, 1000.000000, 25.000000
# Subcell(0, 8)
8.000000e+01, 8.000000e+01, 4.060810e-06, 5.101520e-14, 2.940300e+02,
8.183835e+08, 1.400000e+00, 1000.000000, 25.000000
# Subcell(0, 9)
8.000000e+01, 8.000000e+01, 4.060810e-06, 5.101520e-14, 2.940300e+02,
8.183835e+08, 1.400000e+00, 1000.000000, 25.000000
# Subcell(0, 10)
8.000000e+01, 8.000000e+01, 4.060810e-06, 5.101520e-14, 2.940300e+02,
8.183835e+08, 1.400000e+00, 1000.000000, 25.000000

…

# Subcell(98, 90)
8.000000e+01, 8.000000e+01, 4.060810e-06, 5.101520e-14, 2.940300e+02,
8.183835e+08, 1.400000e+00, 1000.000000, 25.000000
# Subcell(98, 91)
8.000000e+01, 8.000000e+01, 4.060810e-06, 5.101520e-14, 2.940300e+02,
8.183835e+08, 1.400000e+00, 1000.000000, 25.000000
# Subcell(98, 92)
8.000000e+01, 8.000000e+01, 4.060810e-06, 5.101520e-14, 2.940300e+02,
8.183835e+08, 1.400000e+00, 1000.000000, 25.000000
# Subcell(98, 93)
8.000000e+01, 8.000000e+01, 4.060810e-06, 5.101520e-14, 2.940300e+02,
8.183835e+08, 1.400000e+00, 1000.000000, 25.000000
# Subcell(98, 94)
8.000000e+01, 8.000000e+01, 4.060810e-06, 5.101520e-14, 2.940300e+02,
8.183835e+08, 1.400000e+00, 1000.000000, 25.000000
# Subcell(98, 95)
8.000000e+01, 8.000000e+01, 4.060810e-06, 5.101520e-14, 2.940300e+02,
8.183835e+08, 1.400000e+00, 1000.000000, 25.000000
# Subcell(98, 96)
```

```
8.000000e+01, 8.000000e+01, 4.060810e-06, 5.101520e-14, 2.940300e+02,
8.183835e+08, 1.400000e+00, 1000.000000, 25.000000
# Subcell(98, 97)
8.000000e+01, 8.000000e+01, 4.060810e-06, 5.101520e-14, 2.940300e+02,
8.183835e+08, 1.400000e+00, 1000.000000, 25.000000
# Subcell(98, 98)
8.000000e+01, 8.000000e+01, 4.060810e-06, 5.101520e-14, 2.940300e+02,
8.183835e+08, 1.400000e+00, 1000.000000, 25.000000

# end
```

References

[1] "Global market outlook for photovoltaics 2013-2017," European Photovoltaic Industry Association, 2013.

[2] "Global market outlook for photovoltaics 2014-2018," European Photovoltaic Industry Association, 2014.

[3] "Technology roadmap - solar photovoltaic energy," International Energy Agency, 2014.

[4] "Photovoltaics report," Fraunhofer Institute for Solar Energy Systems ISE, 2014.

[5] *NREL Chart of Best Research-Cell Efficiencies*.

[6] "IEC 60904-1 International standard: Measurement of photovoltaic current-voltage characteristics (2nd Edition)," 2006.

[7] P. Vorasayan, "Spatially-Resolved Measurement of Thin Film Silicon Solar Modules by Laser Beam Induced Current (LBIC) System ," *PhD Thesis, Loughborough University,* 2011.

[8] J. Carstensen, G. Popkirov, J. Bahr and H. Föll, "CELLO: an advanced LBIC measurement technique for solar cell local characterization ," *Solar Energy Materials & Solar Cells,* vol. 76, pp. 599-611, 2003.

[9] T. Fuyuki, H. Kondo, T. Yamazaki, Y. Takahashi and Y. Uraoka, "Photographic surveying of minority carrier diffusion length in polycrystalline silicon solar cells by electroluminescence," *Applied Physics Letters,* vol. 86, pp. 262108-1-262108-3, 2005.

[10] T. Trupke, R. A. Bardos, M. C. Schubert and W. Warta, "Photoluminescence imaging of silicon wafers," *Applied Physics Letters,* vol. 89, pp. 044107-1-044107-3, 2006.

[11] O. Breitenstein, J. P. Rakotoniaina and M. H. Al Rifai, "Quantitative Evaluation of Shunts in Solar Cells by Lock-In Thermography," *Prog. Photovolt: Res. Appl.,* vol. 11, pp. 515-526, 2003.

[12] B. E. Pieters, "Spatial modeling of thin-film solar modules using the network simulation method and SPICE," *IEEE Journal of Photovoltaics,* vol. 1, pp. 93-98, 2011.

[13] R. Gupta, P. Somasundaran and D. K. Nandi, "Electrical simulation and characterization of shunts in solar cells," *Applied Mechanics and Materials,* vol. 110-116, pp. 2453-2457, 2012.

[14] A. Zekry and A. Y. Al-Mazroo, "A distributed SPICE-model of a solar cell," *IEEE Transactions on Electron Devices,* vol. 43, pp. 691-700, 1996.

[15] K. Brecl and M. Topic, "Simulation of losses in thin-film silicon modules for different configurations and front contacts," *Progress in Photovoltaics,* vol. 16, pp. 479-488, 2008.

[16] S. Eidelloth, F. Haase and R. Brende, "Simulation tool for equivalent circuit modeling of photovoltaic devices," *IEEE Journal of Photovoltaics,* vol. 2, pp. 572-579, 2012.

[17] S. Guo, A. G. Aberle and M. Peters, "Investigating local inhomogeneity effects of silicon wafer solar cells by circuit modelling," *Energy Procedia,* vol. 33, pp. 110-117, 2013.

[18] B. Michl, M. Kasemann, J. Giesecke, M. Glatthaar, A. Schütt, J. Carstensen, H. Föll, S. Rein, W. Warta and H. Nagel, "Application of luminescence imaging based series resistance measurement methods in an industrial environment," in *23rd European Photovoltaic Solar Energy Conference,* Valencia, 2008, pp. 1175-1181.

[19] K. Ramspeck, K. Bothe, D. Hinken, B. Fischer, J. Schmidt and R. Brendel, "Recombination current and series resistance imaging of solar cells by combined luminescence and lock-in thermography," *Applied Physics Letters,* vol. 90, pp. 153502-1-153502-3, 2007.

[20] H. Kampwerth, T. Trupke, J. W. Weber and Y. Augarten, "Advanced luminescence based effective series resistance imaging of silicon solar cells," *Applied Physics Letters,* vol. 93, pp. 202102-1-202102-3, 2008.

[21] *LTspice IV*. Available: http://www.linear.com/designtools/software/#LTspice.

[22] *OrCAD EE (PSpice) Designer*. Available: http://www.orcad.com/products/orcad-ee-pspice-designer/overview.

[23] J. Nelson, *The Physics of Solar Cells.* Imperial College Press, 2003.

[24] S. R. Wenham, M. A. Green, M. E. Watt and R. Corkish, *Applied Photovoltaics.* Earthscan, 2007.

[25] *PVCDROM*. Available: http://www.pveducation.org/pvcdrom.

[26] P. Auger, "Sur les rayons β secondaires produits dans un gaz par des rayons X," *C. R. A. S.,* vol. 177, pp. 169-171, 1923.

[27] R. F. Pierret, *Semiconductor Device Fundamentals.* Addison Wesley, 1996.

[28] C. Carrero, D. Ramírez, J. Rodríguez and C. A. Platero, "Accurate and fast convergence method for parameter estimation of PV generators based on three main points of the I-V curve," *Renewable Energy,* vol. 36, pp. 2972-2977, 2011.

[29] D. L. King, W. E. Boyson and J. A. Kratochvil, "Photovoltaic array performance model," Sandia National Laboratories, Tech. Rep. SAND2004-3535, 2004.

[30] D. S. H. Chan, J. R. Phillips and J. C. H. Phang, "A comparative study of extraction methods for solar cell model parameters," *Solid-State Electronics,* vol. 29, pp. 329-337, 1986.

[31] F. Ghani and M. Duke, "Numerical determination of parasitic resistances of a solar cell using the Lambert W-function," *Solar Energy,* vol. 85, pp. 2386-2394, 2011.

[32] R. Khezzar, M. Zereg and A. Khezzar, "Comparative study of mathematical methods for parameters calculation of current-voltage characteristic of photovoltaic module," in *International Conference on Electrical and Electronics Engineering,* Bursa, 2009, pp. I24-I28.

[33] T. O. Saetre, O. -. Midtgård and G. H. Yordanov, "A new analytical solar cell I-V curve model," *Renewable Energy,* vol. 36, pp. 2171-2176, 2011.

[34] I. Martil and G. G. Diaz, "Determination of the dark and illuminated characteristic parameters of a solar cell from I-V characteristics," *European Journal of Physics,* vol. 13, pp. 193-197, 1992.

[35] A. Hovinen, "FItting of the solar cell IV-curve to the two diode model," *Physica Scripta,* vol. T54, pp. 175-176, 1994.

[36] T. Zdanowicz, "The interactive computer program to fit I-V curves of solar cells," in *12th European Photovoltaic Solar Energy Conference,* Amsterdam, 1994, pp. 1311-1314.

[37] E. Q. B. Macabebe, C. J. Sheppard and E. Ernest van Dyk, "Parameter extraction from I-V characteristics of PV devices," *Solar Energy,* vol. 85, pp. 12-18, 2011.

[38] G. L. Araujo, E. Sanchez and M. Marti, "Determination of the two-exponential solar cell equation parameters from empirical data," *Solar Cells,* vol. 5, pp. 199-204, 1982.

[39] O. Breitenstein and S. Rißland, "A two-diode model regarding the distributed series resistance," *Solar Energy Materials & Solar Cells,* vol. 110, pp. 77-86, 2013.

[40] O. Breitenstein, P. Altermatt, K. Ramspeck and A. Schenk, "The origin of ideality factors n>2 of shunts and surfaces in the dark I-V curves of si solar cells," in *21st European Photovoltaic Solar Energy Conference,* Munich, 2006, pp. 625-628.

[41] J. M. Shah, Y. -. Li, T. Gessmann and E. F. Schubert, "Experimental analysis and theoretical model for anomalously high ideality factors (n>>2) in AlGaN/GaN p-n junction diodes," *Journal of Applied Physics,* vol. 94, pp. 2627-2630, 2003.

[42] S. Steingrube, O. Breitenstein, K. Ramspeck, S. W. Glunz, A. Schenk and P. P. Altermatt, "Explanation of commonly observed shunt currents in c-Si solar cells by means of recombination statistics beyond the Shockley-Read-Hall approximation," *Journal of Applied Physics,* vol. 110, pp. 014515, 2011.

[43] Z. Wang, Z. Cheng, A. E. Delahoy and K. K. Chin, "A study of light-sensitive ideality factor and voltage-dependent carrier collection of CdTe solar cells in forward bias," *IEEE Journal of Photovoltaics,* vol. 3, pp. 843-851, 2013.

[44] J. Merten, J. M. Asensi, C. Voz, A. V. Shah, R. Platz and J. Andreu, "Improved equivalent circuit and analytical model for amorphous silicon solar cells and modules," *IEEE Transactions on Electron Devices,* vol. 45, pp. 423-429, 1998.

[45] R. Gottschalg, D. G. Infield and M. J. Kearney, "Parametrisation of thin film solar cells," *International Journal of Ambient Energy,* vol. 19, pp. 135-142, 1998.

[46] R. Gottschalg, "Environmental Influences on the Performance of Thin Film Solar Cells," *PhD Thesis, Loughborough University,* 2001.

[47] J. Phang, D. Chan and J. Phillips, "Accurate analytical method for the extraction of solar cell model parameters," *Electronics Letters,* vol. 20, pp. 406-408, 1984.

[48] M. Wolf and H. Rauschenbach, "Series resistance effects on solar cell measurements," *Advanced Energy Conversion,* vol. 3, pp. 455-479, 1963.

[49] A. Kaminski, J. J. Marchand, A. Fave and A. Laugier, "New method of parameters extraction from dark I-V curve," in *26th IEEE Photovoltaic Specialists Conference,* Anaheim, 1997, pp. 203-206.

[50] D. L. King, B. R. Hansen, J. A. Kratochvil and M. A. Quintana, "Dark current-voltage measurements on photovoltaic modules as a diagnostic or manufacturing tool," in *26th IEEE Photovoltaic Specialists Conference,* Anaheim, 1997, pp. 1125-1128.

[51] K. Bouzidi, M. Chegaar and M. Aillerie, "Solar cells parameters evaluation from dark I-V charcteristics," *Energy Procedia,* vol. 18, pp. 1601-1610, 2012.

[52] J. L. Boone and T. P. Van Doren, "Solar-cell design based on a distributed diode analysis," *IEEE Transactions on Electron Devices,* vol. ED-25, pp. 767-771, 1978.

[53] L. D. Nielsen, "Distributed series resistance effects in solar cells," *IEEE Transactions on Electron Devices,* vol. ED-29, pp. 821-827, 1982.

[54] E. Van Kerschaver, J. Nijs, R. Mertens and M. Ghannam, "Twodimensional solar cell simulations by means of circuit modelling," in *26th IEEE Photovoltaic Specialists Conference,* 1997, pp. 175-178.

[55] V. G. Karpov, A. D. Compaan and D. Shvydka, "Effects of nonuniformity in thin-film photovoltaics," *Applied Physics Letters,* vol. 80, pp. 4256-4258, 2002.

[56] U. Rau, P. O. Grabitz and J. H. Werner, "Resistive limitations to spatially inhomogeneous electronic losses in solar cells," *Applied Physics Letters,* vol. 85, pp. 6010-6012, 2004.

[57] A. Helbig, T. Kirchartz, R. Schaeffler, J. H. Werner and U. Rau, "Quantitative electroluminescence analysis of resistive losses in Cu(In, Ga)Se2 thin-film modules," *Solar Energy Materials & Solar Cells,* vol. 94, pp. 979-984, 2010.

[58] K. Araki and M. Yamaguchi, "Novel equivalent circuit model and statistical analysis in parameters identification," *Solar Energy Materials & Solar Cells,* vol. 75, pp. 457-466, 2003.

[59] M. Kasemann, D. Grote, B. Walter, W. Kwapil, T. Trupke, Y. Augarten, R. A. Bardos and E. Pink, "Luminescence imaging for the detection of shunts on silicon solar cells," *Progress in Photovoltaics: Research and Applications,* vol. 16, pp. 297-305, 2008.

[60] M. Frei and D. Wang, "Performance and yield calculations for large-area thin-film modules through distributed modeling," in *34th IEEE Photovoltaic Specialists Conference,* Philadelphia, 2009, pp. 1708-1712.

[61] A. W. Haas, J. R. Wilcox, J. L. Gray and R. J. Schwartz, "A distributed emitter model for solar cells: Extracting an equivalent lumped series resistance," in *34th IEEE Photovoltaic Specialists Conference,* Honolulu, 2010, pp. 002044-002049.

[62] P. Vorasayan, T. R. Betts and R. Gottschalg, "Spatially distributed model for the analysis of laser beam induced current (LBIC) measurements of thin film silicon solar modules," *Solar Energy Materials & Solar Cells,* vol. 95, pp. 111-114, 2011.

[63] Y. Yang, P. P. Altermatt, W. Zhu, X. Liang and H. Shen, "Analysis of industrial c-Si solar cell's front metallization by advanced numerical simulation," *Progress in Photovoltaics: Research and Applications,* vol. 20, pp. 490-500, 2012.

[64] T. Ott, F. R. Runai, F. Schwäble and T. Walter, "2D network simulation and luminescence characterization of Cu(In,Ga)Se2 thin film modules," *Progress in Photovoltaics: Research and Applications,* vol. 20, pp. 600-605, 2012.

[65] S. Guo, F. Ma, B. Hoex, A. G. Aberle and M. Peters, "Analysing solar cells by circuit modelling," *Energy Procedia,* vol. 25, pp. 28-33, 2012.

[66] A. Acciarri, C. Chemelli, F. Fraschini, E. Grilli, A. Martinelli, N. Novello and G. Timò, "Quasi-3D modelling of concentrating photovoltaic solar cell and light emitting diode front contact grid," in *27th European Photovoltaic Solar Energy Conference and Exhibition,* Frankfurt, 2012, pp. 503-508.

[67] G. T. Koishiyev and J. R. Sites, "Impact of sheet resistance on 2-D modeling of thin-film solar cells," *Solar Energy Materials & Solar Cells,* vol. 93, pp. 350-354, 2009.

[68] F. W. Fecher, A. P. Romero, C. J. Brabec and C. Buerhop-Lutz, "Influence of a shunt on the electrical behavior in thin film photovoltaic modules - a 2D finite element simulation study," *Solar Energy,* vol. 105, pp. 494-504, 2014.

[69] P. O. Grabitz, U. Rau and J. H. Werner, "Modeling of spatially inhomogeneous solar cells by a multi-diode approach," *Physica Status Solidi (a),* vol. 202, pp. 2920-2927, 2005.

[70] K. Nishioka, T. Takamoto, W. Nakajima, T. Agui, M. Kaneiwa, Y. Uraoka and T. Fuyuki, "Analysis of triple-junction solar cell under concentration by SPICE," in *3rd World Conference on Photovoltaic Energy Conversion,* 2003, pp. 869-872.

[71] B. Galiana, C. Algora, I. Rey-Stolle and I. G. Vara, "A 3-D model for concentrator solar cells based on distributed circuit units," *IEEE Transactions on Electron Devices,* vol. 52, pp. 2552-2558, 2005.

[72] K. Brecl, M. Topič and F. Smole, "A detailed study of monolithic contacts and electrical losses in a large-area thin-film module," *Prog Photovoltaics Res Appl,* vol. 13, pp. 297-310, 2005.

[73] Matevž Bokalič, J. Raguse, J. R. Sites and Marko Topič, "Analysis of electroluminescence images in small-area circular CdTe solar cells," *J. Appl. Phys.,* vol. 114, pp. 123102, 2013.

[74] Y. Vygranenko, M. Fernandes, M. Vieira, A. Khosropour and A. Sazonov, "A Distributed SPICE Model for Amorphous Silicon Solar Cells," *Energy Procedia,* vol. 60, pp. 96-101, 2014.

[75] T. Fuyuki, A. Tani, S. Tsujii and E. Sugimura, "Photographic distinction of defects in polycrystalline si by spectroscopic electroluminescence," in *35th IEEE Photovoltaic Specialists Conference,* Honolulu, 2010, pp. 001380-001382.

[76] L. Singher, I. Naot and L. Levin, "Multi-wavelength photoluminescence for CIGS characterisation," in *26th European Photovoltaic Solar Energy Conference and Exhibition,* Hamburg, 2011, pp. 3007-3009.

[77] M. Bliss, X. Wu, K. Bedrich, T. R. Betts and R. Gottschalg, "Spatially and spectrally resolved spectral electroluminescence measurement system," in *10th Photovoltaic Science Application and Technology*
, Loughborough, 2014, pp. 201-204.

[78] E. L. Miller, S. S. Chern and A. Shunka, "The solar cell laser scanner," in *15th IEEE Photovoltaic Specialists Conference,* Kissimmee, 1981, pp. 1126-1131.

[79] C. R. Osterwald and K. A. Emery, "Solar cell area considerations," *Solar Cells,* vol. 10, pp. 1-5, 1983.

[80] S. Damaskinos, "An improved laser scanning technique for evaluation of solar cells: application to CuInSe2/(CdZn)S devices," *Solar Cells,* vol. 26, pp. 151-158, 1989.

[81] T. Kulessa, T. Eickhoff, W. Hilgers and J. Herion, "Detection of local shunts, pinholes and thickness inhomogeneities in a-si solar cells by light beam induced current (LBIC)," in *11th European Photovoltaic Solar Energy Conference,* Montreux, 1992, pp. 575-577.

[82] S. Martinuzzi and M. Stemmer, "Mapping of defects and their recombination strength by a light-beam-induced current in silicon wafers," in *3rd International Workshop of NATO Advanced Research Workshop,* Bologna, 1993, pp. 152-158.

[83] R. Matson and K. Emery, "The large scale laser scanner: Milli-characterization of photovoltaic devices and modules," in *12th European Photovoltaic Solar Energy Conference,* Amsterdam, 1994, pp. 1222-1225.

[84] R. Bisconti, R. A. Kous, M. Lundqvist and H. A. Ossenbrink, "ESTI scan facility," *Solar Energy Materials & Solar Cells,* vol. 48, pp. 61-68, 1997.

[85] W. Warta, J. Sutter, B. F. Wagner and R. Schindler, "Impact of diffusion length distributions on the performance of mc-silicon solar cells," in *2nd World Conference on Photovoltaic Energy Conversion Conference,* Vienna, 1998, pp. 1650-1653.

[86] J. Carstensen, G. Popkirov, J. Bahr and H. Foll, "CELLO: An advanced LBIC measurement for solar cell local characterization," in *16th European Photovoltaic Solar Energy Conference,* Glasgow, 2000, pp. 1627-1630.

[87] A. Kress, T. Pernau, P. Fath and E. Bucher, "LBIC measurements on low cost back contact solar cells," in *16th European Photovoltaic Solar Energy Conference,* Glasgow, 2000, .

[88] S. Roschier, G. Agostinelli and E. D. Dunlop, "Laser scanning of amorphous silicon photovoltaic modules with different bias conditions," *Opto-Electronics Review,* vol. 8, pp. 328-332, 2000.

[89] M. Acciarri, S. Binetti, A. Racz, S. Pizzini and G. Agostinelli, "Fast LBIC inline characterization for process quality control in the photovoltaic industry," *Solar Energy Materials & Solar Cells,* vol. 72, pp. 417-424, 2002.

[90] T. Pernau, P. Fath and E. Bucher, "Phase-sensitive LBIC analysis," in *29th IEEE Photovoltaic Specialists Conference,* New Orleans, 2002, pp. 442-445.

[91] G. Agostinelli and E. D. Dunlop, "Local inversion of photocurrent in cadmium telluride solar cells," *Thin Solid Films,* vol. 431-432, pp. 448-452, 2003.

[92] T. Michel, R. Gottschalg and D. G. Infield, "Large area laser scanning of amorphous silicon modules," in *19th European Photovoltaic Solar Energy Conference,* Paris, 2004, pp. 2522-2524.

[93] M. Bouaïcha, W. Dimassi, H. Nouri, B. Bessaïs and R. Bennaceur, "Evaluation of the diffusion length of gettered multicrystalline silicon using solar cells – cross-sectional LBIC scan," *Physica Status Solidi (a),* vol. 202, pp. 1808-1813, 2005.

[94] S. Mathissen, J. Carstensen, H. Foll, G. Voorwinden and H. Stiebig, "CELLO measurements of CIGS and ucSi solar cells," in *Material Research Society Symposium,* 2005, pp. 215-220.

[95] C. Fernandez-Lorenzo, J. A. Poce-Fatou, R. Alcantara, J. Navas and J. Martin, "High resolution laser beam induced current focusing for photoactive surface characterization," *Applied Surface Science,* vol. 253, pp. 2179-2188, 2006.

[96] P. Vorasayan, M. Bliss, T. Betts, R. Gottschalg and A. N. Tiwari, "Large area LBIC measurement system for thin film photovoltaic modules," in *Solar Energy Society (UK-ISES) 2006,* 2006, .

[97] F. J. Vorster and E. E. Van Dyk, "High saturation solar light beam induced current scanning of solar cells," *Review of Scientific Instruments,* vol. 78, pp. 013940, 2007.

[98] M. Ben Rabha, W. Dimassi, M. Bouaicha, H. Ezzaouia and B. Bessais, "Laser-beam-induced current mapping evaluation of porous silicon-based passivation in polycrystalline silicon solar cells," *Solar Energy,* vol. 83, pp. 721-725, 2009.

[99] F. J. Navas, R. Alcántara, C. Fernández-Lorenzo and J. Martín, "A methodology for improving laser beam induced current images of dye sensitized solar cells," *Review of Scientific Instruments,* vol. 80, pp. 063102, 2009.

[100] P. Vorasayan, T. R. Betts, A. N. Tiwari and R. Gottschalg, "Multi-laser LBIC system for thin film PV module characterisation," *Solar Energy Materials & Solar Cells,* vol. 93, pp. 917-921, 2009.

[101] J. Navas, R. Alcantara, C. Fernandez-Lorenzo, J. Anta, E. Guillen and J. Martin-Calleja, "Improving photoresponse characterization of dye-sensitized solar cells: application to the laser beam-induced current technique," *Measurement Science and Technology,* vol. 21, pp. 075702, 2010.

[102] B. Moralejo, V. Hortelano, M. A. González, O. Martínez, J. Jiménez, S. Ponce-Alcántara and V. Parra, "Study of the crystal features of mc-Si PV cells by laser beam induced current (LBIC)," *Physica Status Solidi (c),* vol. 8, pp. 1330-1333, 2011.

[103] W. Brooks, S. Irvine, V. Barrioz and A. J. Clayton, "Laser beam induced current measurements of Cd1-xZnxS/CdTe solar cells," *Solar Energy Materials & Solar Cells,* vol. 101, pp. 26-31, 2012.

[104] J. -. Wagner, J. Carstensen, A. Schütt and H. Föll, "Qualitative and quantitative evaluation of thin-film solar cells using solar cell local characterization," *Journal of Applied Physics,* vol. 113, pp. 064503, 2013.

[105] *Light Beam Induced Current - Semilab*. Available: http://www.semilab.hu/technologies/pvi/light-beam-induced-current.

[106] *Corescan - Sunlab*. Available: http://www.sunlab.nl/index.php/9-corescan/14-application-examples-corescan.

[107] J. M. Frey, S. S. Hegedus and C. P. Thompson, "Quantitative analysis and extraction of cell parameters from interconnected thin-film solar modules through LBIC-voltage sweeps," in *35th IEEE Photovoltaic Specialists Conference,* Honolulu, 2010, pp. 001277-001282.

[108] C. Shen, H. Kampwerth, M. Green, T. Trupke, J. Carstensen and A. Schutt, "Spatially resolved photoluminescence imaging of essential silicon solar cell parameters and comparison with CELLO measurements," *Solar Energy Materials & Solar Cells,* vol. 109, pp. 77-81, 2013.

[109] Y. Augarten, T. Trupke, M. Lenio, J. Bauer, J. W. Weber, M. Juhl, M. Kasemann and O. Breitenstein, "Calculation of quantitative shunt values using photoluminescence imaging," *Progress in Photovoltaics: Research and Applications,* vol. 21, pp. 933-941, 2013.

[110] C. Karcher, H. Helmers, M. Schachtner, F. Dimorth and A. W. Bett, "Temperature-dependent electroluminescence and voltages of multi-junction solar cells," *Progress in Photovoltaics: Research and Applications,* vol. 28th EU PVSEC, 2013.

[111] S. Rißland and O. Breitenstein, "Evaluation of luminescence images of solar cells for injection-level dependent lifetimes," *Solar Energy Materials & Solar Cells,* vol. 111, pp. 112-114, 2013.

[112] S. Besold, U. Hoyer, J. Bachmann, T. Swonke, P. Schilinsky, R. Steim and C. J. Brabec, "Quantitative imaging of shunts in organic photovoltaic modules using lock-in thermography," *Solar Energy Materials & Solar Cells,* vol. 124, pp. 133-137, 2014.

[113] M. Topic, J. Raguse, K. Zaunbrecher, M. Bokalic and J. R. Sites, "Electroluminescence of Thin Film Solar Cells and PV Modules - Camera Calibration," 2011.

[114] O. Breitenstein, W. Eberhardt and K. Iwig, "Imaging the local forward current density of solar cells by dynamical precision contact thermography," in *IEEE First World Conference on Photovoltaic Energy Conversion (Vol. 2), 1994.* Waikoloa, 1994, pp. 1633-1636.

[115] O. Breitenstein and M. Langenkamp, *Lock-in Thermography - Basics and use for Functional Diagnostics of Electronic Components.* Berlin: Springer, 2003.

[116] Z. Hameiri and P. Chaturvedi, "Spatially resolved electrical parameters of silicon wafers and solar cells by contactless photoluminescence imaging," *Applied Physics Letters,* vol. 102, pp. 073502-1-073502-3, 2013.

[117] B. True, A. Stavrides and I. Latchford, "Image processing techniques for correlation of photoluminescence images of as-cut wafers with final cell IV parameters," in *26th European Photovoltaic Solar Energy Conference and Exhibition,* Hamburg, 2011, pp. 2095-2098.

[118] T. Trupke, R. A. Bardos, M. D. Abbott, P. Wurfel, E. Pink, Y. Augarten, F. W. Chen, K. Fisher, J. E. Cotter, M. Kasemann, M. C. Schubert, M. The, S. W. Glunz, W. Warta, D. Macdonald, J. Tan, A. Cuevas, J. Bauer, R. Gupta, O. Breitenstein, T. Buonassisi, G. Tarnowski, A. Lorenz, H. P. Hartmann, D. H. Neuhaus and J. M. Fernandez, "Progress with luminescence imaging for the characterisation of silicon wafers and solar cells," in *22nd European Photovoltaic Solar Energy Conference,* Milan, 2007, pp. 22-31.

[119] T. Trupke, R. A. Bardos, M. D. Abbott, K. Fisher, J. Bauer and O. Breitenstein, "Liminescence imaging for fast shunt localization in silicon solar cells and silicon wafers," in *International Workshop on Science and Technology of Crystalline Silicon Solar Cells,* Sendai, 2006, .

[120] T. Trupke, R. A. Bardos, M. D. Abbott and J. E. Cotter, "Suns-photoluminescence: contactless determination of current-voltage characteristics of silicon wafers," *Applied Physics Letters,* vol. 87, pp. 093503, 2005.

[121] T. Fuyuki, H. Kondo, Y. Kaji, A. Ogane and Y. Takahashi, "Analytic findings in the electroluminescence characterization of crystalline silicon solar cells," *Journal of Applied Physics,* vol. 101, pp. 023711, 2007.

[122] P. Würfel, T. Trupke, T. Puzzer, E. Schäffer, W. Warta and S. W. Glunz, "Diffusion lengths of silicon solar cells from luminescence images," *Journal of Applied Physics,* vol. 101, pp. 123110, 2007.

[123] O. Breitenstein, J. Bauer, T. Trupke and R. A. Bardos, "On the detection of shunts in silicon solar cells by photo- and electroliminescence imaging," *Progress in Photovoltaics: Research and Applications,* vol. 16, pp. 325-330, 2008.

[124] O. Breitenstein, A. Khanna, Y. Augarten, J. Bauer, J. -. Wagner and K. Iwig, "Quantitative evaluation of electroluminescence images of solar cells," *Phys. Status Solidi RRL,* vol. 4, pp. 7-9, 2010.

[125] M. Köntges, M. Siebert, D. Hinken, U. Eitner, K. Bothe and T. Potthof, "Quantitative analysis of PV-modules by electroluminescence images for quality control," in *24th European Photovoltaic Solar Energy Conference,* Hamburg, 2009, pp. 4CO.2.3.

[126] M. Kasemann, M. C. Schubert, M. The, M. Köber, M. Hermle and W. Warta, "Comparison of luminescence imaging and illuminated lock-in thermography on silicon solar cells," *Applied Physics Letters,* vol. 89, pp. 224102-1-224102-3, 2006.

[127] O. Breitenstein, J. Bauer, K. Bothe, D. Hinken, J. Muller, W. Kwapil, M. C. Schubert and W. Warta, "Can Luminescence Imaging Replace Lock-in Thermography on Solar Cells?" *IEEE Journal of Photovoltaics,* vol. 1, pp. 159-167, 2011.

[128] D. Hinken, K. Ramspeck, K. Bothe, B. Fischer and R. Brendel, "Series resistance imaging of solar cells by voltage dependent electroluminescence," *Applied Physics Letters,* vol. 97, pp. 182104-1-182104-3, 2007.

[129] T. Trupke, E. Pink, R. A. Bardos and M. D. Abbott, "Spatially resolved series resistance of silicon solar cells obtained from luminescence imaging," *Applied Physics Letters,* vol. 90, pp. 093506-1-093506-3, 2007.

[130] K. Bothe, P. Pohl, J. Schmidt, T. Weber, P. Altermatt, B. Fischer and R. Brendel, "Electroluminescence imaging as an in-line characterisation tool for solar cell production," in *21st European Photovoltaic Solar Energy Conference,* Dresden, 2006, pp. 597-600.

[131] M. D. Abbott, T. Trupke, H. P. Hartmann, R. Gupta and O. Breitenstein, "Laser isolation of shunted regions in industrial solar cells," *Progress in Photovoltaics: Research and Applications,* vol. 15, pp. 613-620, 2007.

[132] K. Bothe, K. Ramspeck, D. Hinken, C. Schinke, J. Schmidt, S. Herlufsen, R. Brendel, J. Bauer, J. -. Wagner, N. Zakharov and O. Breitenstein, "Luminescence emission from forward- and reverse-biased multicrystalline silicon solar cells," *Journal of Applied Physics,* vol. 106, pp. 104510, 2009.

[133] A. Kitiyanan, A. Ogane, A. Tani, T. Hatayama, H. Yano, Y. Uraoka and T. Fuyuki, "Comprehensive study of electroluminescence in multicrystalline silicon solar cells," *Journal of Applied Physics,* vol. 106, pp. 043717, 2009.

[134] J. Bachmann, C. Buerhop-Lutz, R. Steim, P. Schilinsky, J. A. Hauch, E. Zeira and B. J. Christoh, "Highly sensitive non-contact shunt detection of organic photovoltaic modules," *Solar Energy Materials & Solar Cells,* vol. 101, pp. 176-179, 2012.

[135] G. M. Berman, N. Call, R. K. Ahrenkiel and S. W. Johnston, "Evaluation of four imaging techniques for the electrical characterization of solar cells," in *2008 Materials Reserch Society Fall Meeting,* Boston, 2008, .

[136] P. Somasundaran, A. Sinha and R. Gupta, "Simulation and characterization of spatial variation of shunts in industrial solar cells by pspice and dark lock-in infrared thermography," in *27th European Photovoltaic Solar Energy Conference and Exhibition,* Frankfurt, 2012, pp. 744-748.

[137] O. Breitenstein, J. P. Rakotoniaina, M. kaes, S. Seren, T. Pernau, G. Hahn, W. Warta and J. Isenberg, "Lock-in thermography - a universal tool for local analysi of solar cells," in *20th European Photovoltaic Solar Energy Conference,* Barcelona, 2005, pp. 590-593.

[138] U. Rau, "Superposition and reciprocity in the electroluminescence and photoluminescence of solar cells," *IEEE Journal of Photovoltaics,* vol. 2, pp. 169-172, 2012.

[139] U. Rau, "Reciprocity relation between photovoltaic quantum efficiency and electroluminescent emission of solar cells," *Physical Review B,* vol. 76, pp. 085303, 2007.

[140] T. Kirchartz, A. Helbig, W. Reetz, M. Reuter, J. H. Werner and U. Rau, "Reciprocity between electroluminescence and quantum efficiency used for the characterization of silicon solar cells," *Progress in Photovoltaics: Research and Applications,* vol. 17, pp. 394-402, 2009.

[141] V. Gazuz and C. Buerhop, "Detection of power losses in busbar solder contacts by electroluminescence imaging of solar cells," *Meas. Sci. Technol.,* vol. 22, pp. 115702-1-115702-6, 2011.

[142] M. Glatthaar, J. Giesecke, M. Kasemann, J. Haunschild, M. The, W. Warta and S. Rein, "Spatially resolved determination of the dark saturation current of silicon solar cells from electroluminescence images," *Journal of Applied Physics,* vol. 105, pp. 113110-1-113110-5, 2009.

[143] M. Seeland, R. Rösch and H. Hoppe, "Quantitative analysis of electroluminescence images from polymer solar cells," *Journal of Applied Physics,* vol. 111, pp. 024505-1-024505-5, 2012.

[144] F. Fertig, J. Greulich and S. Rein, "Spatially resolved determination of the short-circuit current density of silicon solar cells via lock-in thermography," *Applied Physics Letters,* vol. 104, pp. 201111-1-201111-4, 2014.

[145] B. Hallam, Y. Augarten, B. Tjahjono, T. Trupke and S. Wenham, "Photoluminescence imaging for determining the spatially resolved implied open circuit voltage of silicon solar cells," *Journal of Applied Physics,* vol. 115, pp. 044901-1-044901-9, 2014.

[146] O. Breitenstein, "Nondestructive local analysis of current-voltage characteristics of solar cells by lock-in thermography," *Solar Energy Materials & Solar Cells,* vol. 95, pp. 2933-2936, 2011.

[147] J. Wong, "Griddler: Intelligent computer aided design of complex solar cell metallization patterns," in *2013 IEEE 39th Photovoltaic Specialists Conference (PVSC),* Tampa, USA, 2013, pp. 0933-0938.

[148] B. E. Pieters, "A free and open source finite-difference simulation tool for solar modules," in *2014 IEEE 40th Photovoltaic Specialist Conference (PVSC),* Denver, USA, 2014, pp. 1370-1375.

[149] E. P. Natarajan, "KLU - A high performance sparse linear solver for circuit simulation problems," *MSc Thesis, University of Florida,* 2005.

[150] T. A. Davis and E. P. Natarajan, " Algorithm 907: KLU, a direct sparse solver for circuit simulation problems," *ACM Transactions on Mathematical Software,* vol. 37, pp. 36:1-36:17, 2010.

[151] X. Li and J. W. Demmel, "SuperLU DIST: A scalable distributed memory sparse direct solver for unsymmetric linear systems," *ACM Transactions on Mathematical Software,* vol. 29, pp. 110-140, 2003.

[152] X. Chen, Y. Wang and H. Yang, "NICSLU: An adaptive sparse matrix solver for parallel circuit simulation," *IEEE Transactions on Computer-Aided Design of Integrated Circuits and Systems,* vol. 32, pp. 261-274, 2013.

[153] *Spice OPUS*. Available: http://www.spiceopus.si/.

[154] L. W. Nagel, "SPICE2: A computer program to simulate semiconductor circuits," *PhD Thesis, University of California, Berkeley,* 1975.

[155] R. M. Kielkowski, *Inside SPICE.* McGraw-Hill, 1998.

[156] D. S. Watkins, *Fundamentals of Matrix Computations.* New Jersey: Wiley, 2010.

[157] R. A. Horn and C. A. Johnson, *Matrix Analysis.* Cambridge University Press, 1985.

[158] T. A. Davis and E. P. Natarajan, "Sparse matrix methods for circuit simulation problems," *Scientific Computing in Electrical Engineering SCEE 2010, Mathematics in Industry,* pp. 3-14, 2012.

[159] J. H. Mathews and K. D. Fink, *Numerical Methods using MATLAB.* Prentice-Hall, 2003.

[160] W. H. Press, *Numerical Recipes in C++ : The Art of Scientific Computing.* Cambridge University Press, 1992.

[161] J. W. Demmel, *Applied Numerical Linear Algebra.* Society for Industrial and Applied Mathematics (SIAM), 1997.

[162] J. W. Demmel, S. C. Eisenstat, J. R. Gilbert, X. Li and J. W. H. Liu, " A supernodal approach to sparse partial pivoting," *SIAM Journal on Matrix Analysis and Applications,* vol. 20, pp. 720-755, 1999.

[163] J. W. Demmel, J. R. Gilbert and X. Li, "An asynchronous parallel supernodal algorithm for sparse Gaussian elimination," *SIAM Journal on Matrix Analysis and Applications,* vol. 20, pp. 915-952, 1999.

[164] T. A. Davis, "Direct methods for sparse linear systems," Society for Industrial and Applied Mathematics, Philadelphia, 2006.

[165] Y. Saad, "Iterative methods for sparse linear systems (2nd edition)," Society for Industrial and Applied Mathematics, Philadelphia, 2003.

[166] Y. Saad and M. H. Schultz, "GMRES: A generalized minimal residual algorithm for solving nonsymmetric linear systems," *SIAM Journal on Scientific & Statistical Computing,* vol. 7, pp. 856-869, 1986.

[167] J. R. Shewchuk, "An introduction to the conjugate gradient method without the agonizing pain (edition 1.25)," School of Computer Science, Carnegie Mellon University, 1994.

[168] D. Michels, "Sparse-matrix-CG-solver in CUDA," in *15th Central European Seminar on Computer Graphics,* Viničné, 2011, pp. 123-130.

[169] *Nvidia CUDA Parallel Programming and Computing Platform*. Available: http://www.nvidia.com/object/cuda_home_new.html.

[170] Anonymous "CUDA C programming guide (version 5.5)," Nvida, Tech. Rep. PG-02829-001, 2013.

[171] *cuSPARSE Library*. Available: https://developer.nvidia.com/cusparse.

[172] *cuBLAS Library*. Available: https://developer.nvidia.com/cublas.

[173] *cusp Library*. Available: http://code.google.com/p/cusp-library/.

[174] *Root-mean-square deviation*. Available: http://en.wikipedia.org/wiki/Root-mean-square_deviation.

[175] X. Wu, M. Bliss, T. R. Betts and R. Gottschalg, "Fast spatially-resolved electrical modelling for photovoltaic cells using accelerated PV-oriented nodal analysis," in *10th Photovoltaic Science Application and Technology,* Loughborough, UK, 2014, pp. 225-228.

[176] P. Mack, T. Ott, F. Schwäble, F. Runai and T. Walter, "2D- Network Simulation and Modelling of CIGS Modules," 2010.

[177] J. W. Bishop, "Computer simulation of the effects of electrical mismatches in photovoltaic cell interconnection circuits," *Solar Cells,* vol. 25, pp. 73-89, 1988.

[178] I. Cole, "Modelling CPV," *PhD Thesis, Loughborough University,* 2015.

[179] J. A. Gow and C. D. Manning, "Development of a photovoltaic array model for use in power-electronics simulation studies," in *IEE Proceedings - Electric Power Applications, Vol. 146, no. 2*, 1999, pp. 193-200.

[180] J. O. Bird, *Electrical Circuit Theory and Technology.* Oxford: Newnes/Elsevier Science, 2007.

[181] A. Woyte, J. Nijs and R. Belmans, "Partial shadowing of photovoltaic arrays with different system configurations: literature review and field test results," *Solar Energy,* vol. 74, pp. 217-233, 2003.

[182] E. Karatepe, M. Boztepe and M. Colak, "Development of a suitable model for characterizing photovoltaic arrays with shaded solar cells," *Solar Energy,* vol. 81, pp. 977-992, 2007.

[183] M. C. Alonso-Garcia and J. M. Ruiz, "Analysis and modelling the reverse characteristic of photovoltaic cells," *Solar Energy Materials & Solar Cells,* vol. 90, pp. 1105-1120, 2006.

[184] M. C. Alonso-Garcia, J. M. Ruiz and F. Chenloa, "Experimental study of mismatch and shading effects in the I–V characteristic of a photovoltaic module," *Solar Energy Materials & Solar Cells,* vol. 90, pp. 329-340, 2006.

[185] M. C. Alonso-Garcia, J. M. Ruiz and W. Herrmann, "Computer simulation of shading effects in photovoltaic arrays," *Renewable Energy,* vol. 31, pp. 1986-1993, 2006.

[186] M. Chegaar, G. Azzouzi and P. Mialhe, "Simple parameter extraction method for illuminated solar cells," *Solid-State Electronics,* vol. 50, pp. 1234-1237, 2006.

[187] Y. Chen, X. Wang, D. Li, R. Hong and H. Shen, "Parameters extraction from commercial solar cells I–V characteristics and shunt analysis," *Applied Energy,* vol. 88, pp. 2239-2244, 2011.

[188] A. Jain and A. Kapoor, "Exact analytical solutions of the parameters of real solar cells using Lambert W-function," *Solar Energy Materials & Solar Cells,* vol. 81, pp. 269-277, 2004.

[189] A. Jain and A. Kapoor, "A new method to determine the diode ideality factor of real solar cell using Lambert W-function," *Solar Energy Materials & Solar Cells,* vol. 85, pp. 391-396, 2005.

[190] A. Jain, S. Sharma and A. Kapoor, "Solar cell array parameters using Lambert W-function," *Solar Energy Materials & Solar Cells,* vol. 90, pp. 25-31, 2006.

[191] W. Kim and W. Choi, "A novel parameter extraction method for the one-diode solar cell model," *Solar Energy,* vol. 84, pp. 1008-1019, 2010.

[192] Y. Li, W. Huang, H. Huang, C. Hweitt, Y. Chen, G. Fang and D. L. Carroll, "Evaluation of methods to extract parameters from current-voltage characteristics of solar cells," *Solar Energy,* vol. 90, pp. 51-57, 2013.

[193] C. Zhang, J. Zhang, Y. Hao, Z. Lin and C. Zhu, "A simple and efficient solar cell parameter extraction method from a single current-voltage curve," *Journal of Applied Physics,* vol. 110, pp. 064504, 2011.

[194] M. W. Denhoff and N. Drolet, "The effect of the front contact sheet resistance on solar cell performance," *Solar Energy Materials & Solar Cells,* vol. 93, pp. 1499-1506, 2009.

[195] C. Monokroussos, R. Rüther, R. Gottschalg, M. Kong and D. G. Infield, "Effect of cell width on the device performance of amorphous silicon solar cells," in *19th European Photovoltaic Solar Energy Conference,* Paris, 2004, pp. 1489-1492.

[196] U. Malm and M. Edoff, "Influence from front contact sheet resistance on extracted diode parameters in CIGS solar cells," *Progress in Photovoltaics: Research and Applications,* vol. 16, pp. 113-121, 2008.

[197] M. Bliss, X. Wu, K. Bedrich, T. R. Betts and R. Gottschalg, "Spatially and spectrally resolved spectral electroluminescence measurement system," *IET Renewable Power Generation,* vol. (Accepted for publication), 2015.

[198] S. Rißland and O. Breitenstein, "High resolution saturation current density imaging at grain boundaries by lock-in thermography," *Solar Energy Materials & Solar Cells,* vol. 104, pp. 121-124, 2012.

[199] D. Abou-Ras, T. Kirchartz and U. Rau, *Advanced Characterization Techniques for Thin Film Solar Cells.* Weinheim, Germany: Wiley-VCH, 2011.

[200] M. Kasemann, W. Kwapil, B. Walter, J. Giesecke, T. Michel, M. The, J. -. Wagner, J. Bauer, A. Schutt, J. Carstensen, S. Kluska, F. Granek, H. Kampwerth, P. Gundel, M. C. Schubert, R. A. Bardos, H. Foll, H. Nagel, P. Wurfel, T. Trupke, O. Breitenstein, M. Hermle, W. Warta and S. W. Glunz, "Progress in silicon solar cell characterization with infrared imaging methods," in *23ed European Photovoltaic Solar Energy Conference,* Valencia, 2008, pp. 965-973.

[201] B. Matevž and M. Topič, *Spatially Resolved Characterization in Thin-Film Photovoltaics.* Springer International Publishing, 2015.

[202] R. Gottschalg, M. Rommel, D. G. Infield and M. Kearney, "The influence of the measurement environment on the accuracy of the extraction of the physical parameters of solar cells," *Meas Sci Technol,* vol. 10, pp. 796-804, 1999.

[203] J. Bird, *Engineering Mathematics.* Routledge, 2010.

List of publications

Journal articles

X. Wu, M. Bliss, A. Sinha, T.R. Betts, R. Gupta and R. Gottschalg, "Accelerated spatially-resolved electrical simulation for photovoltaic devices using photovoltaic-oriented nodal analysis", *IEEE Transactions on Electron Devices*, available online (DOI: 10.1109/TED.2015.2409058).

M. Bliss, **X. Wu**, K. Bedrich, T.R. Betts and R. Gottschalg, "Spatially and spectrally resolved spectral electroluminescence measurement system", *IET Renewable Power Generation*, accepted.

X. Wu, M. Bliss, A. Sinha, T.R. Betts, R. Gupta and R. Gottschalg, "Distributed network modelling approach for spatially-resolved characterisation of photovoltaic modules", *IET Renewable Power Generation*, vol. 8, no. 5, pp. 459-466, 2014.

Conference papers

G. Koutsourakis, M. Cashmore, **X. Wu**, S. Hall, M. Bliss, T.R. Betts and R. Gottschalg, "Fast current mapping of photovoltaic devices using compressive sampling", abstract submitted to *European PV Solar Energy Conference and Exhibition (EU-PVSEC)* 2015.

X. Wu, M. Bliss, T.R. Betts and R. Gottschalg, "Effects of lateral resistances in photovoltaic cells and full 2-D parameter extraction for the spatially-resolved models using electroluminescence images", *11th Photovoltaic Science Application and Technology (PVSAT-11)*, accepted for an oral presentation.

X. Wu, M. Bliss, J. Zhu, T.R. Betts and R. Gottschalg, "Fast electrical modelling for spatially-resolved characterization of amorphous silicon photovoltaic cells", *40th IEEE Photovoltaic Specialists Conference (PVSC-40)*, Denver, USA, pp. 2620-2625, June 2014.

X. Wu, M. Bliss, T.R. Betts, and R. Gottschalg "Fast spatially-resolved electrical modelling for photovoltaic cells using accelerated PV-oriented nodal analysis", in *10th Photovoltaic Science Application and Technology (PVSAT-10)*, Loughborough, UK, pp. 225-228, April 2014.

M. Bliss, **X. Wu**, K. Bedrich, T.R. Betts and R. Gottschalg, "Spatially and spectrally resolved spectral electroluminescence measurement system", in *10th Photovoltaic Science Application and Technology (PVSAT-10)*, Loughborough, UK, pp. 201-204, April 2014.

X. Wu, M. Bliss, A. Sinha, T.R. Betts, R. Gupta and R. Gottschalg, "Modelling spatial electrical properties in photovoltaic modules using PV-oriented nodal analysis", in *39th Annual Conference of the IEEE Industrial Electronics Society (IECON 2013)*, Vienna, Austria, pp. 8098-8103, November 2013.

X. Wu, A. Sinha, M. Bliss, T.R. Betts, R. Gupta and R. Gottschalg, "A distributed network modelling Approach for spatially-resolved characterisation of photovoltaic modules", in *9th Photovoltaic Science Application and Technology (PVSAT-9)*, Swansea, UK, pp. 49-52, April 2013.